# Advanced synchrotron texture analysis of phyllosilicate-rich rocks from different tectonic settings – Understanding texture-forming processes and anisotropic physical properties

Dissertation
zur Erlangung des mathematisch-naturwissenschaftlichen Doktorgrades
"Doctor rerum naturalium"
der Georg-August-Universität Göttingen

im Promotionsprogramm Geowissenschaften / Geographie
der Georg-August University School of Science (GAUSS)

vorgelegt von
Rebecca Kühn

aus Siegen

Göttingen 2019

Betreuungsausschuss:
Prof. Dr. Jonas Kley, Strukturgeologie und Geodynamik, GZG
Prof. Dr. Michael Stipp, Geodynamik, Martin-Luther-Universität Halle
Dr. Bernd Leiss, Strukturgeologie und Geodynamik, GZG

Mitglieder der Prüfungskommission

| | |
|---|---|
| Referent/in: | Prof. Dr. Jonas Kley, Strukturgeologie und Geodynamik, GZG |
| Korreferent/in: | Prof. Dr. Michael Stipp, Geodynamik, Martin-Luther-Universität Halle |

weitere Mitglieder der Prüfungskommission:
Prof. Dr. Jan Behrmann, Marine Geodynamik, GEOMAR/Christian-Albrechts-Universität Kiel
Dr. Bernd Leiss, Strukturgeologie und Geodynamik, GZG
Dr. Klaus Wemmer, Isotopengeologie, GZG
Dr. Kirsten Techmer, Kristallographie, GZG

Tag der mündlichen Prüfung:
07.03.2019

## Acknowledgements

My deepest appreciation goes to my mentor Dr. Bernd Leiss for the continuous support of my PhD study, for motivating and encouraging me.

Secondly, I am really grateful to Prof. Dr. Michael Stipp, for his patience and support, and encouraging me to finalize my thesis.

I would like to express my sincere gratitude to Prof. Jonas Kley for the opportunity of conducting my research and his continuous support of my Ph.D. work and thesis.

Furthermore, I am thankful to Prof. Dr. Jan Behrmann for the opportunity to work in his projects, his support and immense knowledge.

I would also like to thank Dr. Klaus Wemmer for being part of my thesis committee, his support during clay mineral analysis and his sympathetic attitude. I am further thankful to Dr. Kirsten Techmer for being part of my thesis committee and her support during SEM studies.

I am grateful to Prof. Dr. Ann Hirt and Prof. Dr. Andrea Biedermann for supporting me in AMS issues. I would further like to thank Dr. Volker Karius for his support with X-ray powder analysis. Dr. Jens Walter and Dr. David Hindle are thanked for supporting me with computer power for data analysis, and Graciela Sosa for the possibility of using the microscope.

This thesis would not have been possible unless the support and patience of friends and colleagues. In Göttingen I wish to give special thanks to Florian Duschl, Johanna Menningen, Hans Heinrich Müller and everyone who helped me in any kind of way. And in Kiel I would like to warmheartedly thank Michel Kühn, Robert Kurzawski, Judith Elger and everyone else from the “Mittagsrunde”.

I am thankful to Barbara and Peter for their kind support, especially during these last weeks.

Special thanks to my parents, Beate and Ebi, for their always loving support, and Pete, thank you for everything.

## Abstract

Texture analysis, i.e. the analysis of the crystallographic preferred orientations of minerals in rocks, contributes to the understanding of the deformation history and physical properties of rocks. Methods generally applied in geosciences, like optical methods, X-ray, neutron, or electron backscatter diffraction are often not suitable for multiphase, polycrystalline rocks rich in phyllosilicates as preparation or measurement procedures are inapplicable. Applying synchrotron radiation for quantitative texture analysis, i.e. high energy X-rays, with its high penetration depth, allows to measure a sample volume, is unaffected by water and overcomes preparation effects on the sample surface. A relative small beam size of 0.5-1 mm in diameter, however, makes it usually inapplicable to materials with larger grain sizes. An advanced workflow from sample preparation, to measuring and data processing was developed to make the method applicable to such specific rocks. Whole “slices” of cylindrical samples are measured and - if necessary - several slices per sample are finally added to represent a bulk rock texture. The applicability of the work flow using synchrotron diffraction was tested by three case studies regarding phyllosilicate-rich rocks. 1) Quantitative texture analysis of Devonian black shales from the Appalachian Plateau in Pennsylvania (USA) was applied to calculate the anisotropy of the magnetic susceptibility. The modeling results are compared to experimental AMS measurements, which show a good agreement and quantitatively prove that the magnetic anisotropy in these samples is carried by the phyllosilicates. Texture and magnetic fabric dominantly reflect compaction, but also far field tectonic imprint from the Alleghenian orogeny. 2) Water-rich muds and mud rocks from the subduction zone offshore Costa Rica were analyzed regarding their composition and texture. The results give insight into the texture development processes as the compaction of these “freshly” sedimented clay-rich rocks and the tectonic overprint at the continental slope. 3) Fresh oceanic serpentinites consisting from chrysotile and lizardite from the Atlantis Massif oceanic core complex show textures which are interpreted by microstructural analyses to be originating from two different processes. In one case, texture was created by the pseudomorphic serpentinization of pyroxenes leading to the formation of bastites, which generates a local texture. In the other case, texture developed due to a preferred orientation of the serpentinizing microfractures which are supposed to be linked to deformation, either prior to serpentinization or due to the volume increase during metamorphosis. Serpentine minerals adopt a growth direction linked to the orientation of the fractures and thereby generate a textured microfabric. Both processes can lead to seismic anisotropy in these rocks. In all three case studies synchrotron texture analysis in combination with Rietveld refinement lead to the successful determination of textures of the extremely complicated rock material and allowed new insights in processes of texture formation and the contribution to the physical anisotropies. This thesis extends the common comprehension and

applicability of texture analysis usually applied to intra-crystalline plastically deformed rocks to delicate samples affected by sedimentary or metamorphic processes.

# Table of content

# 1. Introduction

## 1.1. Rationale

From a rheological point of view, phyllosilicates play an important role in the localization of tectonic processes. Most phyllosilicates exhibit pronounced plate-like shape anisotropy and deform easily by basal glide on these planes (e.g. Shea and Kronenberg, 1992), which characterizes them as rheologically weak minerals. It was shown that the total strength of a rock is highly dependent on the strength of the weakest phase inherited (e.g. Handy, 1990), which makes phyllosilicates a key mineral in deformation. In most of these tectonic processes the primary orientation of the phyllosilicates in the rock to-be-deformed is of major importance as it can ease or hamper the deformation. Therefore, the knowledge of the shape preferred orientation and texture is of major importance in understanding tectonic processes and their localization. Furthermore, it influences the rock's physical properties which are important to a variety of different disciplines besides structural geology, e.g. geophysics or material sciences. Therefore, understanding how preferred orientation of phyllosilicates develops has impact in a wide scientific field.

Hence, texture analysis in phyllosilicate-rich rocks is a well-established field in geosciences. The term texture describes the orientation distribution of crystallites in a polycrystalline material (Bunge, 1986). Other synonymously used terms are crystallographic preferred orientation (CPO) or lattice preferred orientation (LPO). Analysis of the crystallographic preferred orientation has a long tradition especially in materials sciences where it is used to characterize e.g. metals and alloys and their properties (e.g. Kocks et al., 1998). Methods applied for texture analysis have evolved over time, from U-stage microscopy to X-ray and neutron diffraction and most recently electron backscatter diffraction (EBSD) using a scanning electron microscope (SEM). Despite this evolution the textures of some phyllosilicates are still beyond the limits of measurability, due to e.g. intra-lattice water, sample preparation or grain size issues.

Synchrotron radiation, i.e. high-energy X-rays generated in a particle accelerator, overcomes some of these restricting issues as it is insensitive to water, does not require a high sample preparation effort and is sensitive to grain sizes down to nanometer-scale.

In this study synchrotron diffraction was applied to explore the quantitative textures of phyllosilicates and accompanying minerals in three case studies. These case studies concern three different tectonic settings posing different problems to conventional texture analysis: (1) clay minerals, chlorites, and micas in black shales span over a large range of grain sizes, (2) clay samples from the frontal prism and slope of a convergent margin yield water in swelling minerals and voids, and (3) serpentinite samples from the spreading center at the mid-Atlantic ridge with unique crystallographies of the mineral phases. These examples extend the limits

of quantitative texture analysis of phyllosilicates and allow the understanding of particular geological processes in more detail.

## 1.2. Thesis Structure

This thesis is organized in six chapters, supplemented by an appendix. Chapter 1 gives an introduction on the topic and the objective of this thesis. The chapter provides a short background and explains the aim of this thesis and the thesis structure. The appearance and significance of phyllosilicates and their texture formation are presented. Chapter 2 introduces the method synchrotron diffraction for rock texture analysis and explains the advances achieved in this thesis. Chapter 3 is a manuscript in revision at *Tectonophysics* with the title "Quantitative comparison of microfabric and magnetic fabric in black shales from the Appalachian plateau (western Pennsylvania, U.S.A.)". This study uses different methods, such as synchrotron texture analysis, microstructure analysis and anisotropy of the magnetic susceptibility (AMS), which describe the fabric of Devonian black shales. From the measured texture an AMS is calculated and compared to the measured AMS values. Chapter 4 is a manuscript in revision at the *Journal of Geophysical Research: Solid Earth* with the title "Texture development of clay-rich sediments entering the Costa Rica subduction zone". Within this chapter the texture of wet, soft, clay-rich mud and mudrock samples is determined using synchrotron diffraction. The results are linked to tectonic activity in the slope offshore Costa Rica. Chapter 5 is a manuscript nearly ready for submission with the title "Textures in serpentinites from the Atlantis Massif, Mid-Atlantic Ridge". This chapter explores the textures of serpentinite samples with synchrotron diffraction and explains texture development based on microstructural observations. Chapter 6 summarizes and discusses the results of the three manuscripts and draws a final conclusion.

## 1.3. Texture formation in phyllosilicate-bearing rocks

Phyllosilicates or sheet silicates represent one of the five silicate mineral groups. In general sheet silicates consist of alternating layers of tetrahedra and octahedra sheets. $SiO_4$-tetrahedra are connected layer-wise by sharing three of their oxygen ions with the adjacent tetrahedron and thus form relatively stable sheets. In octahedral layers the tetrahedrons additionally share the fourth oxygen with the next, reversely arranged layer. These layers can be stacked and in between cations can find their lattice position. Phyllosilicates exhibit a strong cleavage in one direction parallel to the basal layers. This leads to a platy morphology and strong shape anisotropy of certain crystallites. When distributed in a preferred orientation within a rock they can introduce a special appearance to a rock, like slaty cleavage in slates and schists.

Phyllosilicate minerals occur in all rock groups, in magmatic rocks most often as biotite or muscovite, in sedimentary rocks for example as clay minerals and in metamorphic rocks e.g. as micas. Therefore, they can take part in all kinds of geologic processes. They play a major role in fault and shear zones and are significant also in other tectonic processes.

As mentioned above, phyllosilicates appear in many different kinds of rocks. Due to their largely developed shape anisotropy as platy minerals, the formation of a preferred orientation is very likely for phyllosilicates when exposed to any kind of stress. Of course, in different rocks different processes can contribute to the evolution of texture. Generally, texture is considered to be generated by intra-crystalline plastic deformation (e.g. Almqvist and Mainprice, 2017; Passchier and Trouw, 2005) and commonly applied as an indicator for ductile deformation. Besides deformation, other processes exist which lead to texture formation in rocks like sedimentation and burial or brittle faulting.

While clay minerals are mostly random oriented during descent and first deposition on the ground, especially when flocculated, this changes during further burial (e.g. Oertel, 1983). With increasing overburden, compression and dewatering the parallel alignment will increase (Figure 1.1a). This is mainly realized by rigid-body rotation and intergranular slip (Oertel, 1983). During this process grain contacts change from dominant edge-to-edge (EE) over edge-to-face (EF) to more face-to-face (FF) grain contacts (e.g. Bennett and Hulbert, 1986). Due to the shape anisotropy of phyllosilicates, this process leads to preferred alignment and hence texture formation.

In metamorphic rocks texture formation occurs mostly in combination with deformation, but in rare cases also static recrystallization in combination with remineralization can lead to texture formation, e.g. if there was already a texture in the precursor rock.

As already mentioned, deformation is an important texture forming process affecting phyllosilicates, either brittle or ductile. In brittle fault gouges, phyllosilicates, especially clay minerals align parallel to the fault geometry either by rigid body rotation or by recrystallization (Figure 1.1b). While fault gouges in experiments can show a strong preferred orientation, those observed in nature mostly show only weak alignment (e.g. Haines et al., 2009). At elevated temperatures rocks deform ductile by intra-crystalline plastic deformation. In phyllosilicates this is mainly realized by basal glide (Figure 1.1c). Biotite, for example, deforms mainly by dislocation slip on either (001)<110> or (001)[100] (e.g. Kronenberg et al., 1990).

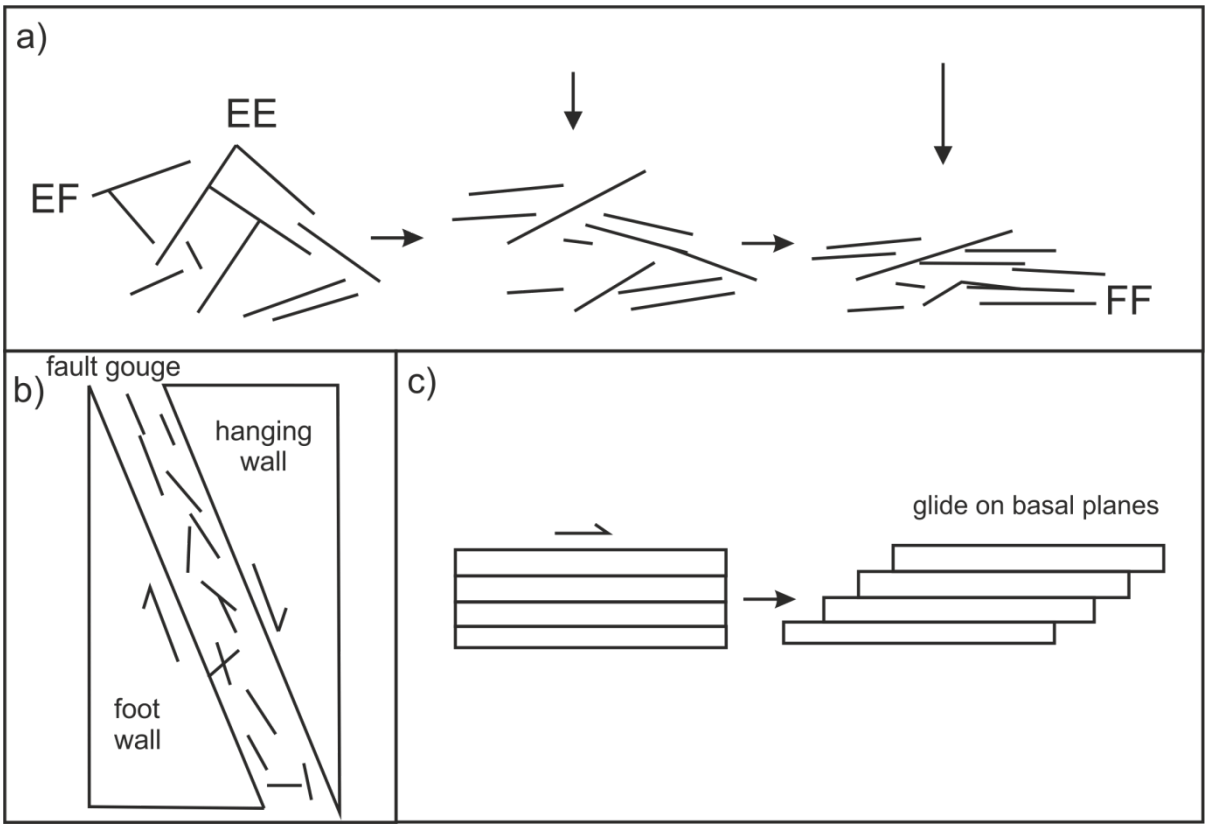


*Figure 1.1. Different texture forming processes affecting phyllosilicates and phyllosilicate-rich rocks a) alignment of phyllosilicates during sedimentation and burial modified from* Moon and Hurst (1984) *b) alignment in fault gouges modified from* Haines et al. (2009) *c) realization of ductile intra-crystalline deformation as slip on basal planes*

The results of texture analysis are commonly visualized as pole figures, which are directional projections of the statistical distribution of the spatial orientation of crystal lattice plane normals. While isotropic aggregates are statistically random, texture intensities can be measured in multiples of random distribution (mrd) (Bunge, 1986).

Due to the crystallographic structure of some minerals physical properties can be different in the different directions of a single crystal leading to anisotropic physical behavior. In polycrystalline aggregates in which the anisotropic axes of a certain mineral phase are aligned, i.e. the mineral phase has a texture, this leads to anisotropy of the rock. So, using the intrinsic physical properties of the minerals inherited and the texture of a rock, its anisotropy can be estimated. Almqvist and Mainprice, (2017) mentioned that micas and clay minerals are the most anisotropic mineral phases with regard to their elastic constants and also for the anisotropy of the magnetic susceptibility the preferred orientation of mica is a well-known issue (Biedermann et al., 2014; Siegesmund et al., 1995). This emphasizes the significance of phyllosilicate textures for rock physical properties.

## References

Almqvist, B.S.G., Mainprice, D., 2017. Seismic properties and anisotropy of the continental crust: Predictions based on mineral texture and rock microstructure. Rev. Geophys. 55, 367–433. doi:10.1002/2016RG000552

Bennett, R., Hulbert, M., 1986. Clay Microstructure. International Human Resources Development Corporation, Boston, pp.161.

Biedermann, A.R., Bender, C., Lorenz, W.E.A., Hirt, A.M., 2014. Low-temperature magnetic anisotropy in micas and chlorite. Tectonophysics 629, 63–74. doi:10.1016/j.tecto.2014.01.015

Bunge, H.J., 1986. General Outline and Series Expansion Method, in: Bunge, H.J., Esling, C. (Eds.), Quantitative Texture Analysis. DGM Informationsgesellschaft, Oberursel, pp. 1–72.

Haines, S.H., van der Pluijm, B.A., Ikari, M.J., Saffer, D.M., Marone, C., 2009. Clay fabric intensity in natural and artificial fault gouges : Implications for brittle fault zone processes and sedimentary basin clay fabric evolution. J. Geophys. Res. - Solid Earth 114, B05406. doi:10.1029/2008JB005866

Handy, M.R., 1990. The solid-state flow of polymineralic rocks. J. Geophys. Res. - Solid Earth 95, 8647–8661. doi:10.1029/JB095iB06p08647

Kocks, U.F., Tomé, C.N., Wenk, H.R., 1998. Texture and Anisotropy. Cambridge University Press, Cambridge, pp. 676.

Kronenberg, A.K., Kirby, S.H., Pinkston, J., 1990. Basal slip and mechanical anisotropy of biotite. J. Geophys. Res. Solid Earth 95, 19257–19278. doi:10.1029/JB095iB12p19257

Moon, C.F., Hurst, C.W., 1984. Fabrics of muds and shales: an overview. Geol. Soc. London Spec. Publ. 15, 579–593.

Oertel, G., 1983. The relationship of strain and preferred orientation of phyllosilicate grains in rocks - a review. Tectonophysics 100, 413–447. doi:10.1016/0040-1951(83)90197-X

Passchier, C.W., Trouw, R.A.J., 2005. Microtectonics. 2nd Ed. Springer, Berlin. pp. 366.

Shea, W.T., Kronenberg, A.K., 1992. Rheology and deformation mechanisms of an isotropic mica schist. J. Geophys. Res. Solid Earth 97, 15201–15237. doi:10.1029/92JB00620

Siegesmund, S., Ullemeyer, K., Dahms, M., 1995. Control of magnetic rock fabrics by mica preferred orientation: a quantitative approach. J. Struct. Geol. 17, 1601-1605 doi:10.1016/0191-8141(95)00047-H

# 2. Synchrotron diffraction for rock texture analysis

Using synchrotron diffraction for texture analysis has several advantages compared to other texture determining methods, like common lab X-ray sources, neutron diffraction or electron backscatter diffraction. Due to the high energy of synchrotron radiation it can also penetrate absorbing materials to a large extent and allows a quantitative volume measurement. Thereby, the beam is not absorbed by hydrogen, e.g. in water-containing structures and can therefore be used for wet samples or samples incorporating minerals rich in water. Furthermore, sample preparation is kept to a minimum, as no polishing or other surface treatment is needed. Besides, it is a non-destructive method.

## 2.1. Experimental setup

Today synchrotron diffraction is available in large research facilities, e.g. at the European Synchrotron Radiation Facility (ESRF) in Grenoble, France or at the German Electron Synchrotron (DESY) in Hamburg, Germany.

To generate synchrotron radiation electrons are accelerated to a speed close to the speed of light. They travel in a circular or circle-like electron guide consisting of vacuum tubes and magnets which keep the electrons on the correct path. When the electrons leave a straight line of travel, i.e. curve, they change their speed and thereby emit synchrotron radiation, i.e. bremsstrahlung, which is then used for experiments. The energy and direction of the synchrotron beam can be modulated by filters, monochromators and mirrors (e.g. Cockcroft and Fitch, 2008).

Synchrotron texture analysis is applicable at beamlines built for powder diffraction as they are equipped with the necessary experimental setup. The measurements are conducted in transmission mode, with the beam hitting the sample directly and the diffracted beam leaving the sample towards an area detector behind the sample (Figure 2.1).

The detector image includes the diffractions of all crystal lattice planes hit by the beam. As the sample is rotated about the cylinder axis by 175° in 5° steps full pole figure coverage is achieved.

Due to the high intensity and collimation of the beam, the size of the synchrotron beam is restricted to only a small aperture, which ranges between 500 µm and 1 mm. Thus, only a limited number of grains diffract in one measurement. Absorption effects can affect samples with a diameter >2 mm in transmission. This limits samples to a size which is too small for most geological samples, to reach a statistically sufficient number of diffracting grains. Additionally, grain size can vary over a large range and might be heterogeneous throughout geological samples.

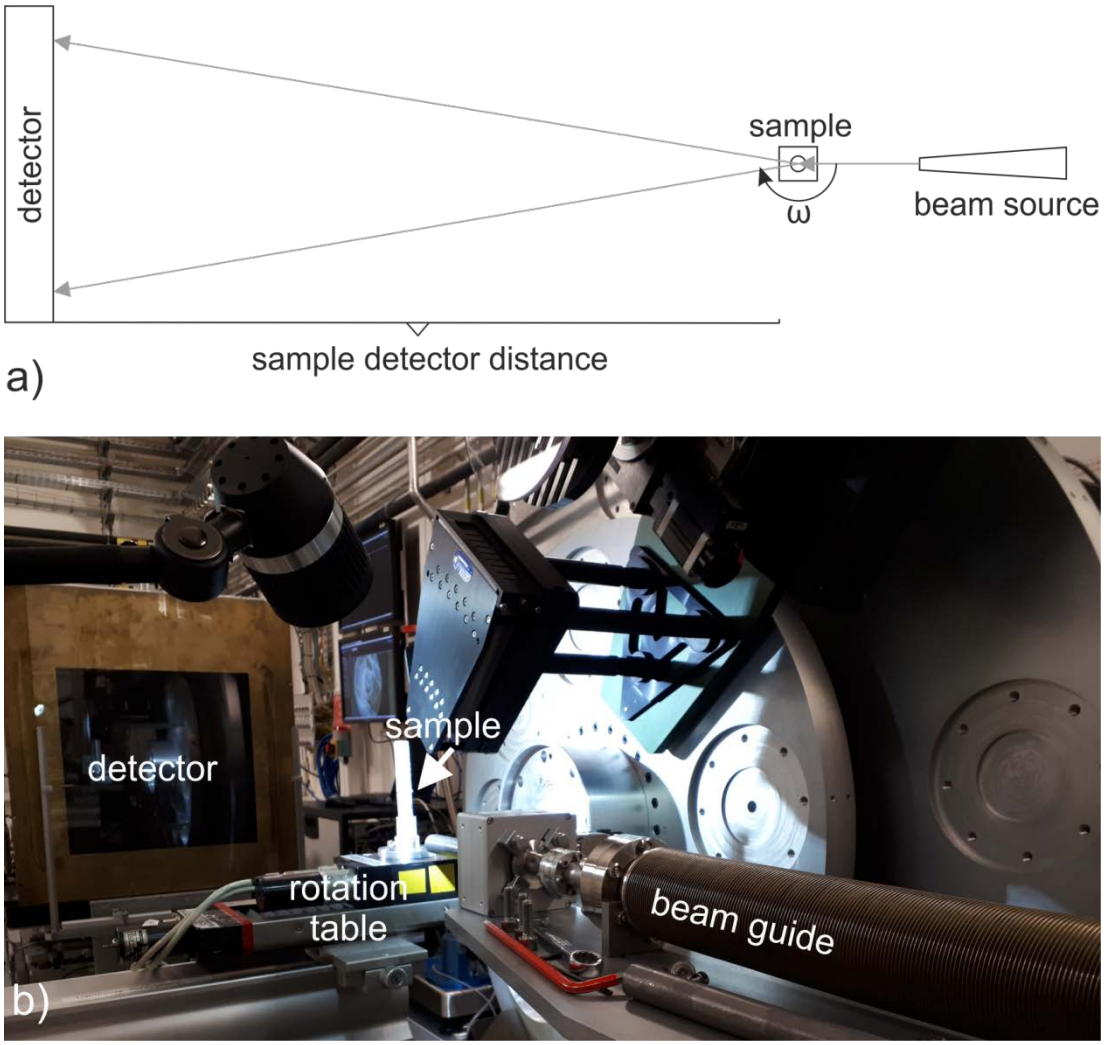


*Figure 2.1. Experimental setup for synchrotron texture measurements a) general experimental setup b) experimental setup at beamline ID22, ESRF*

To overcome the restrictions posed by the small beam size, previous measurement strategies for geological samples as applied by e.g. Lutterotti et al. (2014) and Schumann et al. (2014) were advanced. Two aspects were considered, when planning the measurements: First, the utilization of cylindrical samples with a certain diameter, which was already applied by Schumann et al. 2014, was adopted. Second, several “slices” of the samples were measured, increasing the number of diffracting grains.

An increase in sample thickness has three effects for the peaks in the resulting diffraction pattern: 1.) intensity decreases 2.) peak broadening leads to a degradation in 2Θ resolution which complicates refinements, especially for phyllosilicate-rich samples with a high amount of overlapping diffractions 3) background increases. For bulk rock texture analysis, it is necessary to find the right balance between grain statistics and intensity. Therefore, the applicability of larger sample thicknesses for the texture evaluation after Rietveld Refinement is important. To experimentally determine the maximum sample thickness for our sample type, a test series of Opalinus clay samples with different diameters was measured.

## 2.2. Sample diameter

To test the influence of the sample diameter on the measurement results experimentally, a fine grained sample set from the Jurassic Opalinus formation (Dogger alpha), was used. The sample set originates from the tunnel drilling project of the “Scheibengipfeltunnel” at the northern rim of the Swabian Alb in southern Germany (kindly provided by Prof. Dr. Lempp, Halle University). The shale is composed from mica, chlorite, quartz and calcite, and described as homogeneous (Lempp et al., 2016).

Six samples with different diameters were used: 2 mm, 5 mm, 10 mm, 15 mm, 27 mm, and 50 mm. For all samples the same experimental settings were used (wavelength λ=70 keV, sample detector distance=1401 mm, beam size = 1 mm). Measurements were conducted at beam line ID22 at the ESRF.

Comparing the integrated results of the differently sized samples we can clearly see the loss in intensity, the peak broadening and the increase in background (Figure 2.2) with increasing sample diameter. It can be already seen that the prepared samples are not totally homogeneous in composition and texture as well as peak heights vary. There are slight variations due to the natural sample material.

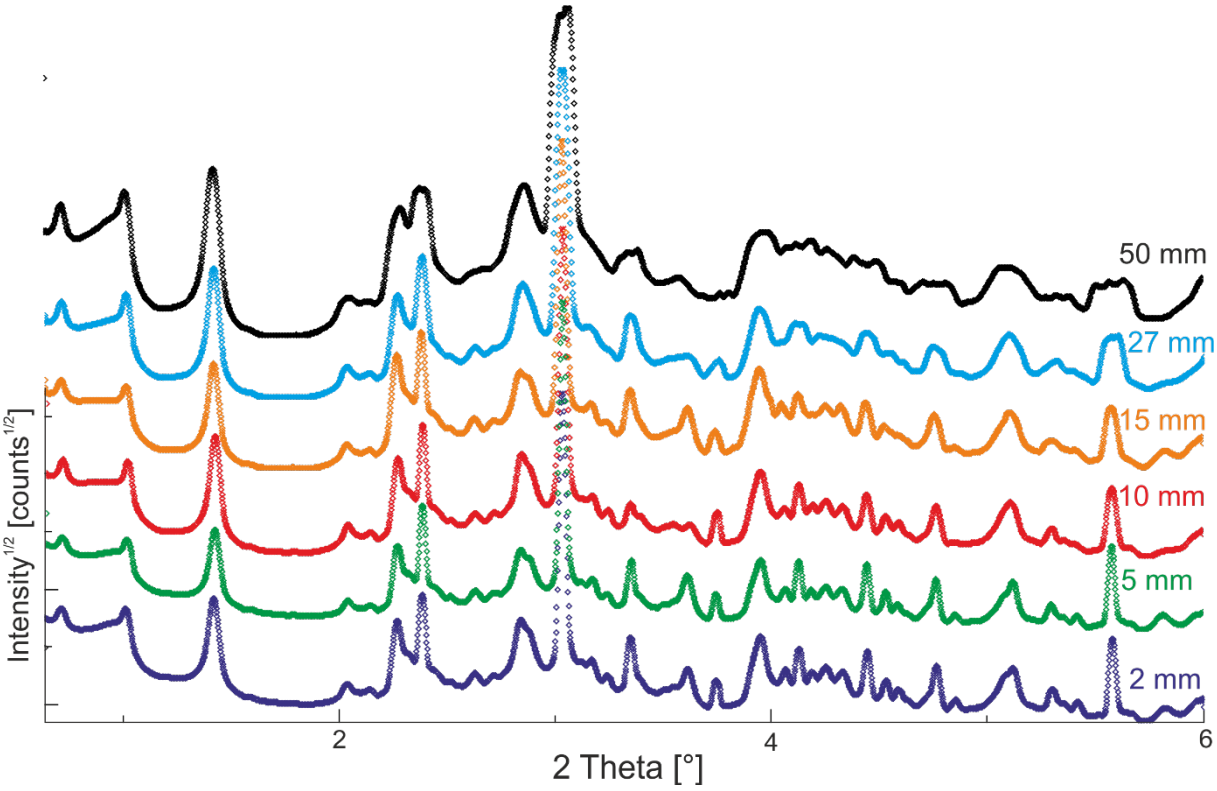


*Figure 2.2. Comparison of diffraction patterns integrated from 2D detector images, measured in transmission on Opalinus clay for different sample diameters.*

To test the reproducibility of the sample texture, Rietveld texture analysis was performed on samples with different diameter. The pole figures recalculated from the different diffraction patterns are shown in Figure 2.3.

Pole figures of the inherited phyllosilicates in all samples show a single maximum for the basal plane normal perpendicular to the foliation reflecting pure flattening strain, while the a-axes form a foliation parallel girdle. The distribution of the maxima within this girdle is comparable between the different samples. The maximum intensities vary for the different phases. Illite has the strongest intensity in all samples, ranging from 9.3 mrd (15 mm sample) to 12 mrd (27 mm sample) for the basal planes maximum. Kaolinite basal planes maximum ranges from 5.6 mrd (5 mm sample) to 7.5 mrd (27 mm sample). Chlorite basal planes maximum is weakest in the 5 mm sample with 5.1 mrd and strongest in the 50 mm sample with 7.5 mrd.

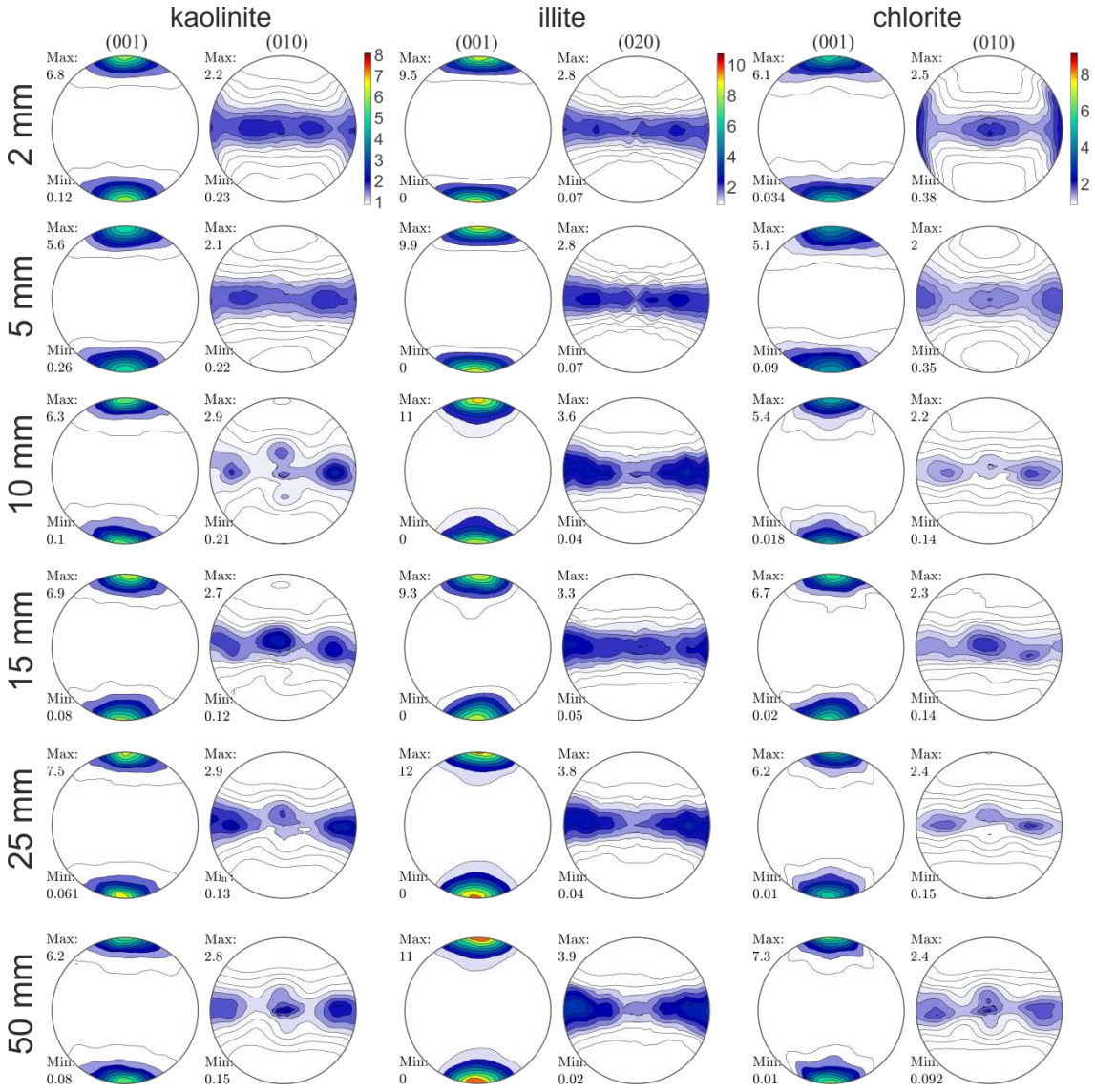


*Figure 2.3. Recalculated pole figures of the phyllosilicates resulting from the evaluation of the diffraction data of the samples with different diameter. Equal area, lower hemisphere projection. Maxima in mrd.*

The total intensity and the texture index F2 (Bunge, 1986) are used as indicators and compared in all samples. A slight variety is attributed to minor compositional changes and therefore tolerated. As no systematic de- or increase of these indicators can be observed, the mean is considered to represent the real texture. Frequent outliers regarding the intensity were found in the 5 mm, 25 mm, and 50 mm sample. Frequent outliers regarding the texture index F2 were found in the 2 mm and 50 mm samples. Considering the results and trying to keep the samples as large as possible, it was decided to use samples with a diameter of about ~15-20 mm for synchrotron texture measurements for the beamlines and sample material analyzed in this study. Of course, the sample diameter also strongly depends on the wavelength λ and the composition of the sample material.

## 2.3. Further improvements and workflow

A second possibility to increase the number of measured grains was to measure several positions along the cylinder axis in each sample, further called slices. Depending on sample homogeneity and grain size different numbers of slices were measured and analyzed.

In samples with certain mineralogy, it might be necessary to determine the mineralogy in advance, especially when analyzing clay minerals.

The application of these methodical aspects lead to the implementation of a certain workflow (Figure 2.4) applied to the case studies within this thesis.

First, the sample composition is estimated depending on the nature of the sample and previous studies on the same or similar material. If the mineral composition is straightforward with only a small number of phases which are clearly defined, this information is sufficient for the texture analysis. But if the composition is more complex, with a large number of phases which might be more complicated regarding their mineral chemistry or overlapping diffractions in the diffraction pattern, additional analyses like X-ray powder diffraction or microscopic analyses are necessary to determine the composition. When the composition is known, the grain size is determined, either from macroscopic observations or using the analyses previously run for mineral determination. If the grain size is relatively fine and homogeneous, i.e. is not visible with the unaided eye, measuring one to three sample slices is sufficient for quantitative texture analysis. If the grain size is coarser or the fabric is more heterogeneous, the measurement of multiple slices is necessary for quantitative texture analysis. The measured slices are then analyzed separately and the resulting pole figures are averaged and summed up at the end of the analysis procedure, giving a representative texture for this sample.

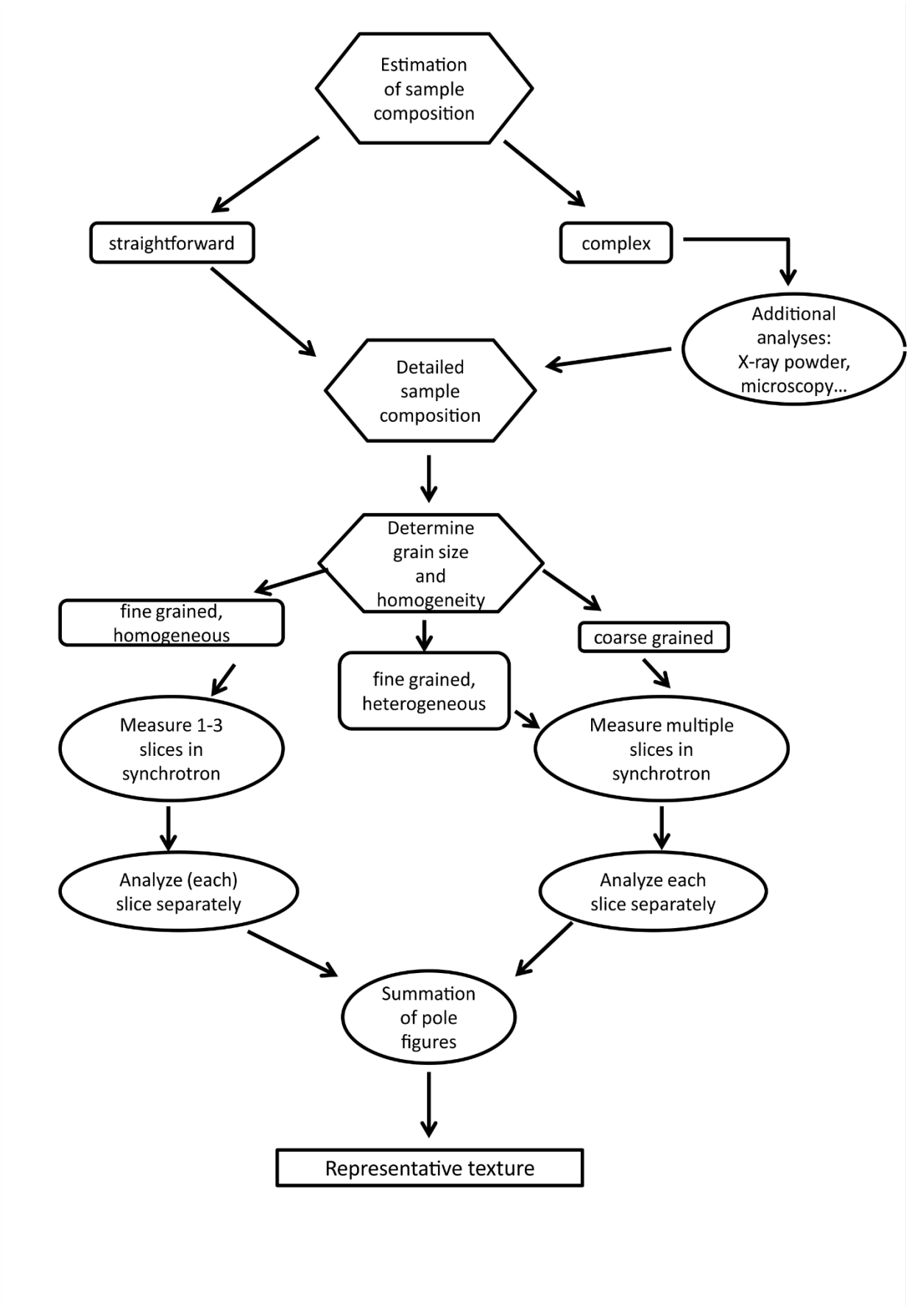


*Figure 2.4. Workflow for advanced quantitative synchrotron texture analysis of bulk rock samples*

## 2.4. Data refinement

The 36 detector images from each measurement are then converted into *tif images using the Fit2D (Hammersley, 1998) software. An average image is created and used for a first refinement. The refinement is conducted using the Rietveld code MAUD (Material Analysis Using Diffraction) (Lutterotti et al., 1997). MAUD integrates 72 individual diffraction patterns from each image which will then be used for the refinement (Figure 2.5). To model a diffraction pattern, which can then be refined, the incorporated mineral phases with the correct crystallography are required. Those are *cif files from the COD (Grazulis et al., 2009) and AMCDS (Downs and Hall-Wallace, 2003) data bases. The following parameters were used for a first refinement: sample specific parameters like background and scale parameters, instrumental parameters like intensity, wave length and beam center. Further crystallographic parameters, i.e. the unit cell dimensions and axes, were refined, followed by microstructural parameters like microstrain and grain size.

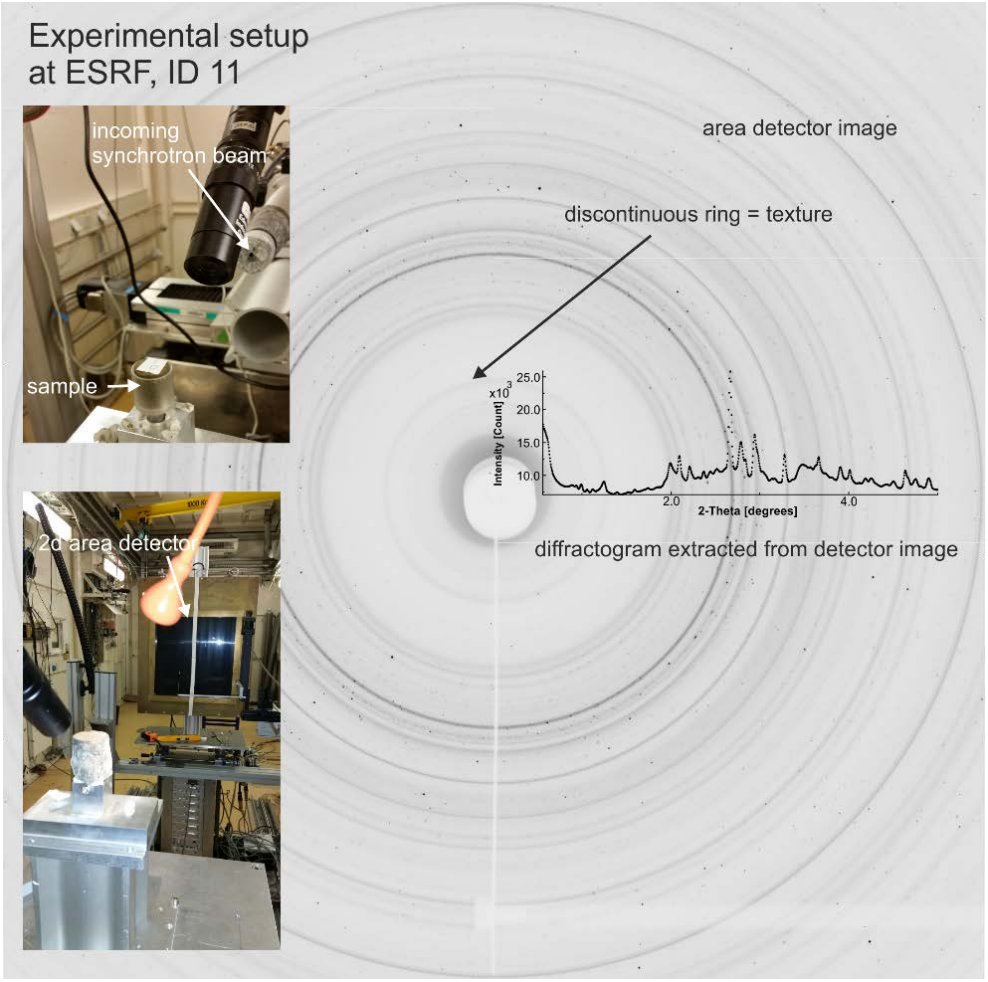


*Figure 2.5. Area detector image of a clay sample recovered at European Synchrotron Radiation Facility, Grenoble (France) ID11 and experimental beam line setup.*

After the first refinement, the average file is replaced by the 36 single images in 5° steps to perform the texture calculation. A texture is induced, using the EWIMV algorithm. This algorithm is implemented in the software MAUD and derived from WIMV (Matthies and Vinel, 1982). The background and scale parameters of the individual images are refined again and the texture is calculated. If necessary, additional parameters of the above described are further refined. By comparing the measured and the modeled data, the quality of the refinement can be visually checked (Figure 2.6).

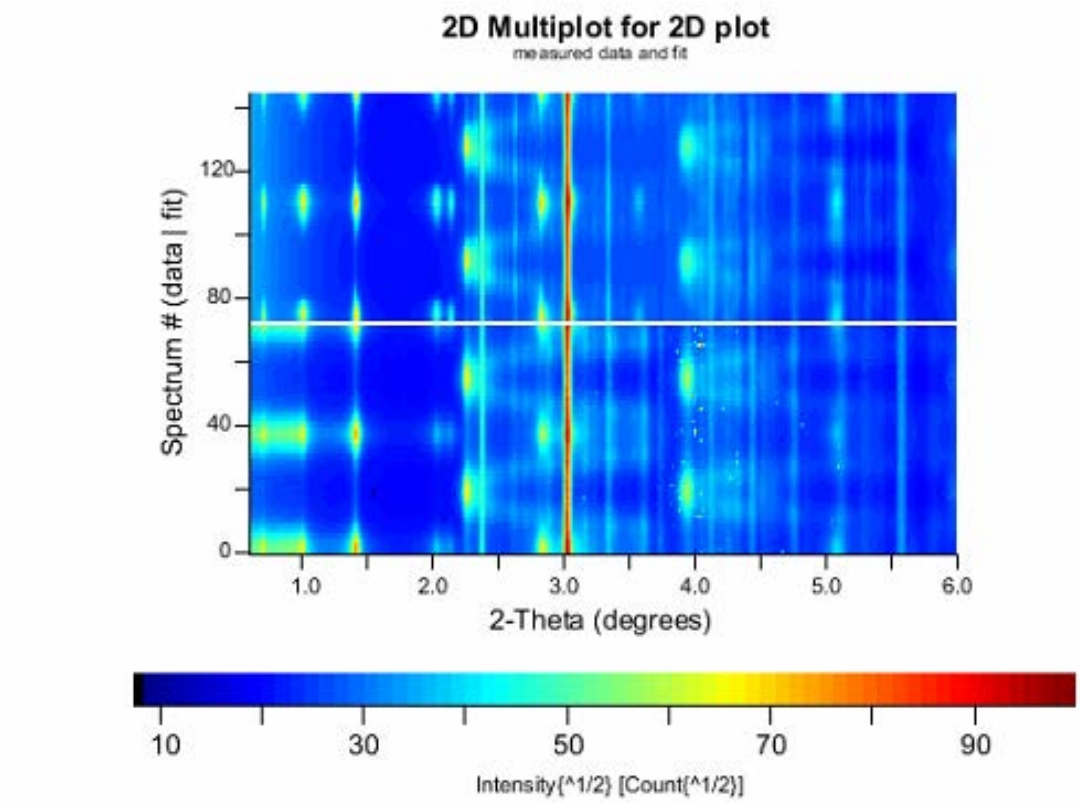


*Figure 2.6. Exemplary 2D Multiplot in MAUD of the 15mm diameter sample showing good agreement between measured and modeled texture*

Pole figures can then be extracted from the MAUD software and imported and treated with other pole figure data programs like Pole Figure Plot (Umlauf and Ullemeyer, 2012) or the Matlab toolbox MTEX (Hielscher and Schaeben, 2008).

Useful Rietveld refinement strategies for texture analysis can be found in Lutterotti et al. (2014); Schumann (2013); Wenk et al. (2014). Advices regarding the treatment of special delicate samples, like e.g. clays, as applied in this thesis are summarized in Appendix A1.

## References

Bunge, H.J., 1986. General Outline and Series Expansion Method, in: Bunge, H.J., Esling, C. (Eds.), Quantitative Texture Analysis. DGM Informationsgesellschaft, Oberursel, pp. 1–72.

Cockcroft, J.K., Fitch, A.N., 2008. Experimental Setups, in: Dinnebier, R.E., Billinge, S.J.L. (Eds.), Powder Diffraction: Theory and Practice. The Royal Society of Chemistry, Cambridge, pp. 20–56.

Downs, R.T., Hall-Wallace, M., 2003. The American Mineralogist crystal structure database. Am. Mineral. 88, 247–250.

Grazulis, S., Chateigner, D., Downs, R.T., Yokochi, A.F.T., Quirós, M., Lutterotti, L., Manakova, E., Butkus, J., Moeck, P., Le Bail, A., 2009. Crystallography Open Database - An open-access collection of crystal structures. J. Appl. Crystallogr. 42, 726–729. doi:10.1107/S0021889809016690

Hammersley, A.P., 1998. FIT2D V9.129 Reference Manual V3.1. Inter Rep ESRF98HA01. Grenoble.

Hielscher, R., Schaeben, H., 2008. A novel pole figure inversion method: specification of the MTEX algorithm. J. Appl. Crystallogr. 41, 1024–1037. doi:10.1107/S0021889808030112

Lempp, C., Menezes, F., Sachwitz, S., 2016. Tonstein als Wirtsgestein: En geomechanischer Beitrag über Opalinuston. geotechnik 39, 235–251. doi:10.1002/gete.201500025

Lutterotti, L., Matthies, S., Wenk, H.-R., Schultz, A.S., Richardson, J.W., 1997. Combined texture and structure analysis of deformed limestone from time-of-flight neutron diffraction spectra. J. Appl. Phys. 81, 594–600. doi:10.1063/1.364220

Lutterotti, L., Vasin, R., Wenk, H.-R., 2014. Rietveld texture analysis from synchrotron diffraction images I. Calibration and basic analysis. Powder Diffr. 29, 76–84. doi:10.1017/S0885715613001346

Matthies, S., Vinel, G.W., 1982. On the Reproduction of the Orientation Distribution Function of Texturized Samples from Reduced Pole Figures Using the Conception of a Conditional Ghost Correction. Phys. status solidi 112, K111–K114. doi:10.1002/pssb.2221120254

Schumann, K., 2013. Strength, textures, microfabrics and acoustic properties of active plate margin sediments on- and offshore SW Japan. PhD thesis. Christian-Albrechts-Universität Kiel.

Schumann, K., Stipp, M., Leiss, B., Behrmann, J.H., 2014. Texture development in naturally compacted and experimentally deformed silty clay sediments from the Nankai Trench and Forearc, Japan. Tectonophysics 636, 125–142. doi:10.1016/j.tecto.2014.08.005

Umlauf, C., Ullemeyer, K., 2012. Pole Figure Plot.

Wenk, H., Lutterotti, L., Kaercher, P., Kanitpanyacharoen, W., Miyagi, L., Vasin, R., 2014. Rietveld texture analysis from synchrotron diffraction images . II . Complex multiphase materials and diamond envil cell experiments. Powder Diffr. 29, 220–232. doi:10.1017/S0885715614000360

# 3. Quantitative comparison of microfabric and magnetic fabric in black shales from the Appalachian plateau (western Pennsylvania, U.S.A.)

* in revision as Kuehn, R., Hirt, A.M., Biedermann, A. R., Leiss, B. at *Tectonophysics*

## Abstract

Anisotropy of magnetic susceptibility (AMS) has been shown to be a good proxy for crystallographic preferred orientation (texture). However, it is not clear in detail how different factors, e.g. modal composition and preferred orientation, define the total AMS in a rock. Black shale samples from a drill core on the Appalachian Plateau in western Pennsylvania were analyzed with respect to their microfabric as determined by texture and microstructure, and AMS. Low- and high-field AMS, which was measured at room temperature, reveals that the AMS of the samples is dominated by the para- and diamagnetic phases. Synchrotron diffraction was applied to determine the texture of all relevant mineral phases incorporated in the samples. Muscovite and chlorite pole figures show single maxima perpendicular to the foliation, reflecting dominant flattening strain. From these textures and the modal compositions, AMS models were calculated using the intrinsic magnetic anisotropy of the single crystals. The modeled and measured AMS are comparable in terms of their principal directions and shapes of the anisotropy ellipsoid for the dominantly paramagnetic samples, with the maximum susceptibility axes oriented subhorizontal to the NE-SW. Both textures and AMS indicate that the samples have undergone largely bedding compaction with a weak tectonic overprint linked to the Alleghenian orogeny. The AMS modeling from the textures demonstrates how the contribution of the intrinsic AMS of each mineral controls the AMS of the whole rock.

## 3.1. Introduction

The magnetic fabric of a rock is determined by the intrinsic magnetic susceptibility of the minerals incorporated and their texture (e.g. Hirt and Almqvist, 2011). We use the term texture synonymously for crystallographic preferred orientation, in the way it is also used in materials science (e.g. Bunge, 1986, Leiss and Ullemeyer, 1999). Features, such as mineral phase distributions, grain boundary configurations, grain intergrowth, veins, voids or cracks, are described as the microstructure of the rock. The term microfabric considers both, texture and microstructure.

Determining the texture of rocks containing clay-sized phyllosilicates can be challenging for several reasons. Depending on the sensitivity of the material and its components, the preparation can be difficult because the microfabric might be destroyed during preparation, e.g. polishing, which is necessary for electron backscatter diffraction. The grain size of some

particles might be too small to be resolvable with optical methods. In addition, as some clay minerals have similar crystallographic structures, diffraction reflections can overlap, which makes Rietveld Refinement (Rietveld, 1969) mandatory.

The relationship between texture and anisotropy of magnetic susceptibility (AMS) has long been observed since Fuller (1960) discovered that the preferred orientation of mica long axes coincides with the long axis of the AMS ellipsoid. Since then, texture and AMS have been qualitatively compared in numerous studies (e.g. Balsley and Buddington, 1960; Cifelli et al., 2005; Graham, 1954; Hirt et al., 2004; Kligfield et al., 1983; Lüneburg et al., 1999; Schmidt et al., 2007), but attempts to quantitatively link a measured texture with intrinsic mineral AMS have been shown to be complex and dependent on a number of factors, e.g., mineralogy and deformation fabric (cf. Borradaile and Jackson, 2010). Because several mineral subfabrics contribute to the magnetic anisotropy in a rock, it is important to understand how different magnetic subfabrics can either enhance or interfere with one another (e.g. Biedermann et al., 2018, 2015; Hirt and Almqvist, 2011).

First measurements of magnetic anisotropy in the Appalachian plateau in New York and Pennsylvania were conducted by Graham (1966). During the 1980's, work on the anisotropy of the rocks' physical properties in the Appalachian area attracted considerable attention (e.g. Engelder and Engelder, 1977, Evans, 1989; Evans et al., 1989a, 1989b), especially due to exploration interests for gas and oil by industry under the US Department of Energy's Eastern Gas Shales Project (Cliffs Minerals Inc., 1982) (Figure 3.1). Devonian strata were recovered under this program from a series of cores along the Appalachian Plateau between Virginia and New York. In Pennsylvania, the Devonian rocks consist of prodeltaic turbiditic siltstones and mudstones, which alternate between black and grey, depending on organic content. At the bottom of the sequence is the Onondaga limestone, which is overlain by calcareous siltstones that grade into limestones, as with the Tully limestone. The calcareous contribution disappears in the upper Genesee Group as more quartzitic clastics become common in the Cashaqua and Rhinestreet formations.

Hirt et al. (1995) analyzed Devonian black shales from the Appalachian Plateau in New York and showed a consistency in orientation of the AMS with chlorite textures determined by Evans et al., (1989b). Other observed strain indicators, such as the direction of fast P-wave velocity and fabric-controlled stress-relief microcrack orientation, are also parallel to the direction of the maximum susceptibility (Evans et al., 1989b; Meglis and Engelder, 1994).

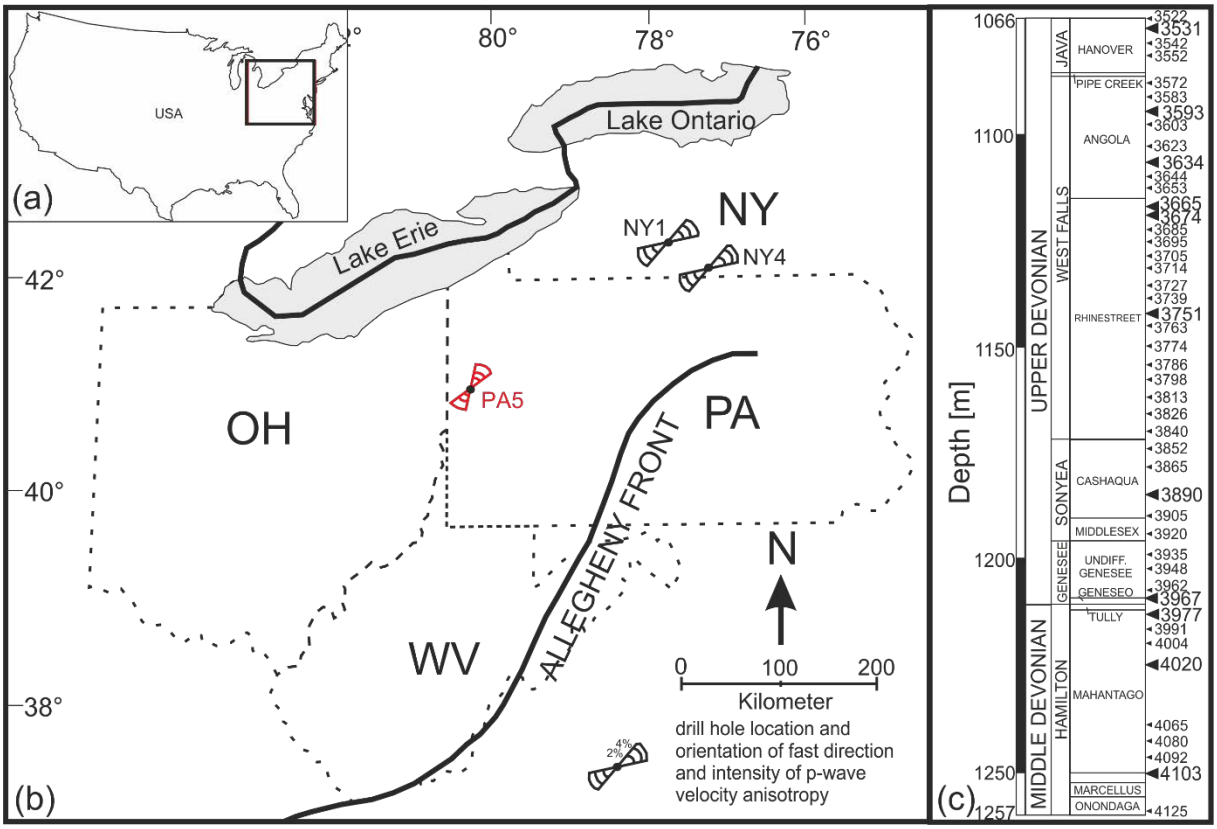


*Figure 3.1. Drilling location and stratigraphy of well PA5: a) overview of map, b) map with drilling location in western Pennsylvania. Additionally, the two drill sites referred to in Hirt et al. (1995) are plotted. Orientation and intensity of the P-wave velocity anisotropy is indicated (data from Evans et al. (1995b) OH: Ohio, PA: Pennsylvania, NY: New York, WV: West Virginia. The Allegheny front line marks the farthest tectonically influenced front during Alleghenian orogeny. c) Devonian stratigraphy in core PA5 and sampling depths of samples, circles indicate samples for low-field AMS, and arrows samples used for texture and high-filed AMS.*

A drop in compaction degree was observed at the base of Rhinestreet formation, which is associated with overpressure in the Rhinestreet formation and an increase of stress in the Tully limestone (Evans et al., 1989a). Since these studies, research on texture and magnetic fabrics has developed further. The concept of different magnetic subfabrics has led to a development of numerous methods to differentiate e.g. paramagnetic, ferromagnetic (*s.l.*) and diamagnetic contributors to the total AMS (e.g. Borradaile and Henry, 1997; Martin-Hernandez and Ferre, 2007). Information on the intrinsic AMS of paramagnetic minerals has advanced sufficiently (Biedermann et al., 2014; Schmidt et al., 2007; Martín-Hernández and Hirt, 2003), so that it is now possible to model AMS on the basis of the texture and contribution of the incorporated minerals (Biedermann et al., 2018, 2015; Haerinck et al., 2015; Schmidt et al., 2009). In this study, we investigate samples from ~1000 to 1250 m depth (Devonian age) from a drill core in western Pennsylvania (PA5) (Cliffs Minerals Inc, 1982) and analyze samples regarding texture and AMS and compare this data to the neighboring New York cores (NY1 & NY4) from Hirt et al. (1995) (Figure 3.1). To gain texture information on all incorporated phases we use synchrotron texture analysis, which yields the opportunity to use the same sample for

texture measurements and for AMS measurements. From these data, we model the AMS and compare it to the measured data. This establishes a link between observed physical anisotropies and rock microfabric that are influenced by sedimentary and tectonic processes on the Appalachian Plateau. Our results, however, can be extrapolated to other deformed fold belts.

## 3.2. Material

### 3.2.1. Geologic background

The eastern margin of the Laurentian craton evolved due to the break-up of Rodinia 750-725 m.y. ago (Moores, 1991; Powell et al., 1993). A carbonate shelf developed that faced the Theic ocean (Faill, 1997a). This period lasted until the beginning of the Taconic orogeny at ~ 470 Ma (Rankin, 1994), which is marked by the docking and obduction of several Theic terranes on the carbonate shelf (Faill, 1997a). Eastern highlands evolved, which separated the Theic ocean from the craton, and as a reaction to the load of the basement, a basin located northwest of the highlands developed (Faill, 1997b). This basin collected sediments during the Taconic orogeny (Faill, 1997b), and was stable as indicated by widespread evaporitic deposition, such as the Salina Group, until the onset of the Acadian orogeny in the middle Devonian (Williams and Hatcher, 1982). The flysch of this orogenic event was deposited in the basin creating the Catskill Delta formation, which consists of four cycles related to four collisional tectophases (Ettensohn, 1985a). All cycles show the transition from basinal to proximal delta facies, where the black shales represent rapid subsidence and transgression (Ettensohn, 1985b). The deposition of black shales indicates an equatorial near-shore setting of the basin, which enhanced terrestrial nutrient input and thus increased plankton productivity. The organic material is probably preserved due to oxygen depletion and water column stratification. Sedimentation lasted until the Alleghenian orogeny, which was the final collision between Laurussia and Gondwana in the early Permian. The final orogenic event lead to decollement tectonics with westward transport and ca. 10% layer parallel shortening; the Salina salt served as detachment level (Engelder and Engelder, 1977; Evans, 1989). There has been considerable discussion about the direction and timing of layer parallel shortening (LPS) around the Pennsylvania salient on the Appalachian plateau. Studies over the past 20 years favor a single phase of shortening deformation. Gray and Stamatakos (1997) explain differences in shortening direction around the salient as being due to lateral difference in LPS, which leads to vertical axis rotation. Wilkins et al., (2014) on the other hand favor fanning of the NW shortening directions prior to the fold-and-thrust belt, which resulted in an initial arcuate trend of deformation. Mount et al. (2017) also support a constant shortening direction with LPS occurring earlier in the deformation history.

### 3.2.2. Description of core PA5

Well PA5 is located in northeastern Lawrence County, Pennsylvania close to the border of Ohio (Figure 3.1a, b). Bedrock at the drill site consists of lower Pennsylvanian sediments from the Allegheny and Pottsville Groups. There are no major structural features in the area and the Devonian strata show a northeast strike with gentle dipping to the southeast. Coring started at 1073.5 m depth (3522.0 feet) in the Hanover formation and ended at 1274.5 m (4125.8 feet) in the Onondaga limestone, covering 184.0 m of the middle and upper Devonian stratigraphy (Figure 3.1c) (Cliffs Minerals Inc., 1982). Black to grey shales dominate the upper part of the core, but more calcareous-rich sediments are found below the Sonyea Group. Two sets of joints are found in the cored rock with a major trend 280-290° and a secondary trend at 320-330°. The two sets were thought to reflect two separate phases of deformation (Cliffs Minerals Inc., 1982). Seismic anisotropy of p-waves was determined from compressibility and ultrasonic measurements and can reach up to 3% (Evans et al., 1989b).

The diameter of the core is 8.89 cm from which we prepared 2.5 to 4.0 cm thick slices. Two to five cylindrical specimens with 2.54 cm diameter were drilled from each core section and trimmed to 2.3 cm length. A total of 47 sample sections were considered along the length of the core to follow the change in the fabric down core (Figure 3.1c). Note that sample names reflect the depth in feet. Eleven samples, representing the major lithologies in the core, were used for texture and microstructure analysis, as well as high-field torque measurements.

## 3.3. Methods

### 3.3.1. Optical and Scanning Electron Microscopy

Thin sections in three orthogonal directions using foliation and magnetic lineation as references, were prepared for nine samples based on material availability. Due to the small grain size, the usefulness of optical microscopy was limited. For the scanning electron microscopy (SEM) analysis, the thin sections were polished and coated with carbon. Backscatter electron (BSE) analyses were obtained using a FEI QUANTA 200T SEM (spot size: 3, voltage: 15 kV, vacuum: 6.4*10^-6 mbar) equipped with a BSE detector.

### 3.3.2. Synchrotron texture analysis

Texture analysis has been conducted with hard synchrotron X-rays, which offers the possibility to penetrate the whole diameter of the sample cylinders without destruction. Synchrotron experiments were conducted at the German Electron Synchrotron (DESY) in Hamburg at the HASYLAB beamline W2 (DORIS ring) and at Beamline ID22 at the European Synchrotron Radiation Facility (ESRF) in Grenoble, France. The cylindrical cores, which were used for AMS measurements, were measured as full samples in transmission mode, being mounted with the cylinder axis perpendicular to the beam. The samples were rotated 180° about the cylinder

axis, measuring in 5° steps, resulting in 36 images per sample. A marXperts mar345 (DESY) and a Perkin Elmer XRD 1611 (ESRF) image plate detector were used. The beam energy was adjusted to ~100 keV at DESY (corresponding to a wavelength of ~0.127 Å) and ~70 keV at ESRF (~0.177 Å) and the beam size was 1 x 1 mm. We measured ~470 mm³ of the sample volume of each sample. The sample detector distance was adjusted to ~1300 mm (DESY) and 1401 mm (ESRF).

Image plate detector data was transformed into *tif-data using the program FIT2D (Hammersley, 1998). The program was also used to determine the image center from a standard measurement. For a first fitting approach, an average-file was created from the 36 different images. For further analysis, the program MAUD (Materials Analysis Using Diffraction (Lutterotti et al., 1997)) was used, which is a code that employs the Rietveld method (Rietveld, 1969). MAUD applies a least squares fitting approach for polyphase sample materials which fits hypothetical peaks by given crystal lattices of certain minerals to the measured spectrum, and allows to calculate textures using the EWIMV algorithm (derived from WIMV; Matthies and Vinel, 1982). MAUD also allows to calculate textures from shales (Kanitpanyacharoen et al., 2012, 2011; Lutterotti et al., 2010; Omotoso et al., 2006; Vasin et al., 2013; Wenk et al., 2007, 2010). The images were loaded by integrating every image in 5° steps, resulting in 72 different diffraction patterns per image and rotational step, respectively. As we measured 36 images per sample, this leads to a total of 72 x 36 = 2592 spectra per sample measurement. Parameter refinement was performed as described previously (Lutterotti et al., 2014; Schumann et al., 2014; Wenk et al., 2014, 2012). Input phase data (cif-files) was available from the Crystallographic Open Database (Grazulis et al., 2009) and the AMCDS data base (Downs and Hall-Wallace, 2003). The following cif-files were used for the refinements: quartz (Antao et al., 2008), chlorite (Zanazzi et al., 2009), a muscovite for the illite/muscovite compound (Liang and Hawthorne, 1996), calcite (Graf, 1961) and dolomite (Graf, 1961). The innermost diffraction in the detector images, corresponding to the chlorite (001), cannot be used for the refinement, as it is partly covered by the beam stop, which gives the peak an irregular shape and influences the texture calculation. The rear part of the spectra is characterized by multiple overlying peaks of the different phases. As this part is not improving texture calculations, it is excluded.

### 3.3.3. Magnetic anisotropy

Low-field AMS was measured on an AGICO KLY-2 susceptibility bridge, with an applied field of 300 A/m and frequency of 920 Hz. High-field AMS was measured on a home-built torque magnetometer (Bergmüller et al., 1994). Samples were measured in seven fields between 750 mT and 1500 mT, every 30° in three mutually perpendicular planes. Dia-/paramagnetic and

ferrimagnetic subfabrics were isolated using the processing routines outlined in Martin-Hernandez and Hirt (2001).

Magnetic susceptibility can be geometrically represented by an ellipsoid; it is determined by a second-order tensor with the eigenvalues k1 ≥ k2 ≥ k3 and their related eigenvectors. The degree of anisotropy of this tensor can be described by k':

$$k' = \sqrt{\frac{(k1 - kmean)^2 + (k2 - kmean)^2 + (k3 - kmean)^2}{3}}$$

with kmean = (k1+k2+k3)/3 (Jelinek, 1984). The shape of the ellipsoid is described by the parameter U,

$$U = (2k2 - k1 - k3)/(k1 - k3)$$

ranging from -1 (prolate) to 1 (oblate ellipsoid shape) (Jelinek, 1981). We use k' because it allows us to describe the degree of anisotropy for both the full and deviatoric tensors. The magnetic lineation is described by $L_m$=k1/k2 and the magnetic foliation by $F_m$=k2/k3 (Hrouda, 1982). Minerals can be either diamagnetic (e.g. quartz), paramagnetic (e.g. phyllosilicates) or ferromagnetic (*s.l.*) (e.g. magnetite) and all components contribute to the total AMS.

### 3.3.4. AMS modelling

Anisotropic physical properties of multiphase aggregates, e.g. magnetic or seismic anisotropy, can be modeled based on texture data and single crystal properties (Mainprice et al., 2011; Mainprice and Humbert, 1994). Two types of models have been computed for the present study: (1) calculating the separate contributions of each mineral, i.e. mica, chlorite, quartz, calcite and dolomite, to the specimens' magnetic anisotropies, and (2) computing the bulk anisotropy as a superposition of each individual mineral contribution weighted by their modal composition. Single crystal tensors were determined from published data for muscovite and chlorite (Ballet and Coey, 1982; Biedermann et al., 2014; Martin-Hernandez and Hirt, 2003), quartz (Voigt and Kinoshita, 1907), and calcite and dolomite (Schmidt et al., 2007, 2006). Because the specimens used in this study contain little iron, we used the single crystal properties for calcite and dolomite with low iron content (Schmidt et al., 2007, 2006). The contribution of each mineral was determined separately using Hill averages, which often give accurate results for modelled elastic properties (Hill, 1952). For the second type of model, Voigt averages were used because the mean susceptibilities of all contributing minerals vary over several orders of magnitude (Voigt, 1928). All models were computed in the MATLAB toolbox MTEX (Hielscher and Schaeben, 2008; Mainprice et al., 2011).

## 3.4. Results

### 3.4.1. Sample composition

The quantitative composition of the crystalline part of the sample is calculated from the Rietveld refinement of the synchrotron analyses (Figure 3.2). The majority of the samples is composed of ~30-50 wt-% illite/muscovite, ~25-40 wt.-% quartz, ~10-25 wt.-% chlorite and in some samples a few percent of pyrite or calcite. Sample 3890 (Cashaqua formation), however, is an exception with a higher quartz content (~60 wt.-%) and lower chlorite content (~4 wt.-%). Sample 3967 from Geneseo formation consists of about ~40 wt.-% quartz, ~30 wt.-% illite/muscovite, ~20 wt.-% chlorite and ~8 wt.-% calcite. Sample 3977 from Tully limestone has a very different composition with about 74 wt.-% calcite, ~9 wt.-% quartz, ~8 wt.-% muscovite, no chlorite and additionally 9 wt.-% dolomite. Samples 4020 and 4103, although shales, contain 4 to 12 wt.-% calcite.

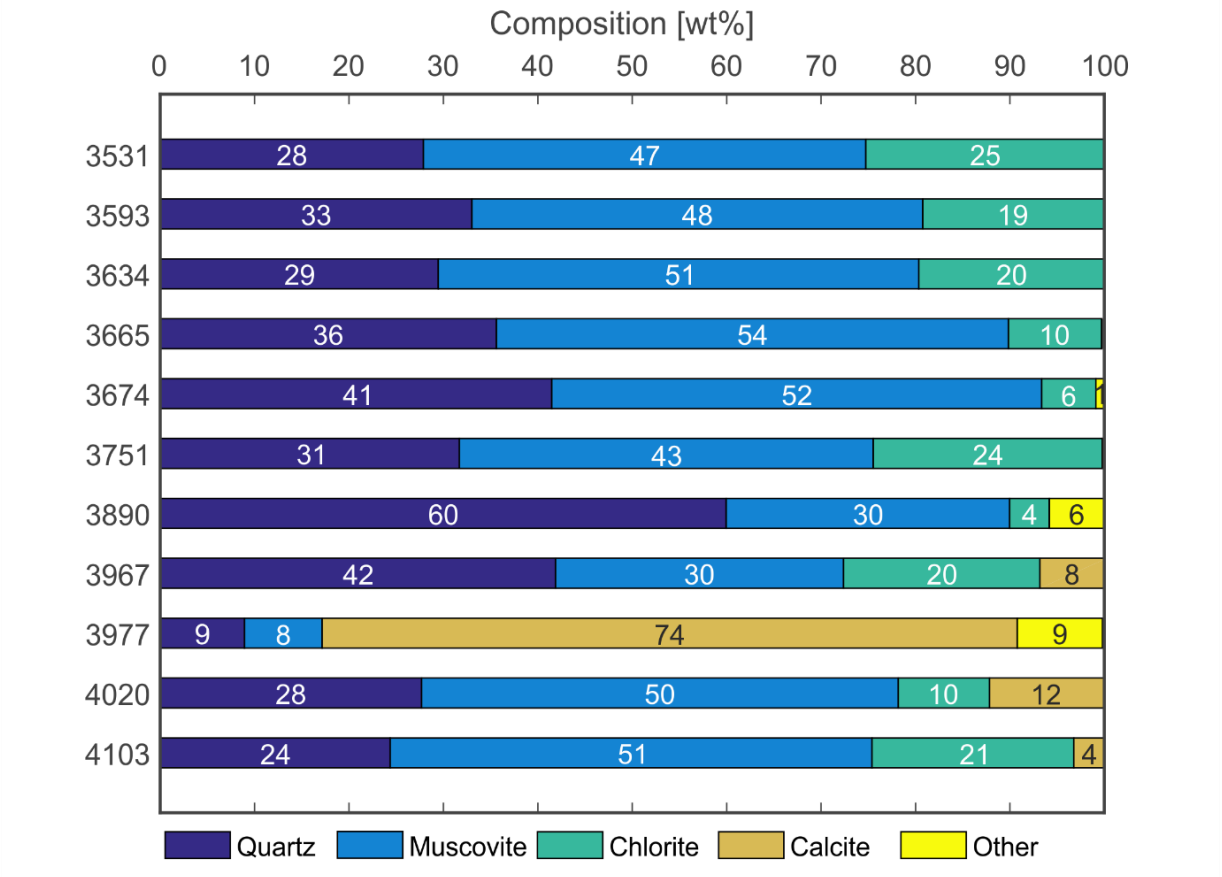


*Figure 3.2. Sample composition from Rietveld Refinement with the main components quartz, illite/muscovite, chlorite and calcite. 'Other' minerals include pyrite and dolomite.*

### 3.4.2. Microstructure

SEM microstructure analysis shows that the foliation in the samples arises mainly from aligned phyllosilicates (Figure 3.3a). Mica and chlorite can be well distinguished by their different atomic mass due to inherited Fe in chlorite. No difference can be observed in grain size or orientation of the two types of phyllosilicates. They show a mean length of 10 µm, but can reach lengths up to 40 µm. Larger phyllosilicate grains can be bent, kinked or fanned out. Mica shows a tendency to build thicker stacks than chlorite. Sometimes there are stacks of mica with chlorite. Detritic quartz grains with a mean grain size of 10 to 20 µm have irregular grain boundaries, often surrounded by organic material. Pyrite is present in all samples and can appear in a spherical shape or as idiomorphic cubes as well as framboidal aggregates. Voids appear to be filled by organic material leaving no open pore space. The filled voids appear as layer parallel oriented lenses, or as local accumulations (Figure 3.3b).

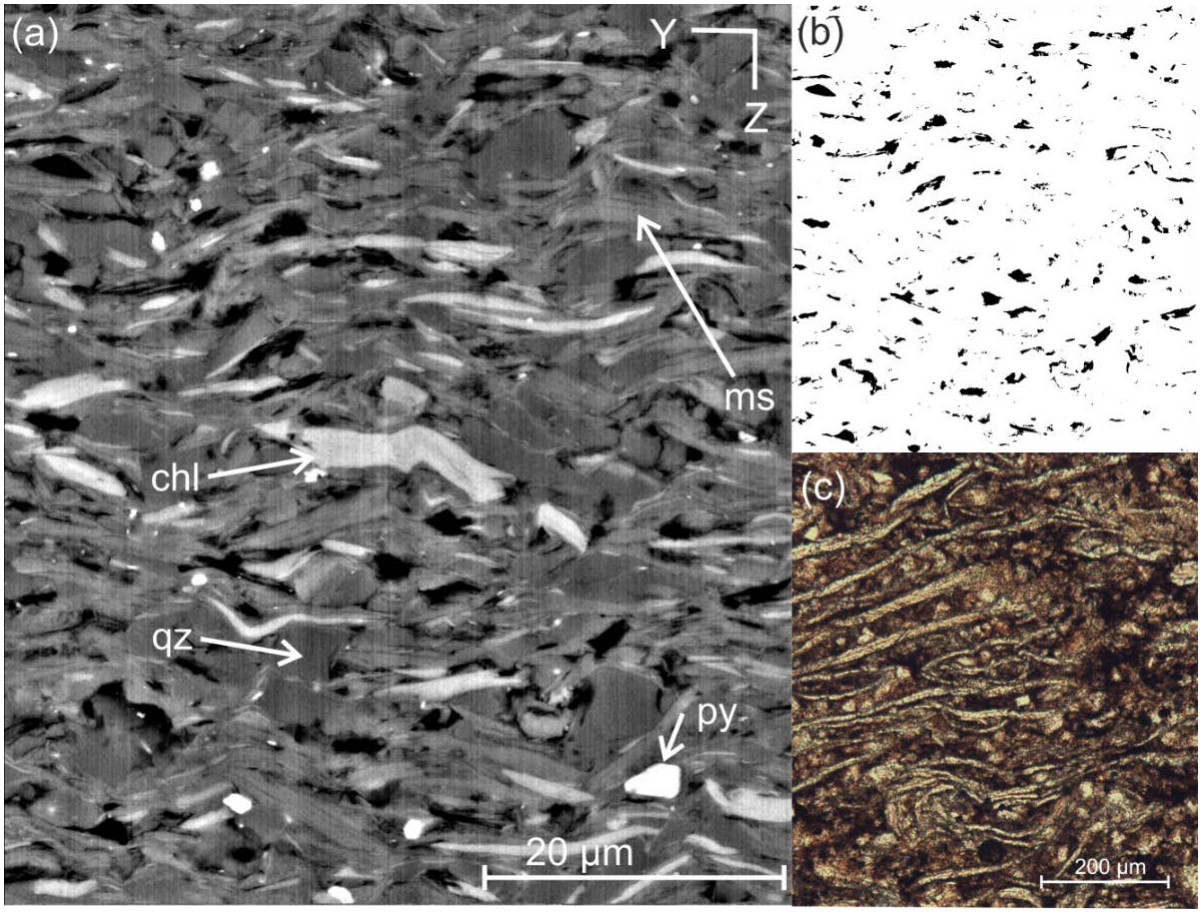


*Figure 3.3. Typical microstructures of the Appalachian Plateau black shales. (a) BSE image of sample 3751 showing the incorporated phases quartz (qz), illite/muscovite (ms), chlorite (chl) and pyrite (py). Phyllosilicates show a parallel orientation building the foliation. (b) same image as a), showing only the voids filled with organic material (c) Polarized microscopy image of sample 3967 showing aligned calcitic shells and fossil fragments of* Styliolina s.l..

Many calcitic shells and microfossils can be observed in sample 3967 (Figure 3.3c), which are mainly *Styliolina* (*s.l.*) as described for the Geneseo formation by Wilson and Schieber (2015*)*. Shells and microfossils are aligned layer parallel with their flat shape but not parallel to each other. Some of the fossils preserve their original shape, while others are broken due to compaction. Foliation is not as strongly developed as in non-fossil-bearing lithologies. Sample 3977 from the Tully limestone is composed mainly from calcitic grains, with some dolomite grains exhibiting zonation to lower Mg-contents towards the margin. Phyllosilicates are very rare in this sample and a foliation is not developed.

### 3.4.3. Texture analysis

Results of the texture analysis are displayed as pole figures in Figure 3.4. Quartz (001) pole figures show either weak texture (< 2 mrd) or are dominated by irregular reflections, caused by e.g. single crystal diffractions or other minor phases. Illite/muscovite (001) pole figures represent a strong single maximum in most samples with an intensity of up to ~22 mrd in sample 3634 from the Angola formation. The maximum is located in the center of the pole figure i.e. perpendicular to the foliation. In most of the samples a slight elongation of the (001) maxima can be observed in NW-SE orientation. The samples from the Geneseo formation (3967) and Tully limestone (3977) show only very weak maxima (1.89 and 1.97 mrd), which are not properly developed. The (010) maxima always lie at the margin of the pole figure i.e. within the foliation. In some samples they are distributed within a homogeneous girdle, and in some samples they show distinct sub-maxima within the girdle. Chlorite pole figures are comparable to the illite/muscovite pole figures, sometimes with less intense maxima and sometimes with more pronounced maxima. The NW-SE elongation of the chlorite (001) maximum is less pronounced, compared to muscovite. The (010) maxima at the margin of the pole figures mostly show a stronger separation in two distinct maxima than the illite/muscovite (010) axis pole figures. Exceptions are sample 3890 from the Cashaqua formation, where only one elongated maximum appears and sample 3967 from the Geneseo formation, which shows two distinct maxima but rotated by ca. 10° from the margin towards the center of the pole figure reflecting an inclination of the bedding which is also macroscopically visible in the sample cylinder. Calcite can show a strong texture (up to 9.93 mrd) as in samples 3967, 4020 and 4103 from the Geneseo and Mahantago formations or a very weak texture as in 3977 (1.3 mrd) from the Tully limestone. Samples 4020 and 4103, have only one (001) maximum in the center of the pole figure and additional maxima at the margin. The complex pole figures for calcite may represent microfossils, as observed in SEM microscopy that are aligned parallel to the foliation. In sample 3977 calcite mostly appears as granular components, which show no crystallographic preferred orientation.

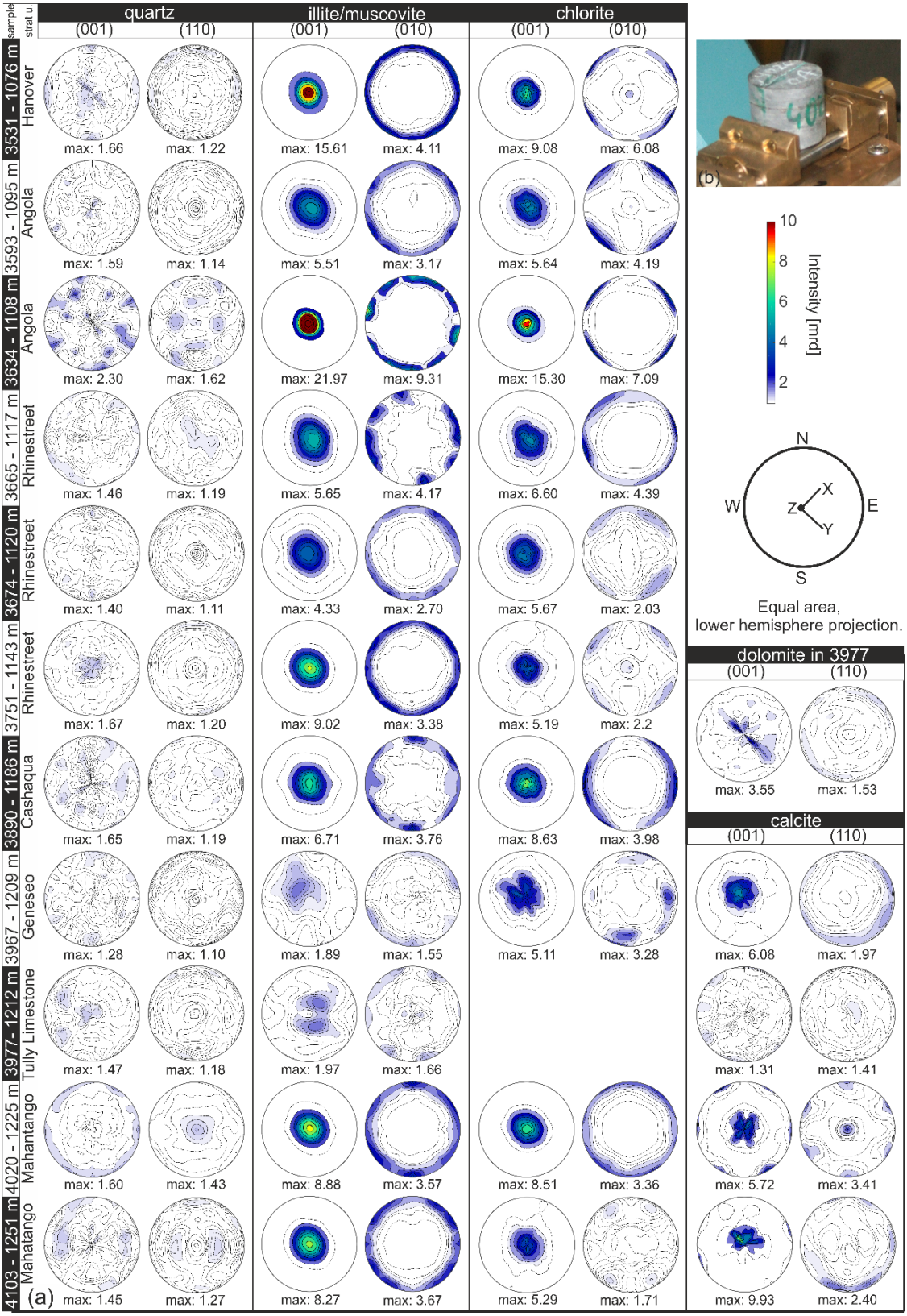


*Figure 3.4. a) Recalculated pole figures for the main mineral phases. Equal area, lower hemisphere projection. Maxima in mrd (multiples of random distribution). Quartz shows no crystallographic preferred orientation. Most samples show a strong alignment of the phyllosilicates perpendicular to the core axis reflecting the compaction, except 3967 and 3977. Calcite and dolomite, are only found in 3 samples, and texture arises most likely due to aligned fossil fragments and shells. b) Sample shape and mounting during synchrotron diffraction measurements. The dot in the orientation overview marks the orientation of the core axis and the normal to the foliation, which are parallel.*

### 3.4.4. Magnetic fabric and anisotropy

Low-field AMS was measured on all samples and is shown in Figure 3.5 and App. A2: Suppl. Table 1. The mean magnetic susceptibility in low-field varies over 2 orders of magnitude from 1.0*10^-5 to 8.0*10^-4 (SI). The mean deviatoric susceptibility, expressed as k', ranges from ~2.0*10^-7 (SI) to 2.6*10^-5 (SI), which corresponds to 0.3% to 7.2% of the mean susceptibility (Figure 3.5a). It is higher in the upper third of the core above 3760, although lower k' is found in samples 3583, 3593, 3665, 3674 and 3685. There is a drop in k' below 3760, in which k' remains below 1.5*10^-5 (SI). The Tully limestone (samples 3977) and Onondaga limestone (samples 4125) have the lowest k'.

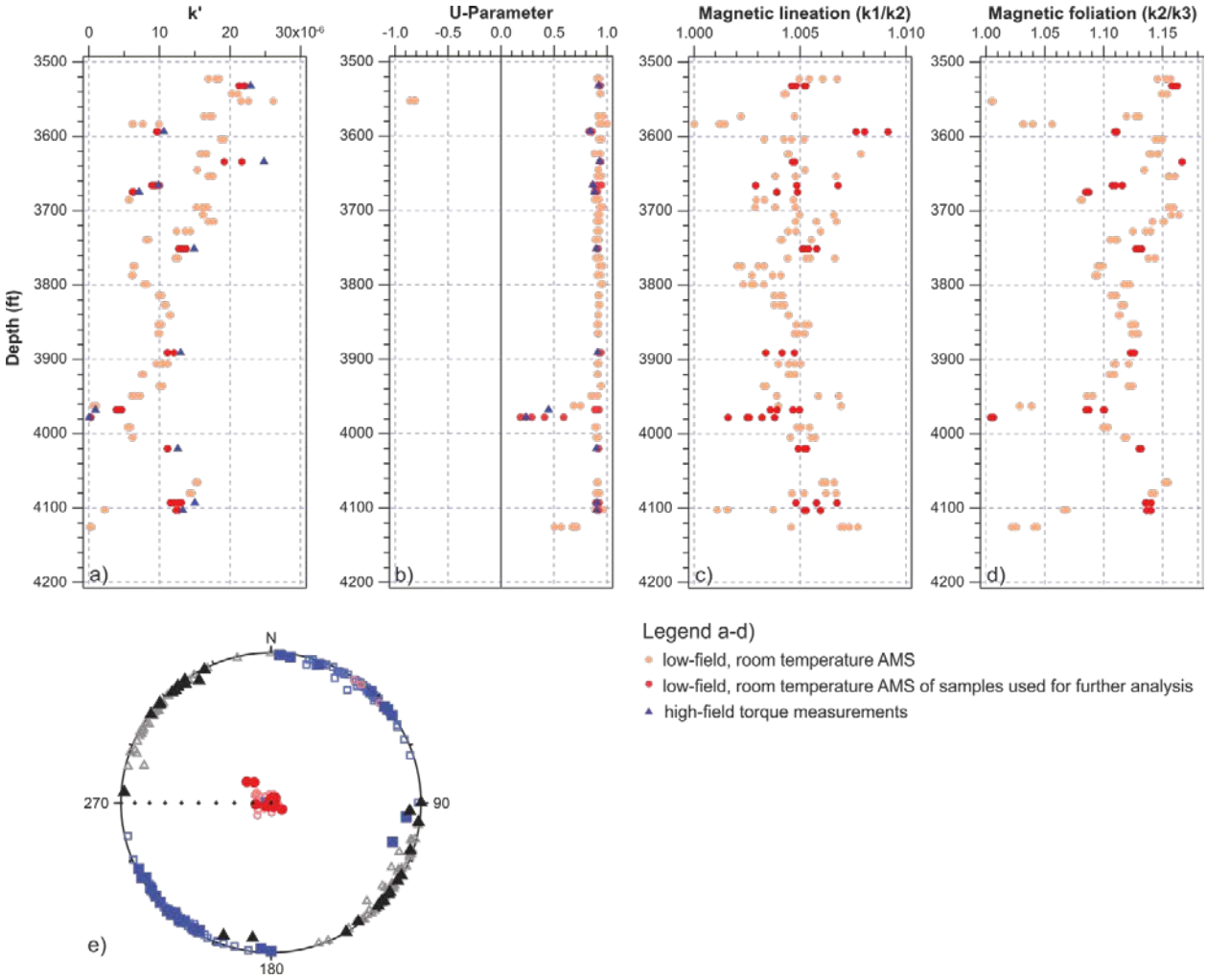


*Figure 3.5. Measured magnetic fabric in core PA5. a) mean deviatoric susceptibility k', b) shape of the susceptibility ellipsoid U, c) magnetic lineation, d) magnetic foliation, and e) orientation of the principal directions; k1 (squares), k2 (triangles), and k3 (circles) that are plotted on an equal-area, lower hemisphere stereonet. Filled symbols indicate samples with texture measurements. Symbols for the AMS axes are used in subsequent figures.*

The shape of the ellipsoid is described by the shape parameter U which is positive for the majority of the samples reflecting an oblate magnetic fabric (Figure 3.5b). Most of the oblate

samples are strongly oblate with U ranging from 0.8 -1.0. Exceptions are the samples from the calcite containing formations 3962, 3967, 3977 and 4125 (U=0.2-0.8). The only prolate sample is 3552 from the Pipe Creek formation with U = -0.8. The magnetic lineation is very weak and is in a range from 1.000 (sample 3583) to 1.009 (sample 3593) (Figure 3.5c). The magnetic foliation, can be very weak, 1.004 (sample 3977) to 1.16 (sample 3634) (Figure 3.5d). For most samples it is greater than 8%.

The principal axes of the AMS ellipsoids show that k3 is well-grouped and sub-parallel to the foliation normal (Figure 3.5e). Only the prolate samples have k1 subparallel to the foliation normal and k3 in foliation. The magnetic susceptibilities for k1 and k2 show only very small differences, as has been seen from the weak degree of lineation. In spite of this weak lineation, the orientation of k1 lies NE-SW for most samples and k2 NW-SE (Figure 3.5e). Only two samples from 3967, which have a prolate shape, show an interchange between the direction of k1 and k2.

High-field torque measurements were conducted on the 11 samples that were used for texture analysis. Only the paramagnetic AMS is significant in all the samples, i.e., the ferrimagnetic component is isotropic. Both k' and U of the high-field AMS have similar values as the low-field AMS, which indicates that paramagnetic minerals control the low-field AMS (blue triangles in Figure 3.5a, b; App. A2: Suppl. Table 2). The directions of the principal axes are also similar in all samples except for the sample from the Tully limestone in which k2 and k3 are interchanged for the dia/ paramagnetic susceptibility (Figure 3.5e).

### 3.4.5. AMS modelling

Figure 3.6 shows an example of how the AMS can be modeled from the different minerals that contribute to the bulk rock AMS. The final bulk rock models for all samples are displayed in Figure 3.7. An overview of all modeled mineral contributions can be found in App. A2: Suppl. Figure 1 & Suppl. Table 3. The contributions from the two phyllosilicates, illite/ muscovite and chlorite are generally coaxial. The orientation of phyllosilicate magnetic fabric is mainly defined by the direction of the minimum susceptibility axes. The intrinsic AMS of these minerals is uniaxial with the unique axis parallel to (001). Because the orientation of the principal axes of the AMS due to illite/muscovite and chlorite are similar, their magnetic fabrics are additive. Quartz, calcite and dolomite can affect the bulk susceptibility strongly but have less of an effect on the principal directions. It is interesting to note that when the magnetic fabric of calcite is coaxial to the muscovite fabric, the quartz fabric is opposite (cf., App. A2: Suppl. Fig. 1; 3967, 4103), and *vice versa* (App. A2: Suppl. Fig. 1; 3977).

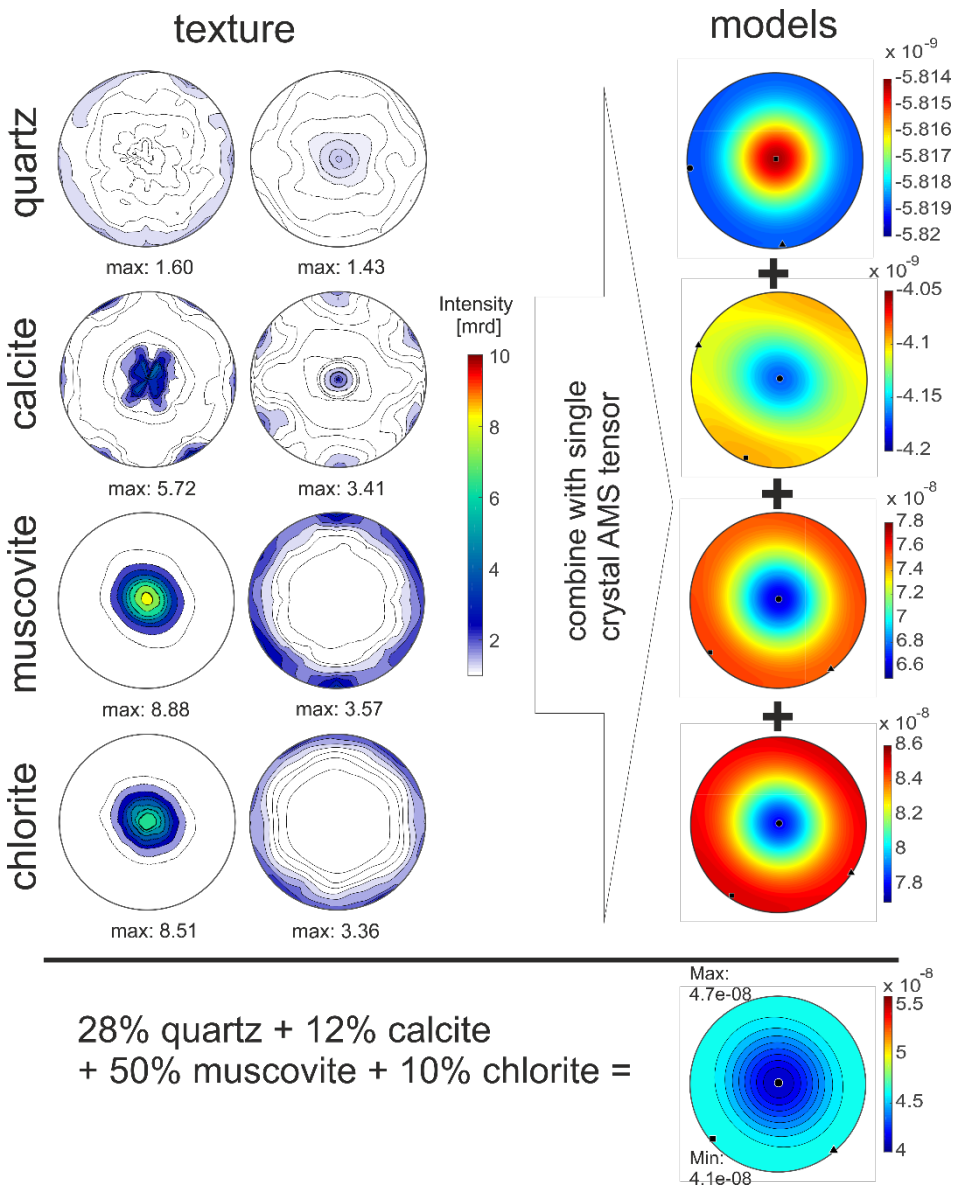


*Figure 3.6. Modelling path for calculating the AMS as demonstrated for sample 4020. The texture of each incorporated mineral and single crystal AMS tensors, are first used to obtain the single phase model, and then combined by applying their modal contribution to the rock. Orientation is the same as in Fig. 4.*

The principal anisotropy directions of the combined models strongly reflect the magnetic fabric contribution of the phyllosilicates (Figure 3.7). Quartz and calcite, even when they dominate the bulk composition, do not appear to affect the orientation of principal axes. They do, however, change the modeled mean susceptibility. For all samples except 3977 (Tully limestone) the modeled k3 is within 10° of k3 from the low-field AMS, and within 7° from the high-field AMS. The difference between the measured and modelled k1 and k2, respectively, reflect the uniaxial nature of the phyllosilicate anisotropy.

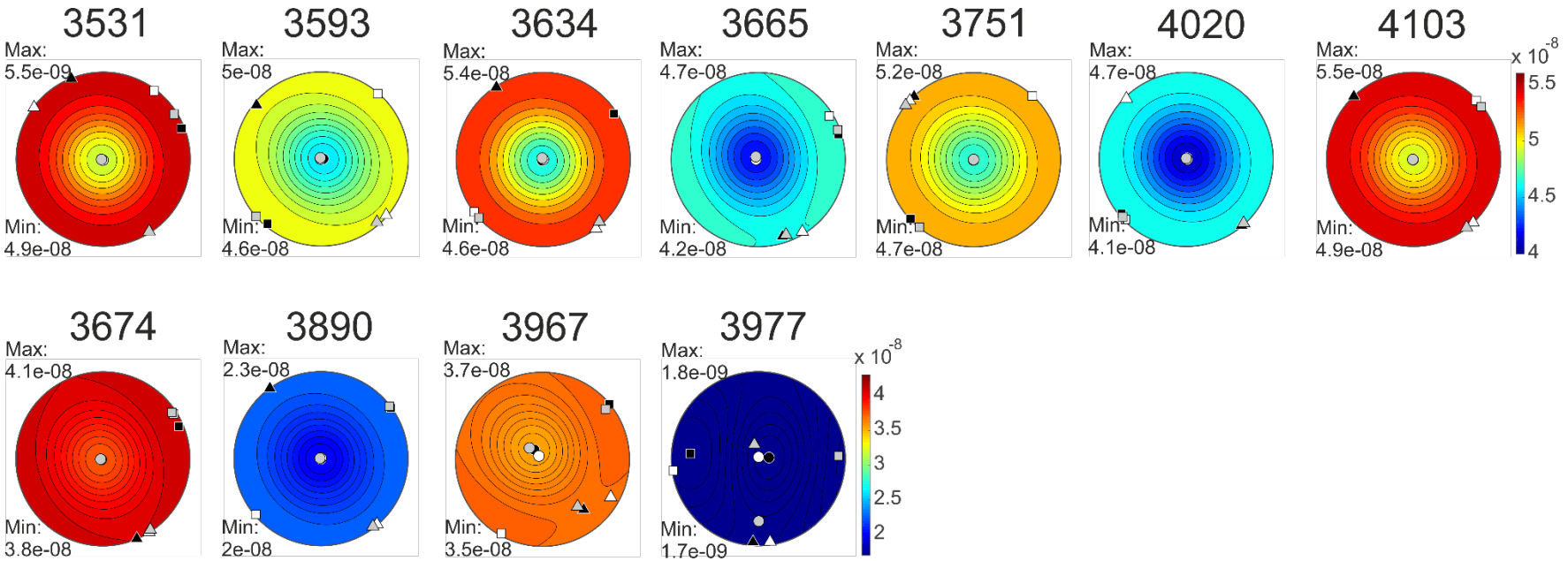


*Figure 3.7. Calculated whole rock AMS models, which mostly reflect the phyllosilicate texture, showing the principal axis of the modeled AMS (black symbols) and measured low-field (white) and high-field (grey) AMS. Data is weight normalized. Orientation is the same as in Fig. 4.*

## 3.5. Discussion

### 3.5.1. Role of mineralogy and texture on AMS

From thin section and X-ray diffraction analyses we know that samples contain both paramagnetic minerals, mainly illite/muscovite and chlorite, and diamagnetic minerals, quartz and in some samples calcite. High-field torque measurements indicate that dia-/paramagnetic minerals are responsible for the observed AMS, and the ferromagnetic phases do not contribute. The ferromagnetic minerals, however, can contribute to the bulk susceptibility. Rock magnetic studies on neighboring drill cores NY1 and NY4 indicate that pyrrhotite and magnetite could be present (Hirt et al., 1995).

We have found a good agreement between the measured and modeled AMS. The agreement of the modeled AMS with the separated dia-/paramagnetic component is slightly better than with the low-field AMS. This difference may be related to any ferromagnetic minerals. It is also clear from the models that the phyllosilicate minerals control the magnetic fabric, even in rocks that have a large quartz and/or calcite content. Compared to the earlier work of Evans et al. (1989b) and Hirt et al. (1995) we demonstrate that illite/muscovite also contributes to the observed AMS. Our results prove the interpretations of other studies that suggested phyllosilicates as the carrier of AMS (Borradaile et al., 1993; Hirt et al., 1995; Hounslow, 1985; Rochette and Vialon, 1984; Schulmann and Jecek, 2011; Zak et al., 2008).

The intrinsic anisotropy of phyllosilicates in combination with the strong texture results in a strongly oblate magnetic fabric with flattening in the foliation plane. There is a weak magnetic lineation that leads k1 to lie NE-SW along the trend of the Allegheny front to the E. This lineation reflects the slight ellipsoidal shape of the phyllosilicates' (001) pole figure maxima, which is in the direction NW-SE. This can be related to the bending and kinking that is observed in thin section (cf. Figure 3.3). Sample 3977, the Tully limestone sample, has a less oblate shape, but its principal directions are still dominated by illite/muscovite.

Shape is the most difficult anisotropy parameter to model (Borradaile and Jackson, 2010). This may be related to small errors/noise either in the texture or anisotropy measurements, and is consistent with Biedermann et al., (2013), who showed that principal directions are least, and anisotropy shape most affected by noise in the data. In our samples there is a fairly good agreement between the modeled and measured U-parameter (Figure 3.8a), where the difference could easily be related to measurement noise.

Models underestimate the measured k' by a factor of 1.6 to 3.6 (2.2 on average) (Figure 3.8b). This is most likely linked to the chemical composition, especially the Fe content, of the single crystal tensors used compared to the composition of the minerals in the samples. Because there is a linear relationship between k' and Fe content (Biedermann et al., 2014; Schmidt et

al., 2006), the observed factor of 2.2 indicates possible difference in Fe concentration of a factor of 2.2. Better results could be obtained by extracting a single tensor from the rock to be modeled, and using that tensor rather than a tensor from the literature.

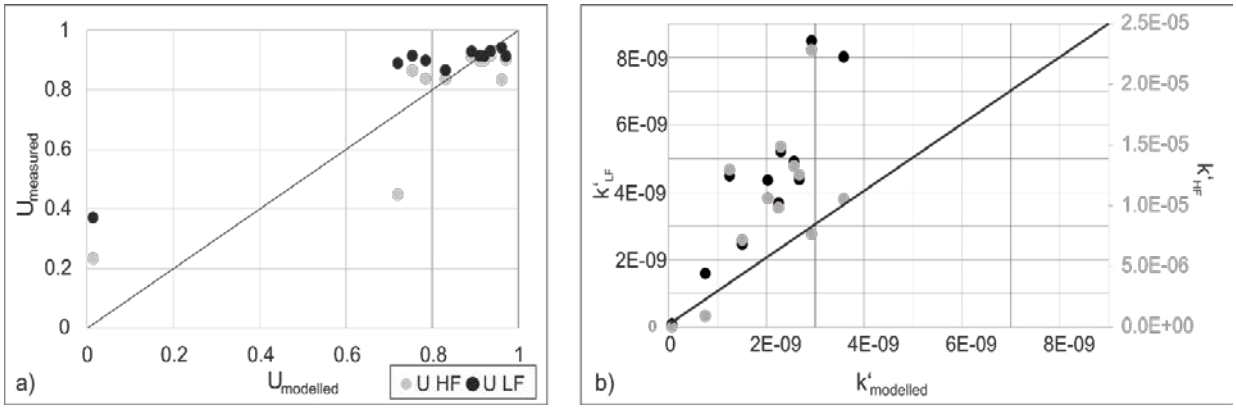


*Figure 3.8. Comparison of a) U, and b) k' for measured and modeled AMS. $K'_{HF}$ is plotted on a second axis as values differ strongly from LF and modeled values.*

For texture analysis we use crystallographic and chemical data from the literature which might be different to the minerals in our samples. Resulting deviations can introduce little errors into the texture data from which error propagation to the AMS calculations can result. Possible sample composition heterogeneities can also introduce an error. Such an error could be minimized by measuring additional sample cylinder slices for the texture analysis.

### 3.5.2. Micro- and magnetic fabric development

The micro- and magnetic fabric development observed in our samples reflect dominant flattening strain and slight NW-SE directed compression. Sedimentation represents mostly the basin facies of the Catskill Delta complex (Ettensohn, 1985b). The sedimentation and compaction processes most likely only lead to a fabric showing a flattening component and did not develop any lineation (Figure 3.9a). Deltaic currents or other synsedimentary processes could possibly invoke a lineation during sedimentation, but as the sedimentary facies changed progressively as recorded by the differing lithologies, the sediment succession experienced several cycles of progression (Ettensohn, 1985b). It seems to be very unlikely that during the different stages the flow direction was constant over time. During burial the induced rigid body rotation can be expected to show a circular maximum in the phyllosilicates (001) pole figure and k1=k2 in the magnetic anisotropy tensor. The slight ellipsoidal appearance of the maxima and appropriate magnetic lineation can be explained by a later compressional deformation. A weak directional compression component could be able just to kink the phyllosilicates (Figure 3.9b). Since the kinking is related to a kink or fold axis an elliptical (00l)-texture-maximum

follows. The slightly inclined basal planes do not fully contribute to the magnetic horizontal NW-SE component, which leads to a slightly lower k2 compared to k1. An elliptical distribution of the (00l) axes of the phyllosilicate phases can lead to a magnetic lineation (Martin-Hernandez et al., 2005). As the chlorite also shows elliptic (00l) maxima, even though they are less pronounced, this indicates that the deformation happened during a later stage of rock history, not during sedimentation.

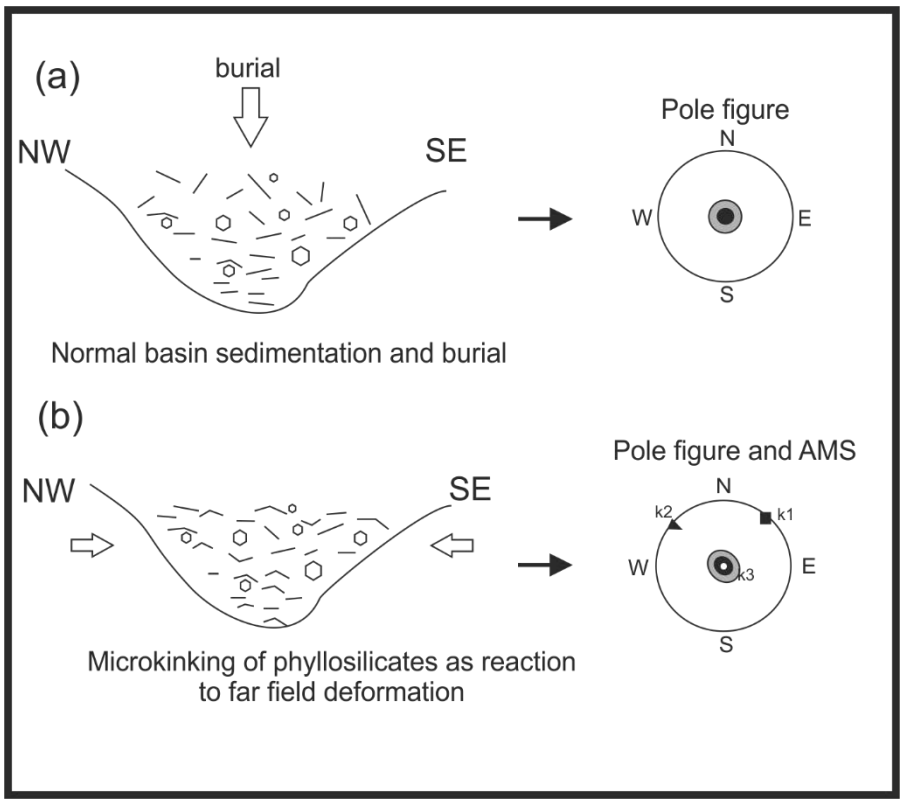


*Figure 3.9. Model for the influence of the Allegheny orogeny on microfabric and resulting asymmetry of pole figure maxima and resulting AMS ellipsoid a) sediment exposed only to flattening strain by burial and b) resulting micro- and magnetic fabric due to tectonic influence of the Allegheny orogeny.*

### 3.5.3. Regional geologic implications

The preferential alignment of phyllosilicates reflects the dominant flattening strain due to burial compaction. The phyllosilicate minerals control the magnetic anisotropy in all samples, including samples in which calcite is the main constituent. As chlorite is commonly assumed to be a secondary mineral phase in sedimentary rocks, its orientation parallel to the primary muscovite/illite platelets emphasizes the burial dominated rock history. Evans et al. (1989b) determined the magnitude of horizontal stress in wells on the Appalachian Plateau in New York state NY1 and NY4. They also estimated the degree of compaction from chlorite texture, which was determined by X-ray goniometry of chlorite. They showed that the degree of compaction

increases with depth until there is a drop at the base of Rhinestreet formation, and this is also seen by a decrease in stress. The authors explain the sudden drop to paleo-overpressure in the lower Rhinestreet formation. Hirt et al. (1995) demonstrated a similar drop in degree of anisotropy at this level. In our study, variations in k' and degree of foliation are strongly dependent on mineralogy. It should be noted, however, that there is a general decrease in k' in the lower part of the Rhinestreet formation (Figure 5). The difference is not large, but is on the same order of what was found for the AMS in cores NY1 and NY4. There is a slight increase of bulk susceptibility with depth which cannot be seen in the observed textures, but the intensity of the susceptibility and anisotropy is more dependent on the individual sample composition.
Samples show a very weak lineation to the NE (Figure 5e), but it is significant on the 95% confidence level for most samples and 90% confidence level for the remainder. This orientation is parallel to the fast Vp direction (Evans et al., 1989b), which is sub-parallel to the Alleghenian front line. The Devonian strata in PA5 show no major structural features, which could give insight into the timing of LPS. The elliptic (001)-texture maxima caused by microfolding and the weak magnetic lineation with a direction to the NE-SW are consistent with northwesterly directed LPS. Although the drill site lies approximately 200 km from the Allegheny Front, the Devonian strata have undergone a small amount of LPS that is detected by the ellipsoid maxima shape in the pole figures and the weak magnetic lineation.

## 3.6. Conclusion

This study demonstrates that the analysis of texture and microstructure in combination with texture derived AMS-modeling is a crucial approach to the understanding of the AMS formation. Modeling the AMS from quantitative texture analysis can explain how individual mineral fabrics contribute to the whole rock AMS. We can clearly show that the bulk susceptibility is composed of all of the dia- and paramagnetic minerals composing the samples, while the anisotropic component is only carried by the paramagnetic phyllosilicates. The magnetic lineation, even though it is weak, is defined by microscale kinking and folding of the phyllosilicates as microstructure impressively demonstrates. This underlines the dominance of phyllosilicates in defining the magnetic fabric. Consequently, the phyllosilicates are able to record the layer-parallel shortening of the black shales of Appalachian Plateau, even if it is only a very weak shortening, by the folding and kinking. Since we could establish the correlation between the ellipticity of the (001)-maxima and the magnetic lineation, for these rocks and this tectonic setting, the AMS can now be employed to routinely measure large sample series in a quick and cost-effective way to upscale the results to a regional scale.

## Acknowledgements

We gratefully acknowledge beam time granted at synchrotron facilities DESY Grant I-20140240 and ESRF Grant ES-611as well as the help of the beamline scientists. We further thank Kirsten Techmer for support during SEM analysis and Helga Groos-Uffenorde for kind help in fossil identification. We are grateful to Bjarne Almqvist, Ken Kodama and Manish A. Mamtani for their detailed reviews which greatly improved the manuscript. RK received funding by the GeoGenderChancen Fonds granted by the Faculty of Geoscience and Geography Göttingen. ARB was supported by Swiss National Science Foundation projects 167608 and 167609. Experimental data can be accessed under DOI 10.5281/zenodo.1462566.

## References

Antao, M., Hassan, I., Wang, J., Lee, P.L., Toby, B.H., 2008. State-of-the-art high-resolution powder X-ray diffraction (HRPXRD) illustrated with Rietveld structure refinement of quartz, sodalite, tremolite, and meionite. Can. Mineral. 46, 1501–1509. doi:10.3749/canmin.46.5.1501

Ballet, O., Coey, J.M.D., 1982. Magnetic properties of sheet silicates; 2:1 layer minerals. Phys. Chem. Miner. 8, 218–229. doi:10.1007/BF00309481

Balsley, J.R., Buddington, A.F., 1960. Magnetic susceptibility anisotropy and fabric of some Adirondack granites and orthogneisses. Am. J. Sci. 258, 6–20.

Bergmüller, F., Bärlocher, C., Geyer, B., Grieder, M., Heller, F., Zweifel, P., 1994. A torque magnetometer for measurements of the high-field anisotropy of rocks and crystals. Meas. Sci. Technol. 5, 1466–1470.

Biedermann, A.R., Bender, C., Lorenz, W.E.A., Hirt, A.M., 2014. Low-temperature magnetic anisotropy in micas and chlorite. Tectonophysics 629, 63–74. doi:10.1016/j.tecto.2014.01.015

Biedermann, A.R., Kunze, K., Hirt, A.M., 2018. Interpreting magnetic fabrics in amphibole-bearing rocks. Tectonophysics 722, 566–576. doi:10.1016/j.tecto.2017.11.033

Biedermann, A.R., Kunze, K., Zappone, A., Hirt, A.M., 2015. Origin of magnetic fabrics in ultramafic rocks, in: 17th International Conference on Textures of Materials (ICOTOM 17). IOP Conf. Series: Materials Science and Engineering, pp. 1–4. doi:10.1088/1757-899X/82/1/012098

Biedermann, A.R., Lowrie, W., Hirt, A.M., 2013. A method for improving the measurement of low-field magnetic susceptibility anisotropy in weak samples. Appl. Geophys. 88, 122–130. doi:10.1016/j.jappgeo.2012.10.008

Borradaile, G.J., Henry, B., 1997. Tectonic applications of magnetic susceptibility and its anisotropy. Earth Sci. Rev. 42, 49–93. doi:10.1016/S0012-8252(96)00044-X

Borradaile, G.J., Jackson, M., 2004. Anisotropy of the magnetic susceptibility (AMS): magnetic petrofabrics of deformed rocks. Geol. Soc. Spec. Pub. 238, 299-360. doi:10.1144/GSL.SP.2004.238.01.18

Borradaile, G.J., Stewart, R.A., Werner, T., 1993. Archean uplift of a subprovince boundary in the Canadian Shield, revealed by magnetic fabrics. Tectonophysics 227, 1–15. doi:10.1016/0040-1951(93)90083-V

Bunge, H.J., 1986. General Outline and Series Expansion Method, in: Bunge, H.J., Esling, C. (Eds.), Quantitative Texture Analysis. DGM Informationsgesellschaft, Oberursel, pp. 1–72.

Cifelli, F., Mattei, M., Chadima, M., Hirt, A.M., Hansen, A., 2005. The origin of tectonic lineation in extensional basins: Combined neutron texture and magnetic analyses on “undeformed” clays. Earth Planet. Sci. Lett. 235, 62–78. doi:10.1016/j.epsl.2005.02.042

Cliffs Minerals Inc, 1982. Analysis of the Devonian shales in the Appalachian basin. Final report to U.S. Dept. of Energy under contract DE-C21-80MC14693, vols. 1 and 2. Morgantown, West Virginia.

Downs, R.T., Hall-Wallace, M., 2003. The American Mineralogist crystal structure database. Am. Mineral. 88, 247–250.

Engelder, T., Engelder, R., 1977. Fossil distortion and décollement tectonics of the Appalachian Plateau. Geology 5, 457–460. doi:10.1130/0091-7613(1977)5<457:FDADTO>2.0.CO;2

Ettensohn, F.R., 1985a. The Catskill delta complex and the Acadian orogeny: A model. Geol. Soc. Am. Spec. Pap. 201, 39–49.

Ettensohn, F.R., 1985b. Controls on development of Catskill Delta complex basin-facies. Geol. Soc. Am. Spec. Pap. 201, 65–77.

Evans, K.F., 1989. Appalachian Stress Study 3. Regional scale stress variations and their relation to structure and contemporary tectonics. J. Geophys. Res. Solid Earth 94, 17619–17645. doi:10.1029/JB094iB12p17619

Evans, K.F., Engelder, T., Plumb, R.A., 1989a. Appalachian stress study 1. A Detailed Description of In Situ Stress Variations in Devonian Shales of the Appalachian Plateau. J. Geophys. Res. 94, 7129–7154. doi:10.1029/JB094iB06p07129

Evans, K.F., Oertel, G., Engelder, T., 1989b. Appalachian stress study 2. Analysis of Devonian shale core: Some implications for the nature of contemporary stress variations and alleghanian deformation in Devonian rocks. J. Geophys. Res. 94, 7155–7170. doi:10.1029/JB094iB06p07155

Faill, R.T., 1997a. A geologic history of the north-central Appalachians. Part 1. Orogenesis from the Mesoproterozoic through the Taconic orogeny. Am. J. Sci. 297, 551–619.

doi:10.2475/ajs.297.6.551

Faill, R.T., 1997b. A geologic history of the north-central Appalachians; Part 2; The Appalachian Basin from the Silurian through the Carboniferous. Am. J. Sci. 297, 729–761. doi:10.2475/ajs.297.7.729

Fuller, M.D., 1960. Anisotropy of Susceptibility and the Natural Remanent Magnetization of Some Welsh Slates. Nature 186, 791–792. doi:10.1038/186791a0

Graf, D.L., 1961. Crystallographic tables for the rhombohedral carbonates. Am. Mineral. 46, 1283–1316.

Graham, J.W., 1966. Significance of Magnetic Anisotropy in Appalachian Sedimentary Rocks. In: Steinhard, I.S. and Smith. T.I. (Eds). The Earth beneath the Continents. Geophys. Monogr., Am. Geophys. Union, 10: 627-648.

Graham, J.W., 1954. Magnetic anisotropy, an unexploited petrofabric element. Geol. Soc. Am. Bull. 65, 1257–1258.

Gray, M.B., Stamatakos, J., 1997. New model for evolution of fold and thrust belt curvature based on integrated structural and paleomagnetic results from the Pennsylvania salient. Geology 25, 1067–1070. doi:10.1130/0091-7613(1997)025<1067:NMFEOF>2.3.CO;2

Grazulis, S., Chateigner, D., Downs, R.T., Yokochi, A.F.T., Quirós, M., Lutterotti, L., Manakova, E., Butkus, J., Moeck, P., Le Bail, A., 2009. Crystallography Open Database - An open-access collection of crystal structures. J. Appl. Crystallogr. 42, 726–729. doi:10.1107/S0021889809016690

Haerinck, T., Wenk, H., Debacker, T.N., Sintubin, M., 2015. Preferred mineral orientation of a chloritoid-bearing slate in relation to its magnetic fabric. J. Struct. Geol. 71, 125–135. doi:10.1016/j.jsg.2014.09.013

Hammersley, A.P., 1998. FIT2D V9.129 Reference Manual V3.1. Inter Rep ESRF98HA01. Grenoble.

Hielscher, R., Schaeben, H., 2008. A novel pole figure inversion method: specification of the MTEX algorithm. J. Appl. Crystallogr. 41, 1024–1037. doi:10.1107/S0021889808030112

Hill, R., 1952. The elastic behaviour of a crystalline aggregate. Proc. Phys. Soc. A 65, 349–354.

Hirt, A.M., Almqvist, B.S.G., 2011. Unraveling magnetic fabrics. Int. J. Earth Sci. 101, 613–624. doi:10.1007/s00531-011-0664-0

Hirt, A. M., Lowrie, W., Luneburg, C., Lebit, H., Engelder, T., 2004. Magnetic and mineral fabric development in the Ordovician Martinsburg Formation in the Central Appalachian Fold and Thrust Belt, Pennsylvania. Geol. Soc. London, Spec. Publ. 238, 109–126. doi:10.1144/GSL.SP.2004.238.01.09

Hirt, A.M., Evans, F., Engelder, T., 1995. Correlation between magnetic anisotropy and fabric

for Devonian shales on the Appalachian Plateau 247, 121–132. doi:10.1016/0040-1951(94)00176-A

Hounslow, M.W., 1985. Magnetic fabric arising from paramagnetic phyllosilicate minerals in mudrocks. J. Geol. Soc. London. 142, 995–1006. doi:10.1144/gsjgs.142.6.0995

Hrouda, F., 1982. Magnetic anisotropy of rocks and its application in geology and geophysics. Geophys. Surv. 5, 37–82. doi:10.1007/BF01450244

Jelinek, V., 1981. Characterization of the magnetic fabric of rocks. Tectonophysics 79, T63–T67. doi:10.1016/0040-1951(81)90110-4

Jelinek, V.I.T., 1984. On a mixed quadratic invariant of the magnetic susceptbility tensor. J. Geophys. 56, 58–60.

Kanitpanyacharoen, W., Kets, F.B., Wenk, H.R., Wirth, R., 2012. Mineral preferred orientation and microstructure in the Posidonia Shale in relation to different degrees of thermal maturity. Clays Clay Miner. 60, 315–329. doi:10.1346/CCMN.2012.0600308

Kanitpanyacharoen, W., Wenk, H.R., Kets, F., Lehr, C., Wirth, R., 2011. Texture and anisotropy analysis of Qusaiba shales. Geophys. Prospect. 59, 536–556. doi:10.1111/j.1365-2478.2010.00942.x

Kligfield, R., Lowrie, W., Hirt, A., Siddans, A.W.B., 1983. Effect of progressive deformation on remanent magnetization of Permian redbeds from the Alpes Maritimes (France). Tectonophysics 97, 59–85. doi:10.1016/0040-1951(83)90211-1

Leiss, B., Ullemeyer, K., 1999. Texture characterization of carbonate rocks and some implications for the modeling of physical anisotropies, derived from idealized texture types. Zeitschrift der Dtsch. Geol. Gesellschaft 259–274.

Liang, J.-J., Hawthorne, F.C., 1996. Rietveld refinement of micaceous materials; muscovite-2M1, a comparison with single-crystal structure refinement. Can. Mineral. 34, 115–122.

Lüneburg, C.M., Lampert, S.A., Lebit, H.D., Hirt, A.M., Casey, M., Lowrie, W., 1999. Magnetic anisotropy, rock fabrics and finite strain in deformed sediments of SW Sardinia (Italy). Tectonophysics 307, 51–74.

Lutterotti, L., Matthies, S., Wenk, H.-R., Schultz, A.S., Richardson, J.W., 1997. Combined texture and structure analysis of deformed limestone from time-of-flight neutron diffraction spectra. J. Appl. Phys. 81, 594–600. doi:10.1063/1.364220

Lutterotti, L., Vasin, R., Wenk, H.-R., 2014. Rietveld texture analysis from synchrotron diffraction images I. Calibration and basic analysis. Powder Diffr. 29, 76–84. doi:10.1017/S0885715613001346

Lutterotti, L., Voltolini, M., Wenk, H.R., Bandyopadhyay, K., Vanorio, T., 2010. Texture analysis of a turbostratically disordered Ca-montmorillonite. Am. Mineral. 95, 98–103. doi:10.2138/am.2010.3238

Mainprice, D., Hielscher, R., Schaeben, H., 2011. Calculating anisotropic physical properties from texture data using the MTEX open source package. Geol. Soc. Spec. Pub. 360, 175-192. doi:10.1144/SP360.10

Mainprice, D., Humbert, M., 1994. Methods of calculating petrophysical properties from lattice preferred orientation data. Surv. Geophys. 15, 575–592. doi:10.1007/BF00690175

Martin-Hernandez, F., Ferre, E.C., 2007. Separation of paramagnetic and ferrimagnetic anisotropies: A review. J. Geophys. Res. 112, B03105. doi:10.1029/2006JB004340

Martin-Hernandez, F., Hirt, A.M., 2003. The anisotropy of magnetic susceptibility in biotite, muscovite and chlorite single crystals. Tectonophysics 367, 13–28. doi:10.1016/S0040-1951(03)00127-6

Martin-Hernandez, F., Hirt, A.M., 2001. Separation of ferrimagnetic and paramagnetic anisotropies using a high-field torsion magnetometer. Tectonophysics 337, 209–221. doi:10.1016/S0040-1951(01)00116-0

Martin-Hernandez, F., Kunze, K., Julivert, M., Hirt, A.M., 2005. Mathematical simulations of anisotropy of magnetic susceptibility on composite fabrics. J. Geophys. Res. 110, B06102. doi:10.1029/2004JB003505

Matthies, S., Vinel, G.W., 1982. On the Reproduction of the Orientation Distribution Function of Texturized Samples from Reduced Pole Figures Using the Conception of a Conditional Ghost Correction. Phys. status solidi 112, K111–K114. doi:10.1002/pssb.2221120254

Meglis, I., Engelder, T., 1994. The Mechanical Properties of Rock through an Ancient Transition Zone in the Appalachian Basin, in: Ortoleva, P.J. (Ed.), Basin Compartments and Seals. American Association of Petroleum Geologists.

Moores, E.M., 1991. Southwest U . S . -East Antarctic ( SWEAT ) connection : A hypothesis. Geology 19, 425–428. doi:10.1130/0091-7613(1991)019<0425:SUSEAS>2.3.CO;2

Mount, V.S., Wilkins, S., Comiskey, C.S., 2017. Characterization of the seismically imaged Tuscarora fold system and implications for layer parallel shortening in the Pennsylvania salient. J. Struct. Geol. 105, 18–33. doi:10.1016/j.jsg.2017.10.007

Omotoso, O., Mikula, R., Urquhart, S., Sulimma, H., Stephens, P., 2006. Characterization of clays from poorly processing oil sands using synchrotron techniques. Clay Sci. 12, 88–93. doi:10.1017/CBO9781107415324.004

Powell, C.M., Li, Z.X., McElhinny, M.W., 1993. Paleomagnetic constraints on timing of the Neoproterozoic breakup of Rodinia and the Cambrian formation of Gondwana. Geology 21, 889–892. doi:10.1130/0091-7613(1993)021<0889:PCOTOT>2.3.CO;2

Rankin, D., 1994. Continental margin of the eastern United States: Past and present, in: Speed, R. (Ed.), Phanerozoic Evolution of North American Continent-Ocean Transitions. Geological Society of America, Decade of North American Geology Continent-Ocean

Transect Volume, Boulder, Colorado, pp. 129–218.

Rietveld, H.M., 1969. A profile refinement method for nuclear and magnetic structures. J. Appl. Crystallogr. 2, 65–71. doi:10.1107/S0021889869006558

Rochette, P., Vialon, P., 1984. Development of planar and linear fabrics in Dauphinois shales and slates (French Alps) studied by magnetic anisotropy and its mineralogical control. J. Struct. Geol. 6, 33–38.

Schmidt, V., Günther, D., Hirt, A.M., 2006. Magnetic anisotropy of calcite at room-temperature. Tectonophysics 418, 63–73. doi:10.1016/j.tecto.2005.12.019

Schmidt, V., Hirt, A.M., Hametner, K., Günther, D., 2007. Magnetic anisotropy of carbonate minerals at room temperature and 77 K. Am. Mineral. 92, 1673–1684. doi:10.2138/am.2007.2569

Schmidt, V., Hirt, A.M., Leiss, B., Burlini, L., Walter, J.M., 2009. Quantitative correlation of texture and magnetic anisotropy of compacted calcite–muscovite aggregates. J. Struct. Geol. 31, 1062–1073. doi:10.1016/j.jsg.2008.11.012

Schulmann, K., Jecek, J., 2011. Some remarks on fabric overprints and constrictional AMS fabrics in igneous rocks. Int. J. Earth Sci. 101, 705–714.

Schumann, K., Stipp, M., Leiss, B., Behrmann, J.H., 2014. Texture development in naturally compacted and experimentally deformed silty clay sediments from the Nankai Trench and Forearc, Japan. Tectonophysics 636, 125–142. doi:10.1016/j.tecto.2014.08.005

Vasin, R.N., Wenk, H.R., Kanitpanyacharoen, W., Matthies, S., Wirth, R., 2013. Elastic anisotropy modeling of Kimmeridge shale. J. Geophys. Res. Solid Earth 118, 3931–3956. doi:10.1002/jgrb.50259

Voigt, W., 1928. Lehrbuch der Kristallphysik. Teubner Verlag, Leipzig.

Voigt, W., Kinoshita, S., 1907. Bestimmung absoluter Werte von Magnetisierungszahlen insbesondere für Kristalle. Ann. Phys. 24, 492–514.

Wenk, H.-R., Kanitpanyacharoen, W., Voltolini, M., 2010. Preferred orientation of phyllosilicates: Comparison of fault gouge, shale and schist. J. Struct. Geol. 32, 478–489. doi:10.1016/j.jsg.2010.02.003

Wenk, H.-R., Lonardelli, I., Franz, H., Nihei, K., Nakagawa, S., 2007. Preferred orientation and elastic anisotropy of illite-rich shale. Geophysics 72, E69–E75. doi:10.1190/1.2432263

Wenk, H.-R., Lutterotti, L., Vogel, S.C., 2012. Rietveld texture analysis from TOF neutron diffraction data. Powder Diffr. 25, 283–296. doi:10.1154/1.3479004

Wenk, H., Lutterotti, L., Kaercher, P., Kanitpanyacharoen, W., Miyagi, L., Vasin, R., 2014. Rietveld texture analysis from synchrotron diffraction images . II . Complex multiphase materials and diamond envil cell experiments. Powder Diffr. 29, 220–232. doi:10.1017/S0885715614000360

Wilkins, S., Mount, V., Mahon, K., Perry, A., Koenig, J., 2014. Characterization and development of subsurface fractures observed in the Marcellus Formation, Appalachian Plateau, north-central Pennsylvania. Am. Assoc. Pet. Geol. Bull. 98, 2301–2345.

Williams, H., Hatcher, R.D.J., 1982. Suspect terranes and accretionary history of the Appalachian orogen. Geology 10, 530–536.

Wilson, R.D., Schieber, J., 2015. Sedimentary Facies and Depositional Environment of the Middle Devonian Geneseo Formation of New York, USA. J. Sediment. Res. 85, 1393–1415.

Zak, J., Verner, K., Tycova, P., 2008. Multiple magmatic fabrics in plutons: an overlooked tool for exploring interactions between magmatic processes and regional deformation? Geol. Mag. 145, 537–551.

Zanazzi, P.F., Comodi, P., Nazzareni, S., Andreozzi, G.B., 2009. Thermal behaviour of chlorite: an in situ single-crystal and powder diffraction study. Eur. J. Mineral. 21, 581–589.

# 4. Texture development of clay-rich sediments across the Costa Rica subduction zone

* in revision as Kuehn, R., Stipp, M., Leiss, B., at *Journal of Geophysical Research: Solid Earth*

## Abstract

During sedimentation, burial and deformation at active continental margins, clay-rich sediments develop crystallographic preferred orientations (textures) due to the progressive alignment of phyllosilicates. Such textures help to interpret sedimentation and compaction conditions as well as tectonic processes at such convergent margins. We collected samples of varying depths from four different drilling locations across the Costa Rica Trench retrieved during IODP (International Ocean Discovery Program) expeditions 334 and 344 as part of the Costa Rica Seismogenesis Project (CRISP). Samples from the incoming Cocos Plate, the frontal prism and the slope of the overriding Caribbean plate were analyzed regarding their composition and texture. Sample composition is quite similar for all sample locations across the trench in the hemipelagic section as determined by X-ray powder diffraction analysis. Synchrotron texture analysis reveals that phyllosilicates in samples from the incoming plate show in general weaker textures than those from upper and middle slope of the overriding plate. Samples from the small frontal accretionary prism, however, correspond more to the incoming plate fabric according to their oceanic origin. Texture intensity depends on compaction, deformation, grain size, porosity and composition. In samples from the continental wedge and the frontal accretionary prism, we are able to distinguish tectonically undisturbed compacted sediments from core sections that suffered faulting and folding due to subduction-related deformation.

## 4.1. Introduction

The microfabric anisotropy of marine phyllosilicate-rich sediments generally increases during burial and progressive compaction at continental margins. This can be determined indirectly by, for example, AMS (anisotropy of the magnetic susceptibility) measurements, void ratios or preferred alignment of larger grains, e.g. illite flakes (e.g., Bowles et al., 1969; Agar et al., 1989; Kawamura and Ogawa, 2004; Kawamura, 2011; Schumann et al., 2014; Maffione and Morris, 2017) or more costly but also more accurately, by analyzing crystallographic preferred orientations (e.g., Kopf & Behrmann, 1997; Schumann et al., 2014). Microstructural parameters influencing the successive compaction besides increasing overburden load and pore pressure state are grain size distributions and shape fabrics of the grains. During compaction, platy grains typically rotate from a chaotic orientation with predominantly edge-to-edge and edge-to-face contacts towards an alignment parallel to the seafloor with

predominantly face-to-face contacts resulting in crystallographic preferred orientations (textures; Bennett et al., 1981; Bennett and Hulbert, 1986; Milliken and Reed, 2010).

As for platy phyllosilicates crystallographic and shape preferred orientations are closely linked, textures can control the physical properties and deformation behavior of such sediments (e.g., Carson et al., 1982; Oertel, 1983; Kock & Huhn, 2007; Mondol et al., 2007; Hashimoto et al., 2010; Schumann et al., 2014), hence the strain distribution in active continental margins and also the frictional behavior in the forearc wedge as well as in the subduction channel along the plate boundary. Sediment strength, friction and related seismogenic behavior are governed by, amongst other parameters, the mineralogical composition and fabric and their relevant physical properties (e.g., Kopf, 2013; Stipp et al., 2013; Schumann et al., 2014).

At erosive continental margins such as the Costa Rica margin (Figure 4.1), material from the overriding plate is tectonically eroded and transported within the subduction channel towards greater depth (von Huene et al., 2000; von Huene & Scholl, 1991; Ranero & von Huene, 2000). The properties of this material might be crucial for earthquake nucleation and rupture. During IODP Expeditions 334 and 344 in the Pacific Ocean offshore Costa Rica, westward of the Osa Peninsula, sedimentary and crustal material from the subducting Cocos plate and the overriding Caribbean plate were sampled. Drilling was part of the Costa Rica Seismogenesis Project (CRISP) which was aimed to investigate the nucleation and rupture of earthquakes at the erosional continental margin offshore Costa Rica (Vannucchi et al., 2012). The Costa Rica trench is well-known for shallow seismogenesis and tsunami generation as expressed in the 2002 Osa earthquake at 6 km depth (Arroyo et al., 2014) and the 2012 Nicoya earthquake at 13.1 km depth (Yue et al., 2013).

This study is intended to determine composition and texture of the sedimentary material of incoming and overriding plate, to detect overprinting by tectonic erosion or accretion, and to characterize the fabric differences with respect to the tectonic setting. Synchrotron texture analysis is the most suitable method for direct measurements of the textures of soft sediments with high water content as it contains swelling and hydrated minerals (e.g. smectite) and as intergranular water and hydrated minerals make other bulk texture methods like X-ray goniometry or neutron diffraction difficult or even impossible to apply.

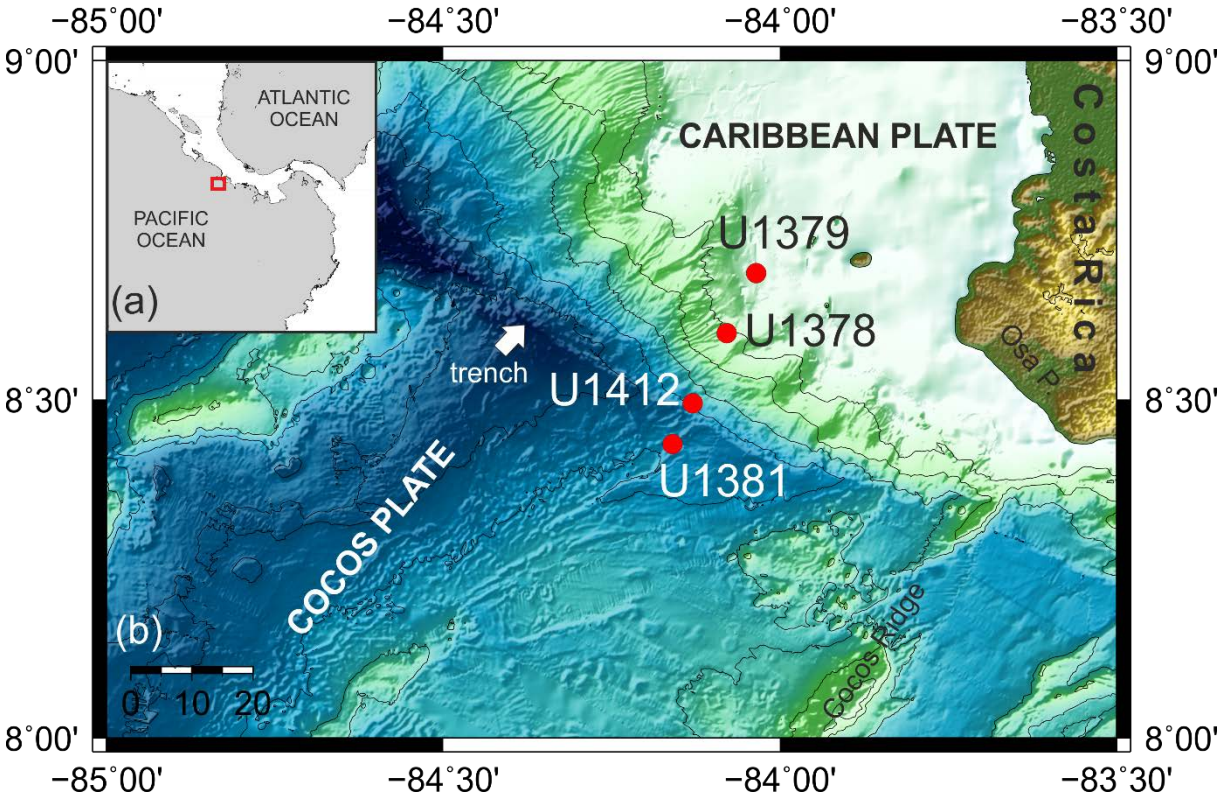


*Figure 4.1. Study area of IODP Expeditions 334 & 344 offshore Costa Rica. Inset (a) shows geographical position of bathymetric map shown in (b). Drill core locations of the samples used in this study and trace of the seismic cross section of Figure 2 are indicated in the bathymetric map. Core location U 1381 is located on the incoming Cocos plate. Core locations U 1378 and U 1379 are at the slope and location U 1412 at the frontal wedge of the overriding Caribbean plate. Map is based on the GEBCO data (The GEBCO_2014 Grid, www.gebco.net).*

## 4.2. Geological Setting and Sampling

The Costa Rica trench (Figure 4.2) represents the southern segment of the Middle America trench (MAT), where the Cocos plate is subducting beneath the Caribbean plate at a rate of 70-90 mm/yr (DeMets, 2001) with a shallow slab angle of <10° (Protti & Schwartz, 1994). Additionally, there is northwestward trench-parallel slip of ~14 mm/yr (DeMets, 2001).This part of the MAT is an erosive continental margin (von Huene et al., 2004; Ranero & von Huene, 2000), where the subducting Cocos plate removes material from the overriding Caribbean plate with an erosional rate of 115 km³/Myr/km (Vannucchi et al., 2003). The subducting crustal material of the Cocos plate is created at two locations: at the East Pacific Rise as well as the Cocos-Nazca spreading center. The Cocos plate crustal material is modified by the movement of the plate over the Galapagos hotspot that created the up to 2.5 km high Cocos Ridge (Barckhausen et al., 2001; von Huene et al., 2000). Cocos Ridge is now subducting below Osa peninsula, which is uplifted due to the elevation and the lower buoyancy of the Cocos Ridge. The oceanic crust except the Cocos Ridge is covered by a pelagic section of calcareous ooze from the Miocene covered by a hemipelagic section of clay and silty clay representing Plio-

and Pleistocene sedimentation. The frontal part of the overriding Caribbean plate directly at the thrust is a <10 km wide accretionary prism built up from oceanic sediments (Bangs et al., 2016). The accretionary prism continues landwards into a continental margin wedge consisting of folded and faulted sediments (Bangs et al., 2015, 2016). These sediments can be either interpreted as a depositionary forearc whose missing underlying forearc basement is supposed to be eroded by subduction erosion (Vannucchi et al., 2016), or as a very recent, rapidly growing accretionary prism (Bangs et al., 2016). The observed deformation is attributed to the compressional as well as the erosional nature of the subduction zone. The sequence is terminated by an unconformity and overlain by a relatively undeformed sedimentary slope cover of sand-, silt- and clay(stones) of Pleistocene age.

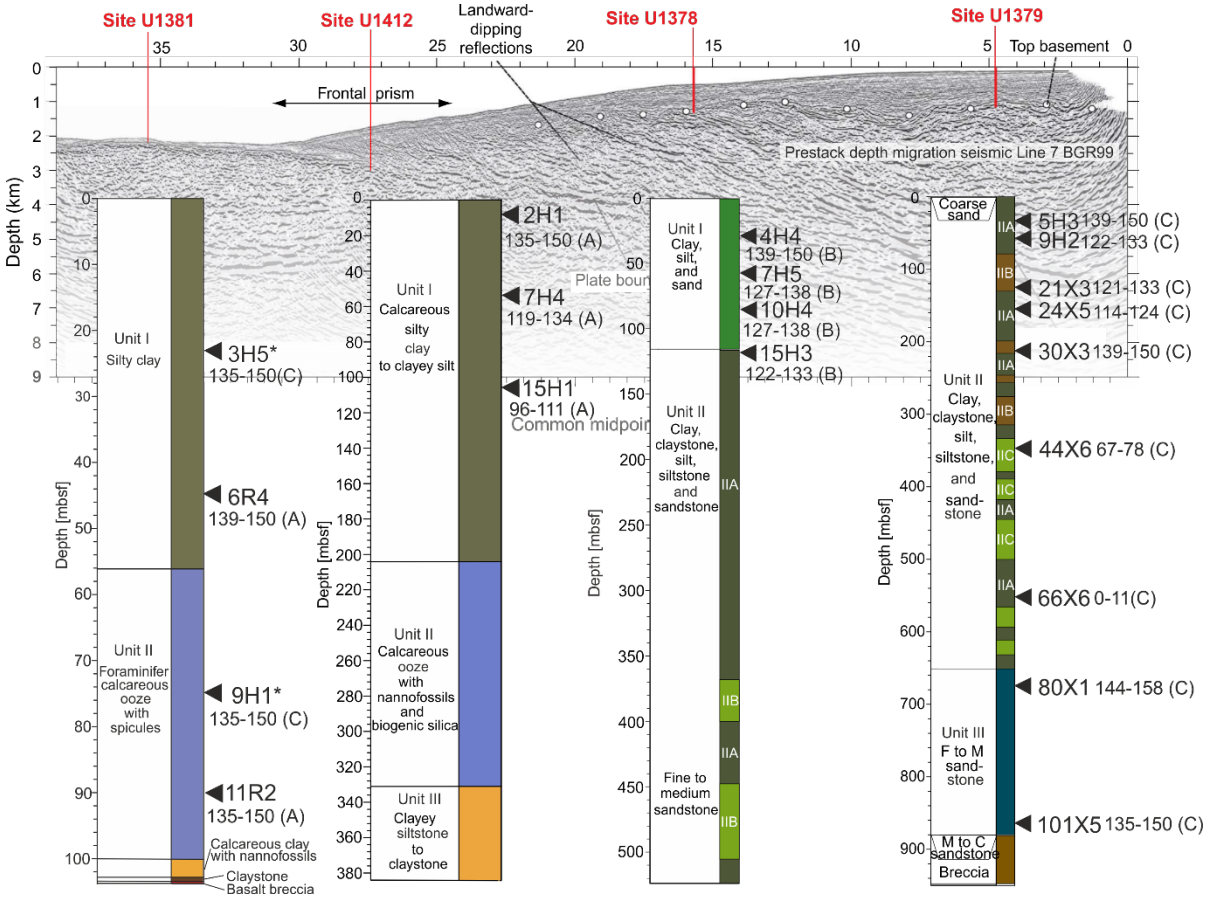


*Figure 4.2. Seismic cross section Profile Line 7 BGR99 (see trace in Fig. 1) with investigated drilling locations of IODP expeditions 334 & 344 offshore Costa Rica, modified from Harris et al., 2013; Vannucchi et al., 2012. Triangles with the abbreviated core section information indicate the samples used in this study. Stars mark samples, which are taken from drill core 1381 during expedition 334, while the core description is from expedition 344. F: fine, M: medium, C: coarse. Note the different total depths and hence length scales of the drill cores.*

We selected samples from four drilling locations penetrating the slope cover (Figure 4.2), one at the upper slope (U1379), one at the mid slope (U1378), one directly at the frontal accretionary prism (U1412) of the Caribbean Plate and one at the incoming Cocos plate (U1381). In most cores, our sampling was restricted to the uppermost 120 mbsf (meters below

sea floor). Only at Site U1379 samples from deeper levels (up to ~860 mbsf) could be collected. Samples in this study mainly represent the phyllosilicate-bearing hemipelagic core sections, but also two calcite-dominated pelagic samples are included. The full sample names are indicated in Figure 2. In the following text, we will refer to the samples by naming them after drilling location and core section (i.e. 1379 5H3).

## 4.3. Methods

### 4.3.1. XRD powder analysis

To gain precise information about the composition of the samples, XRD powder analyses were carried out. Mineral phases are crucial input parameters for Rietveld texture analyses. We used two methodical steps to finally get a quantitative analysis. First, to exactly determine the incorporated clay minerals, the grain size fraction <2 µm was extracted by the particle settling rate. Oriented mounts of the <2 µm fraction were prepared to enhance the peak intensity of the (00l) peaks. These mounts were measured in four different states: in air-dried condition, ethylene glycol desiccated for at least 48 hours, and heated for 30 minutes to 400 °C and 550 °C, respectively (e.g. Moore and Reynolds, 1997). The measurements at the different conditions were then compared to each other to identify clay minerals, which can share the same peak position (e.g. smectite and chlorite). The smectite (001) peak for example shifts from ~6.2°2ΘCuKα to ~5.2°2ΘCuKα when ethylene glycol treated, while the chlorite (001) peak, which is also located at ~6.2° 2ΘCuKα intensifies, when the sample is heated (e.g. Moore and Reynolds, 1997). Second, for quantitative analyses, whole rock powder samples were prepared by using the side loading technique, which provides the best conditions to prepare non-textured samples of phyllosilicate-bearing material (Środoń et al., 2001). XRD measurements were conducted using a *Philipps* PW1800 powder diffractometer with a Cu X-ray tube with an operating current of 30 mA and a voltage of 45 kV. Settings for the different measurement types are given in Table 4.1.

*Table 4.1. Instrumental settings used for the different XRD measurements. Whole rock powder was scanned with long counting time to get a high resolution for Rietveld refinement. Textured samples for clay phase identification were measured in a faster mode.*

| Sample | 2ΘCuKα range [°] | Step size [° 2ΘCuKα] | Counting time/step [s] |
|---|---|---|---|
| Whole rock powder for Rietveld | 4-65 | 0.02 | 12 |
| Textured sample fraction <2 µm<br>- air dried | 3-70 | 0.02 | 4 |
| -ethylene glycol desiccated | 3-32 | 0.02 | 4 |
| - heated 400 °C/ 550 °C | 3-32 | 0.02 | 4 |

Phase identification of the non-clay phases was conducted with the software *X'Pert HighScore* by *PAN'alytical*. Sample height correction of the diffraction patterns was based on the quartz (100) peak at ~20.85° 2ΘCuKα.

According to the diffraction patterns of the different measurement states, we identified the clay phases. Peak shifts and break downs (Figure 4.3) are characteristic for certain clay mineral phases (e.g. Moore and Reynolds, 1997). For a quantitative phase analysis the Rietveld powder measurements were analyzed using the Open Source software *Profex* (Doebelin & Kleeberg, 2015), which is based on the Rietveld code *BGMN* (Bergmann et al., 1998).

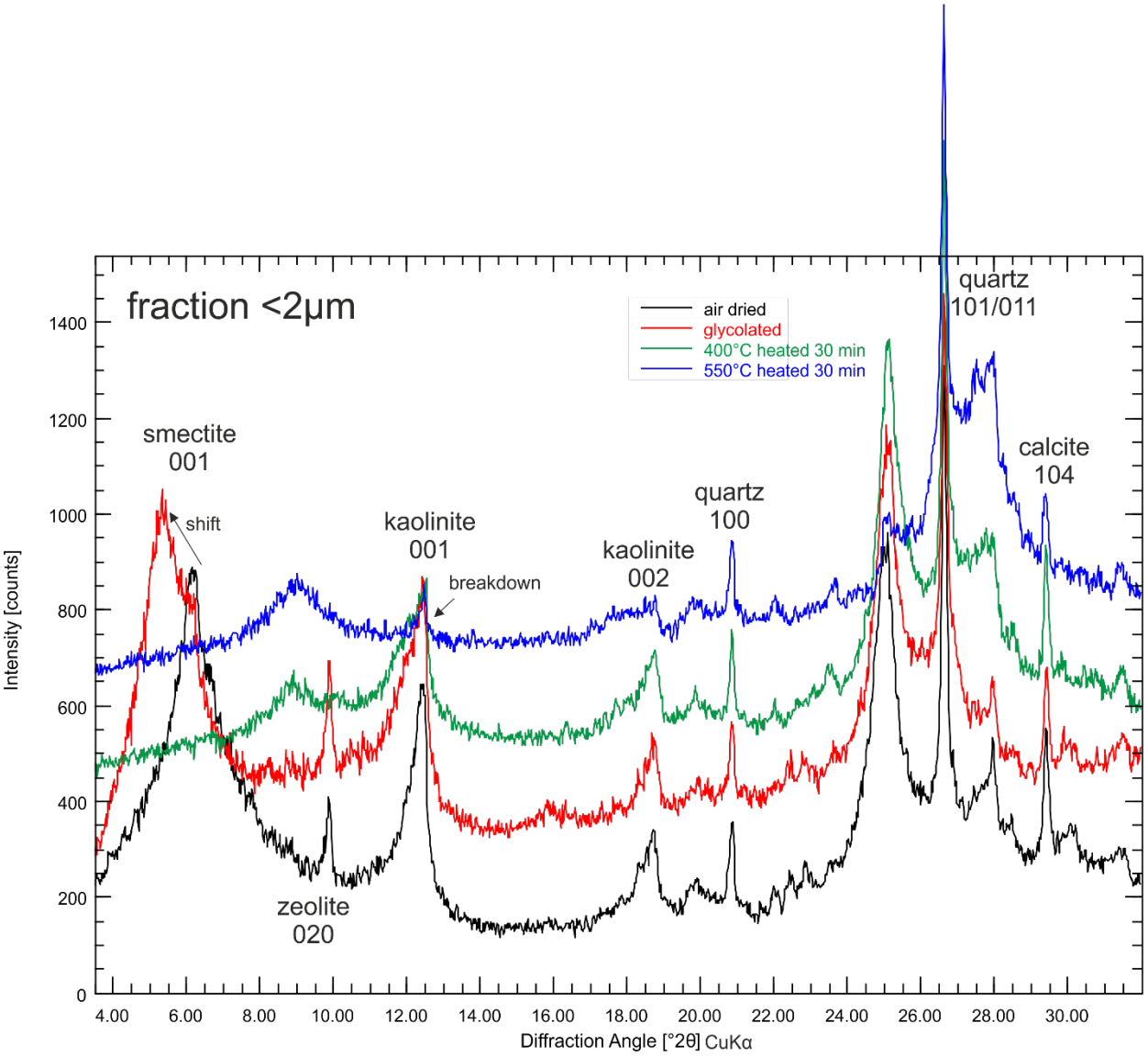


*Figure 4.3. Clay mineral phase identification by measuring at different conditions: air-dried, desiccated with ethylene glycol, heated to 400 °C and 550 °C. Smectite (001) is shifted to smaller 2Θ angles when ethylene glycol desiccated and breaks down when heated, Kaolinite (001) breaks down during heating between 400 and 550 °C.*

### 4.3.2. Synchrotron texture measurements

Cylindrical samples with a diameter of 10 – 20 mm were analyzed. If possible, samples were "cored" with a small core stamp that produces sample cylinders with a diameter of about 15 mm and then fixed in non-diffracting, small acrylic sample holders (Schumann et al., 2014). If it was not possible to core sample cylinders due to crumbly material, we tried to keep as close as possible a cylindrical sample shape to avoid any shape artifacts during synchrotron measurements.

Synchrotron measurements were carried out at the European Synchrotron Radiation Facility (ESRF) in Grenoble and at the German Synchrotron Radiation Facility (DESY) in Hamburg. The experimental setup consisted of a xyz-stage with a ω-rotation stage on which the sample was mounted. In a distance of ca. 1663 (ESRF) mm and 1250 mm (DESY) from the sample, a *Perkin Elmer* 2D-image plate detector was installed to measure in transmission mode. The beam size was limited to 500 x 500 µm and the energy of the beam was restricted to 80 keV at ESRF and 60 keV at DESY, which corresponds to a wavelength of ~ 0.155 Å (ESRF) and 0.208 Å (DESY). The samples mounted on the ω-rotation stage were rotated from 0° to 175° in 5°-steps resulting in 36 images. The size of the cylindrical samples varied in diameter, this led to an adjustment of the total measurement time per frame from 1 to 3 s at ESRF and 10-360 s at DESY. Due to the small beam size, one to three measurements at different y-positions were executed to improve grain statistics.

For data analysis the Open Access software MAUD (Materials Analysis Using Diffraction, Lutterotti et al., 1997), a code based on the Rietveld method (Rietveld, 1969) was used. MAUD applies a least squares fitting approach for polyphase sample materials which fits hypothetical peaks by given crystal lattices of certain minerals to the measured spectrum, and allows to calculate textures using the EWIMV algorithm (derived from WIMV; Matthies and Vinel, 1982). The program is suitable to calculate textures from clays and clay bearing samples as demonstrated by a number of studies (Omotoso et al., 2006; Wenk et al., 2010, 2007, Lutterotti et al., 2010; Vasin et al., 2013; Schumann et al., 2014a). The plate detector images were loaded in MAUD by integrating every image in 5° steps resulting in 72 different diffraction patterns per image and rotational step, respectively. As we measured 36 images per sample, this produces a total of 72 x 36 = 2592 spectra per sample measurement. For Rietveld texture analysis, only the main rock forming minerals (>5%) were fitted to reduce calculation time. Textures of minerals with small portions cannot be adequately modelled and are not significant for the texture development at all. Crystallographic input phase data (cif-files) available from the Crystallographic Open Database (Grazulis et al., 2009) and the AMCDS data base (Downs & Hall-Wallace, 2003) were used for the refinement process: quartz by Antao et al. (2008), calcite by Graf (1961), anorthite by Wainwright & Starkey (1971), illite by Gualtieri et al. (2008), kaolinite by Bish & Von Dreele (1989). Due to material science conventions, for minerals with

monoclinic symmetry the unique folding axis has to be changed from b to c (Lutterotti et al., 2010; Matthies & Wenk, 2009). For smectite, montmorillonite by Gournis et al. (2008) was used and the basal distance initially increased to 15.2 Å to represent a hydrated smectite (Moore & Reynolds, 1997). In addition, amorphous silica from fossil remnants is inherited in the samples (Kurzawski et al., 2016, 2018), but as it is not a crystalline phase and therefore not contributing to the anisotropy of the samples, it is ignored here and subtracted with the background.

## 4.4. Results

### 4.4.1. Sample composition

In the core from the upper slope (1379C), the samples 5H3, 9H2, 21X3, 24X5, 30X3, 44X6 and 66X6 originate from the various subunits of Unit II with clay, claystone, silt, siltstone and sandstone, while samples 80X1 and 101X5 were collected from the subjacent fine to medium sandstone unit. An overview of the full sample compositions is given in Figure 4.4. The smectite content is very variable ranging from 17 wt.-% in 21X3 to 41.5 wt.-% in 101X5. Kaolinite ranges from 7.1 wt.-% in sample 5H3 to 22.2 wt.-% in sample 30X3 and illite, present in six of the samples, varies (if present) from 6.6 wt.-% (44X6) to 18.5 wt.-% (21X3). Of the non-clay minerals, plagioclase is most abundant ranging from 11.1 wt.-% in sample 80X1 to 24.7 wt.-% in sample 5H3. Quartz ranges from 10.3 wt.-% (44X6) to 15.5 wt.-% (80X1), and calcite from 0.3 wt.-% in 24X6 to 9.1 wt.-% in 80X1. Zeolites constitute up to 10.3 wt.-% (66X6).

In the samples from the mid slope (1378B), the three uppermost samples 4H4, 7H5 & 10H4 originate from the clay, silt and sand unit, while sample 15H3 originates from the clay, claystone, silt, siltstone and sandstone unit. The main constituent mineral is also smectite (Figure 4), ranging from 28.3 wt.-% (15H3) to 37.6 wt.-% (4H4), followed by plagioclase (12 wt.-% in 15H3 to 24.7 wt.-% in 7H5) and kaolinite (10.2 wt.-% in 4H4 to 20.5 wt.-% in 7H5). Quartz content is equal in all samples around 11 wt.-%, while calcite strongly varies from 2.2 wt.-% (sample 7H5) to 14.7 wt.-% (sample 4H4). Illite occurs only in two samples with 3.3 wt.-% (7H5) and 13.1 wt.-% (15H3). Zeolite minerals vary from 3.8 wt.-% in sample 4H4 to 8 wt.-% in sample 10H4.

In the samples from the accretionary frontal prism (1412A) (calcareous silty clay to clayey silt), smectite is the most abundant mineral (Figure 4.4), ranging from 31.5 wt.-% in sample 2H1 to 48.9 wt.-% in sample 7H4, followed by plagioclase (from 13.2 wt.-% in 15H1 to 22.6 wt.-% in 2H1) and kaolinite (from 13 wt.-% in 2H1 to 17.4 wt.-% in 7H4). Quartz content in all samples is about 10 wt.-%, while calcite varies between 4.1 wt.-% (7H4) to 10.3 wt.-% (15H1). Zeolite minerals range from 2.5 wt.-% in sample 7H4 to 4.9 wt.-% in 2H1.

In cores 1381A and C from the incoming plate the hemipelagic and pelagic samples are clearly distinguished by their smectite and calcite content (Figure 4). In the hemipelagic silty clay samples the amount of smectite ranges from 45.7 wt.-% in 3H5 to 53.1 wt.-% in 6R4 and

kaolinite from 16.1 wt.-% in 6R4 to 12.8 wt.-% in 3H5. We found 12.7 wt.-% (6R4) to 14.6 wt.-% (3H5) plagioclase, 4 wt.-% (6R4) to 4.8 wt.-% (3H5) calcite and 7.3 wt.-% (6R4) to 10 wt.-% (3H5) quartz and ~3 wt.-% zeolites. In contrast, the pelagic calcareous ooze samples contain 53.8 wt.-% (9H1) and 71.1 wt.-% (11R2) calcite, 6.3 wt.-% (11R2) to 24.2 wt.-% (9H1) plagioclase and no quartz. Smectite is also present with 7.9 wt.-% in sample 9H1 and 12.8 wt.-% in sample 11R2, as well as minor amounts (3.8 wt.-% in 11R2 and 6.5 wt.-% in 9H1) of kaolinite.

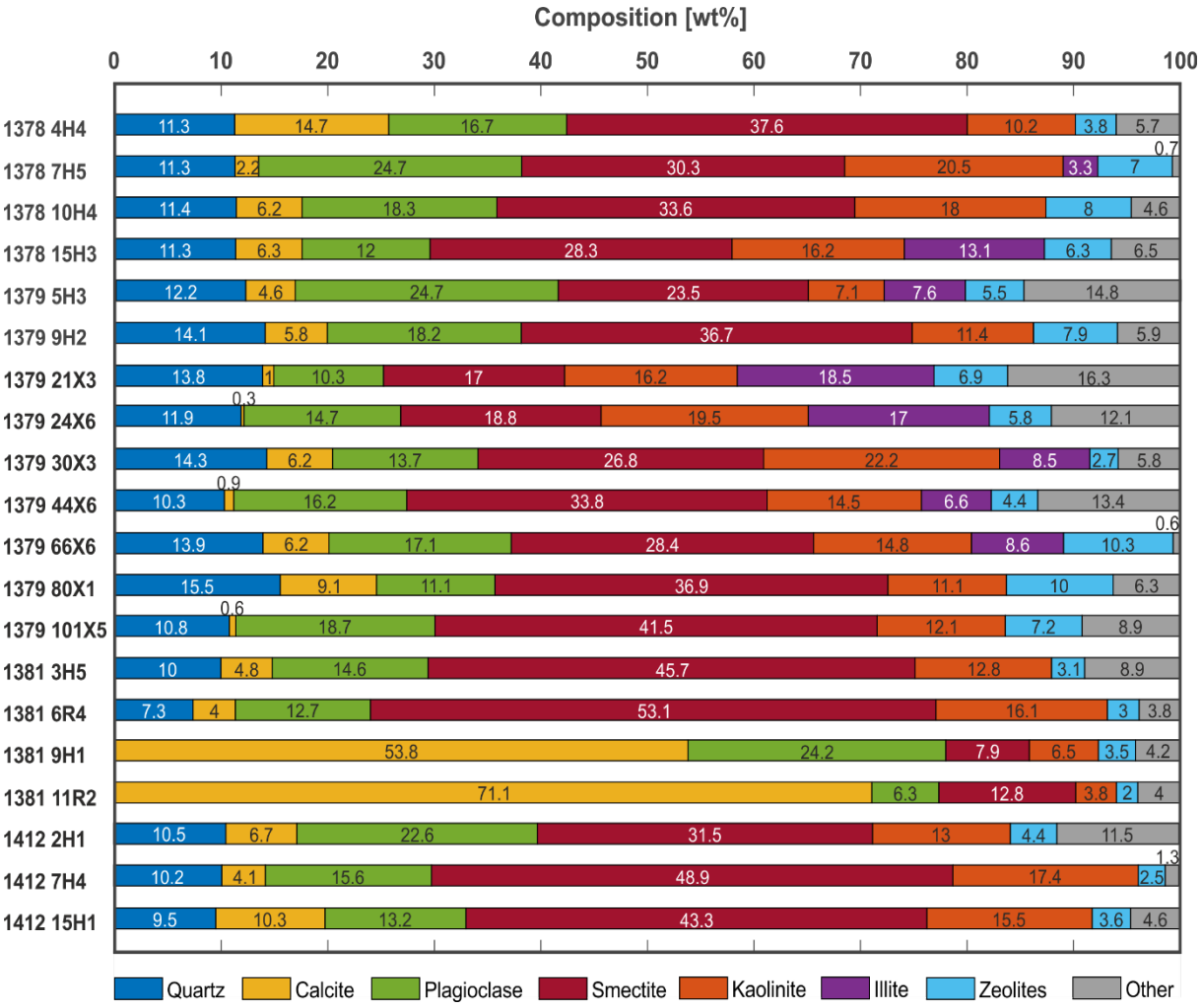


*Figure 4.4. Quantitative sample compositions determined from whole rock X-ray powder analysis. "Other" contains the minerals aragonite, pyrite, chlorite and halite. The two pelagic samples (1381 9H1 and 1381 11R2) are clearly distinguished from the hemipelagic samples by their calcite content.*

### 4.4.2. Texture analysis

#### *4.4.2.1. Textures of phyllosilicates*

In the sediments from the upper slope (1379C, Figure 4.5a) most phyllosilicate (001)-maxima are single maxima parallel or subparallel to the core axis, except for sample 44X6 (351 mbsf), which shows a girdle distribution inclined from the core axis, and 66X6 (554 m) which shows a single maximum inclined from the core axis. The pole figure pattern of the (001)-maximum is the same for all three phyllosilicate phases. Smectite (001) maxima increase with depth from 1.3 mrd (multiples of random distribution) in sample 5H3 (35 mbsf) to 2.3 mrd in sample 30X3 (213 mbsf), then decreasing again to 1.5 mrd in sample 101X5 (867 mbsf). Kaolinite (001) maxima have slightly stronger intensities starting from 1.73 mrd in sample 5H3, increasing towards 2.95 mrd in sample 66X6 and then decreasing again to 1.61 mrd in sample 101X5. Illite, if present, starts from 1.8 mrd in sample 5H3, increases to 3.15 in sample 44X5 and then decreases to 2.17 mrd in sample 66X6.

In mid-slope samples from core 1378B, the incorporated phyllosilicates mostly show a (001) maximum perpendicular to the bedding with a slight inclination. An exception is sample 7H5 where the maxima are inclined by 45° with respect to the core axis. Phyllosilicate texture intensity decreases from sample 4H4 (29 mbsf) to sample 7H5 (60 mbsf), but increases slightly towards greater depths.

Smectite and kaolinite pole figures in samples of core 1412A from the frontal prism, show a slight preferred orientation with a single maximum, which is inclined from the core axis ~10° in sample 7H4 (55 mbsf) and ~45° in samples 2H1 (7 mbsf) and 15H1 (106 mbsf). Texture intensity does not increase with depth.

In hemipelagic and pelagic samples at Site U1381 from the incoming plate, smectite (001) pole figures show a weak single or non-symmetric maximum oriented parallel or sub-parallel to the core axis. Kaolinite is only present in the hemipelagic samples and shows a broad, not very strong maximum with the same (001) orientation as the smectite.

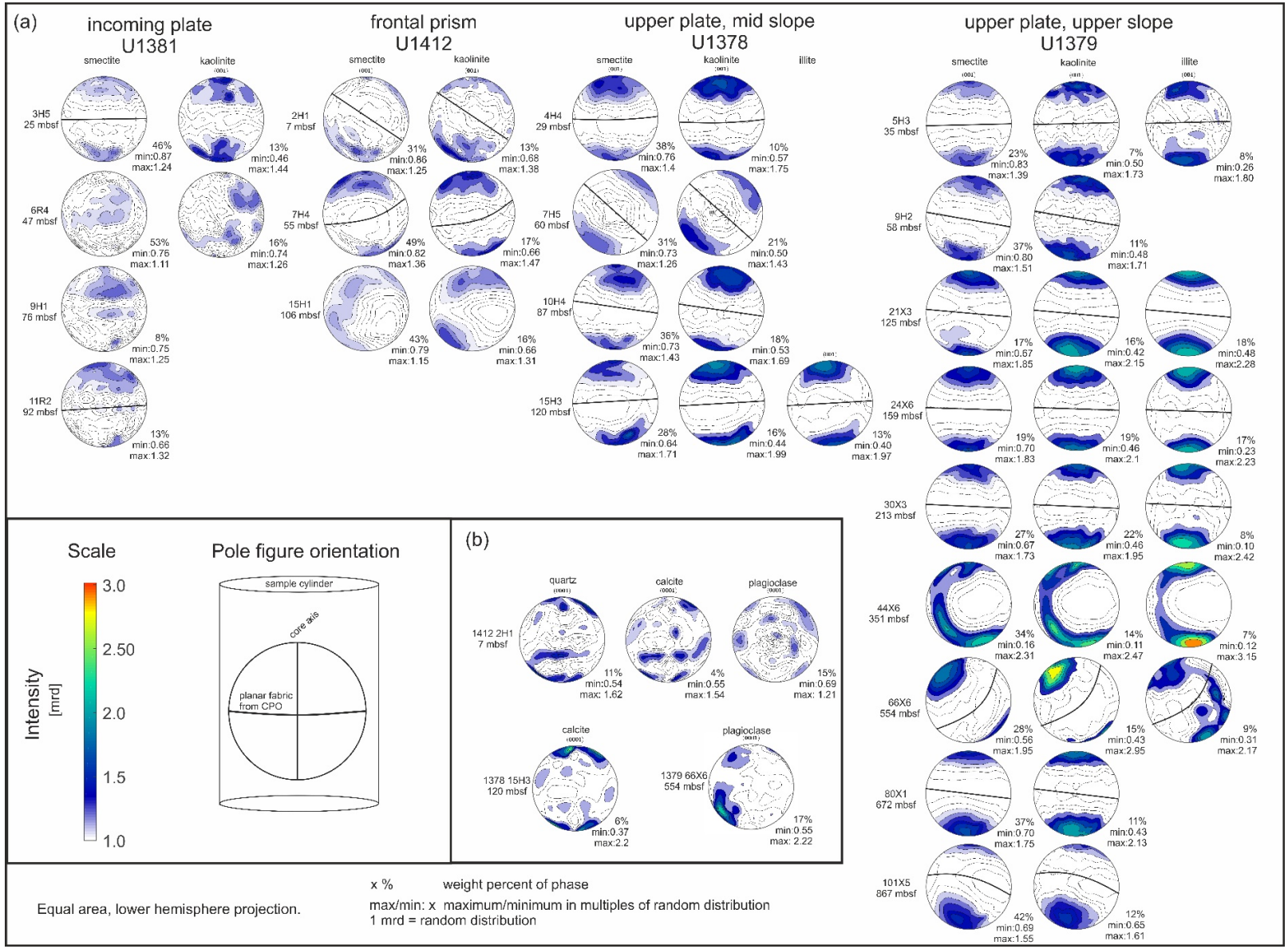


*Figure 4.5.*
*a) Recalculated pole figures of phyllosilicate minerals (001) arranged by location and depth. Planar fabric orientation is inferred from 00l maximum inclination. b) Exemplary recalculated pole figures of non-clay phases. Equal area, lower hemisphere projection. Maxima in mrd (multiples of random distribution). Pole figures for quartz, calcite and plagioclase in sample 1412 2H1 which are dominated by irregular reflections. Strong calcite (001) maximum in sample 1378 15H3. Strong plagioclase (001) maximum in sample 1379 66X6.*

#### *4.4.2.2. Textures of non-clay minerals*

Quartz, plagioclase and calcite pole figures in most of the hemipelagic samples are dominated by irregular reflections, caused by e.g. single crystal diffractions or minor phases (Figure 4.5b). Exceptions are the calcite (001) pole figure in mid-slope sample 1378 15H3, which shows a strong double maximum parallel to the core axis. A large fossiliferous component aligned subparallel to the bedding might generate this. Plagioclase only showed a texture in sample 1379 66X6 from the upper slope, which has a maximum of 2.2 mrd. A large plagioclase single grain might cause this. In the pelagic, calcite dominated samples from the incoming plate no calcite preferred orientation can be observed.

## 4.5. Discussion

In the following, we discuss the composition of the sediments, the origin and development of the observed textures and the implications, which arise for the regional tectonic framework. In addition, we discuss the advantage of synchrotron texture analysis for our samples in comparison to other methods.

### 4.5.1. Synchrotron texture analysis

Non- or partly lithified, water-containing soft sediments are difficult to analyze when studying the crystallographic preferred orientation (texture). Synchrotron texture analysis is the only method, which meets all necessary requirements of sample preparation, measurement and data analysis. First, sample disturbance usually occurs during sample preparation. Water-rich samples like ours with a porosity of 70% or even a little bit higher require a special treatment for most microfabric investigations, e.g., freeze-drying or replacing sample fluid by low-viscosity resin to withstand further mechanical or chemical polishing as necessary for X-ray texture goniometry (XTG) or scanning electron microscopy (SEM). These preparation procedures at least significantly modify the soft and sensitive microfabric of the soft sediments. By punching out full sample cylinders (Schumann et al., 2014), we restrict fabric manipulation to the sample outline, i.e. the outermost tenth and usually not more than a few 100 µm wide zone that becomes negligible when investigating sample volumes with 15 to 20 mm in diameter for texture analysis. The use of a sample volume according to the high penetration depth of the high-energy synchrotron X-rays, provides orders of magnitude better grain statistics than surface-bound methods like XTG and electron backscatter diffraction (EBSD) at the SEM.

By summing up data from several sample slices acquired perpendicular to the long axis, we further enhance grain statistics and provide a good representation of the sample. Our samples exhibit a broad grain size distribution, ranging from clay size fraction to sand and may even include mm-size shell fragments. The orientation of all these grain sizes can be captured, as there is no optical resolution limit like for optical universal stage or EBSD. By rotating the

sample 180° in 5° steps, we achieve full pole figure coverage with a 5° grid, as we extract diffraction patterns every 5° from the plate detector images. This is a higher resolution as, for example, used by Lonardelli et al. (2007), Wenk et al. (2008b), or Kanitpanyacharoen et al. (2015), who rotated their samples about 60-90° by measuring every 10-15° and did not get full pole figure coverage. Especially for our heterogeneous material it is important to reach a good pole figure coverage, which represents the fabric adequately, due to grain size variability, number of different mineral phases, and weak preferred orientations. In transmission mode, we can use a large range of the 2Θ-spectra (0.6-6°$2\Theta_{\lambda=70keV}$) as no defocusing errors occur at high reflection angles like in XTG measurements. Due to the adjustable sample detector distance, we are also able to resolve small 2Θ-angles, which include the important clay mineral (001)-peak positions. This can be very difficult with XTG, because too small reflection angles produce a high scattering background.

By using Rietveld analysis, we can analyze all sample components, which contribute to the anisotropy, even though the composition is complex. Earlier studies had to use different methods for different mineral phases (e.g. Kopf & Behrmann 1997: XTG for smectite, relative orientation of particles in optical microscopy), which may have led to incomplete data sets. Background scattering from incorporated water molecules is increased by amorphous silica, which locally (~2.2° $2\Theta_{\lambda=70keV}$) contributes to the background as broad hump (e.g. Ghisoli et al. 2010). As we consider the full spectra for background calculation, we can better subtract these features. Using multiple peaks for texture analysis we can determine the texture more accurately than by using only single peaks like for XTG. In clay-rich samples peak overlapping is frequent. Nevertheless, as we consider multiple phases contributing to peak intensities with Rietveld, we can consider all minerals and all belonging peaks, which might contribute to the fabric anisotropy. In comparison to AMS measurements and microstructure observations, we can quantify the orientation of the different included minerals contributing to the total anisotropy.

### 4.5.2. Composition

The quantitative mineralogical composition of the sediments from the incoming Cocos Plate has been subject to several studies (e.g. Spinelli and Underwood, 2004; Kameda et al., 2015). Regarding the hemipelagic sediments, these studies are largely comparable to what we found. Only a lower quartz content in the Spinelli and Underwood (2004) study with 2-5 wt.-% quartz compared to 7-10 wt.-% in our study can be observed, which might arise from local heterogeneities, as these samples originate from offshore Nicoya Peninsula which is ~200 km further north. Differences might also result from methodical aspects, as our “clay” represents all clay minerals and is not restricted to the <2 µm fraction as in the other studies. The composition of the pelagic calcareous ooze in contrast, differs largely. Kameda et al. (2015)

did not detect clay and Spinelli and Underwood (2004) determined trace amounts to 6 wt.-% clay, while we measured 15-19 wt.-% clay minerals. Same holds for plagioclase, with 4-8 wt.-% (Spinelli & Underwood, 2004) and 15 wt.-% in average (Kameda et al., 2015) while we found 6-24 wt.-%. Consequently, we found a lower calcite contribution than the other studies (Spinelli and Underwood, 2004: 83-92 wt.-%; Kameda et al., 2015: 85 wt.-%; this study: 54-71 wt.-%). The differences may arise from different methods in calcite content determination. While we applied powder diffractometry measurements, Kameda et al. (2015) used a leaching technique and Spinelli and Underwood (2004) determined the total inorganic carbon by coulometry. However, it is quite likely that most of the data differences are related to compositional sample-to-sample variability.

Unfortunately, there is no published quantitative data for samples from the overriding Caribbean plate offshore Costa Rica. However, the qualitative results (i.e. the minerals identified) described by Vannucchi et al. (2012) and Harris et al. (2013) are in good agreement with our results as we detected the same minerals. Even though two samples from the core 1379C originate from Unit III, which is described as fine to medium sand (Vannucchi et al., 2012), the portion of quartz and plagioclase is not significantly higher than in other samples described as silt or silty clay. This might indicate that the quartz and plagioclase grains in the other units are predominantly silt size but constitute the same volumetric proportion.

### 4.5.3. Texture development with ongoing compaction

The platy shape of phyllosilicates requires the grains to align by a kind of a rigid body rotation process during progressive burial, contemporaneous to the reduction of porosity and dewatering. The latter should progressively intensify the texture strength with increasing depth and compaction (e.g., Voltolini et al., 2009). A general reduction of porosity with increasing depth is observed in the investigated cores of this study (Figure 4.6; data from Vannucchi et al., 2012, and Harris et al., 2013). Deviations from the general trend are probably mainly due to variations in composition and grain fabric as well as the local rate of burial and compaction. For the uppermost 100 mbsf of the sediment sequence, present in all drill cores, there is no general trend in texture development and intensification with depth. The cores show variable and weak fabrics, indicating that the onset of texture development is chaotic and in the uppermost part not primarily controlled by burial, dewatering and hence decreasing porosity but by other factors (Figure 4.6). Maffione and Morris (2017) determined the onset of fabric development in clay-rich sediments from the Philippine Sea in a zone of 83-113 mbsf using AMS data. Even though we already found a weak fabric at shallower depth, we observe a significant increase from 1.5 mrd to 1.8 mrd between 58 and 125 mbsf samples in core 1379, and from 1.4 mrd (87 mbsf) to 1.7 mrd (120 mbsf) in core 1378, which support the findings of

Maffione & Morris (2017). In this depth range, also the characteristic basal fabric of the phyllosilicates becomes predominant.

For greater depths, we can only rely on 1379C as we have only from this core samples down to greater depth to ~867 mbsf. A rough increase in intensity of pole figure maxima can be observed, which has already been described by earlier studies for other IODP drill cores (e.g., Kopf and Behrmann, 1997; Schumann et al. 2014). The texture intensification stops at a depth of ~350 mbsf that corresponds to a grain coarsening of the sediment indicated by the occurrence of silty sand and sandstone (Subunit IIC), followed by fine to medium sandstone (Unit III) (Vannucchi et al., 2012). Several studies demonstrated that an increase of quartz content in clay samples negatively correlates with fabric development (Curtis et al., 1980; Sintubin, 1994; Voltolini et al., 2009). We did not detect a significant increase in quartz content, but an increase of non-platy particles may also weaken the fabric. Below ~350 mbsf, the phyllosilicate alignment is more strongly affected by grain size, as larger grains do inhibit the rotation of platy phyllosilicates more effectively.

In most of the samples, we observe a stronger texture for illite and kaolinite than for smectite. This might be caused by a more flocculated microstructure of smectite that remains preserved during compaction. Smectite is less compactable than kaolinite and illite, which is attributed to a larger number of smaller grains resulting in a better distribution of stress over the grain contacts by Mondol et al. (2007). A chaotic aggregate of platy minerals with variable orientation cannot be aligned as easy as single platy crystals in a matrix of small, equant and rounded grains (Mondol et al., 2007). Kopf and Behrmann (1997) and Schumann et al. (2014) observed a stronger maximum for illite than for smectite and kaolinite in oceanic sediments that can at least partly be related to large illite flakes in these studies. All other minerals, i.e., mainly quartz, plagioclase and calcite, do not show any texture trends that can be related to grain shape and size-dependent effects on compaction.

### 4.5.4. Origin of texture

In most of the samples, a preferred orientation of quartz, plagioclase and calcite cannot be observed. Exceptions, as shown in Figure 4.5, are due to large single crystals, for example plagioclase from volcanic ash, or shell fragments, which have been described from smear slide analysis of the cores (e.g., Vannucchi et al., 2012) or for other drilling locations, for example, the Nankai accretionary prism offshore SW-Japan (Schumann et al., 2014).

Platy phyllosilicates tend to align perpendicular to the direction of vertical effective stress, induced by the overburden, or become aligned parallel or subparallel to a fault plane (e.g. Moon and Hurst, 1984). Accordingly, the planar fabric is perpendicular to the (00l) maxima of the phyllosilicates. Regarding crystallographic preferred orientation and intensity four characteristic texture types are distinguishable:

Samples with a planar fabric perpendicular or at a great angle to the core axis most likely represent the undisturbed, horizontal or nearly horizontal bedding plane (see Figure 4.5). For most samples this corresponds to a maximum slope angle of 5-7° reported for the slope offshore Costa Rica (Vannucchi et al., 2003) and bedding dips determined by shipboard measurements at the split core sections (Vannucchi et al., 2012; Harris et al., 2013). For some samples (marked in green in Table 4.2), our results agree well within a difference of ≤5° to the shipboard data. If they do not fit this might be related to the spatial distance between our whole round samples and the next measured bedding plane in the core indicating fabric heterogeneities caused by local cross-bedding or local slope changes or, alternatively, by the local occurrence of discrete faults.

Samples with a more strongly inclined single maximum (>15°: 1379 101X5, 1378 7H5, 1412 2H1, 1412 7H4) may represent tectonically tilted sediment packages. At such high angles wet slope sediments are supposed to be remobilized, excluding a pure sedimentary origin of these bedding inclinations. Sample 1379 66X6 is also inclined by 45°; but as observed from split core images (Vannucchi et al., 2012) the sediment core is fractured and fragmented, and therefore we cannot prove if the bedding plane orientation is true or if the fragment experienced a drilling-induced rotation. Nevertheless, the observed texture intensity can be interpreted, as any fragment rotation would not influence the occurrence of pole figure maxima, but only their exact position.

Samples 1379 44X6 and 1412 15H1 show girdle or partial girdle fabrics of the phyllosilicates instead of a single maximum. Small-scale folds can explain such an orientation distribution and here possibly drag folding close to a fault plane. Documented faulting within the 300-350 mbsf section in core 1379C (Vannucchi et al., 2012) supports this interpretation. Other small-scale folding could also explain these girdle fabrics.

Weak and non-symmetric fabrics of the hemipelagic samples from the incoming plate (U1381) contrast to the symmetric fabrics with predominant basal maximum of the samples from the overriding plate of comparable composition and depth. Considering the higher porosity in the samples from the incoming plate as documented by shipboard porosity measurements (Harris et al., 2013; Vannucchi et al., 2012), which is approximately 5-10% higher than in overriding plate samples, it can be stated that the (hemi)pelagic sediments are less compacted and therefore less textured. Furthermore, the amount of phyllosilicates in the (hemi)pelagic samples is relatively low and a pronounced phyllosilicate texture is therefore more difficult to attain and would require higher compaction strain. Finally, the incoming plate sediments are largely undeformed, whereas the sediments of the overriding plate are considerably deformed as outlined in the following section and this contributes to their generally stronger texture.

*Table 4.2. Comparison of dip angle determined from 00l orientation of texture measurements to dip angles from shipboard measurements above and below the actual sample position in the core. * data from (Harris et al., 2013; Vannucchi et al., 2012). Abbreviations: b: bedding, f: fault, sz: shear zone, l: lamination, as interpreted by shipboard scientists, ta: tectonic activity.*

| Sample (depth [mbsf]) | Dip from 00l maximum | Dip from core above actual sample*(depth [mbsf]) | Dip from core below actual sample*(depth [mbsf]) | Fit of 00l dip and core dip (± 5°) |
|---|---|---|---|---|
| Mid slope | | | | |
| 1378 4h4 (29.30) | 2° b | 5° b (26.72) | 2° b (32.53) | |
| 1378 7h5 (60.07) | 42° ta | 2° b (57.84) | 6° b (62.61) | |
| 1378 10h4 (86.99) | 8° b | 10° b (84.26) | 8° b (92.09) | |
| 1378 15h3 (119.87) | 3° b | 26° b (116.27) | 4° b (121.77) | |
| Upper slope | | | | |
| 1379 5h3 (34.59) | 1° b | 19° b (32.24) | 35° b (38.85) | |
| 1379 9h2 (58.22) | 10° b | | 10° b (61.03) | |
| 1379 21x3 (124.71) | 5° b | 12° b (123.99) | | |
| 1379 24x6 (158.54) | 2° b | 12° b (157.23) | 3° b (159.05) | |
| 1379 30x3 (213.09) | 3° b | 8° b (176.83) | 8° b (247.28) | |
| 1379 44x6 (350.77) | 2.5° ta | 46° f (343.92) | 16° sz (353.91) | |
| 1379 66x6 (553.50) | 45° b | 28° b,f (546.44) | 4° b (559.54) | |
| 1379 80x1 (671.64) | 7° b | 58° f (670.94) | 8° b (672.03) | |
| 1379 101x5 (866.95) | 15° b | 61° f (865.8) | | |
| Incoming Plate | | | | |
| 1381 3h5 (24.95) | 0.5° b | 16° b (26.75) | | |
| 1381 6r4 (47.39) | n.d. | 0° b (51.75) | | |
| 1381 9h1 (75.95) | n.d. | 10° b (76.2) | 0° b (76.32) | |
| 1381 11r2 (92.35) | 3° b | 0° b (91.9) | | |
| Frontal Prism | | | | |
| 1412 2h1 (7.25) | 34° b | 11° b (6.73) | | |
| 1412 7h4 (54.62) | 17° b | 67° b (54.34) | | |
| 1412 15h1 (105.56) | 12°b,ta | 5° l (98.9) | | |

### 4.5.5. Deformation features of the active continental margin off Costa Rica

Considering the above-discussed aspects of texture type and intensity, the different zones of the active continental margin offshore Costa Rica can be characterized by their texture. Sediments from the incoming plate are only weakly textured, most likely due to small grain sizes, high water content, slow compaction rates and the absence of tectonic strain.

In the frontal accretionary prism we mostly found weakly textured, probably tectonically tilted or deformed sediments. The generally weak textures might be related to their origin on the incoming plate followed by their accretion in the frontal prism, as determined by Bangs et al. (2016). This means that the process of frontal accretion might not enhance texture strength but cause the small scale folding documented in sample 1412 15H1. Its possible relation to faulting is most likely a result of accretion and compressive deformation and not a relict

microfabric of the incoming plate sediments. Hence, the fabric is mainly controlled by original sedimentation (composition), initial compaction and accretionary tectonics.

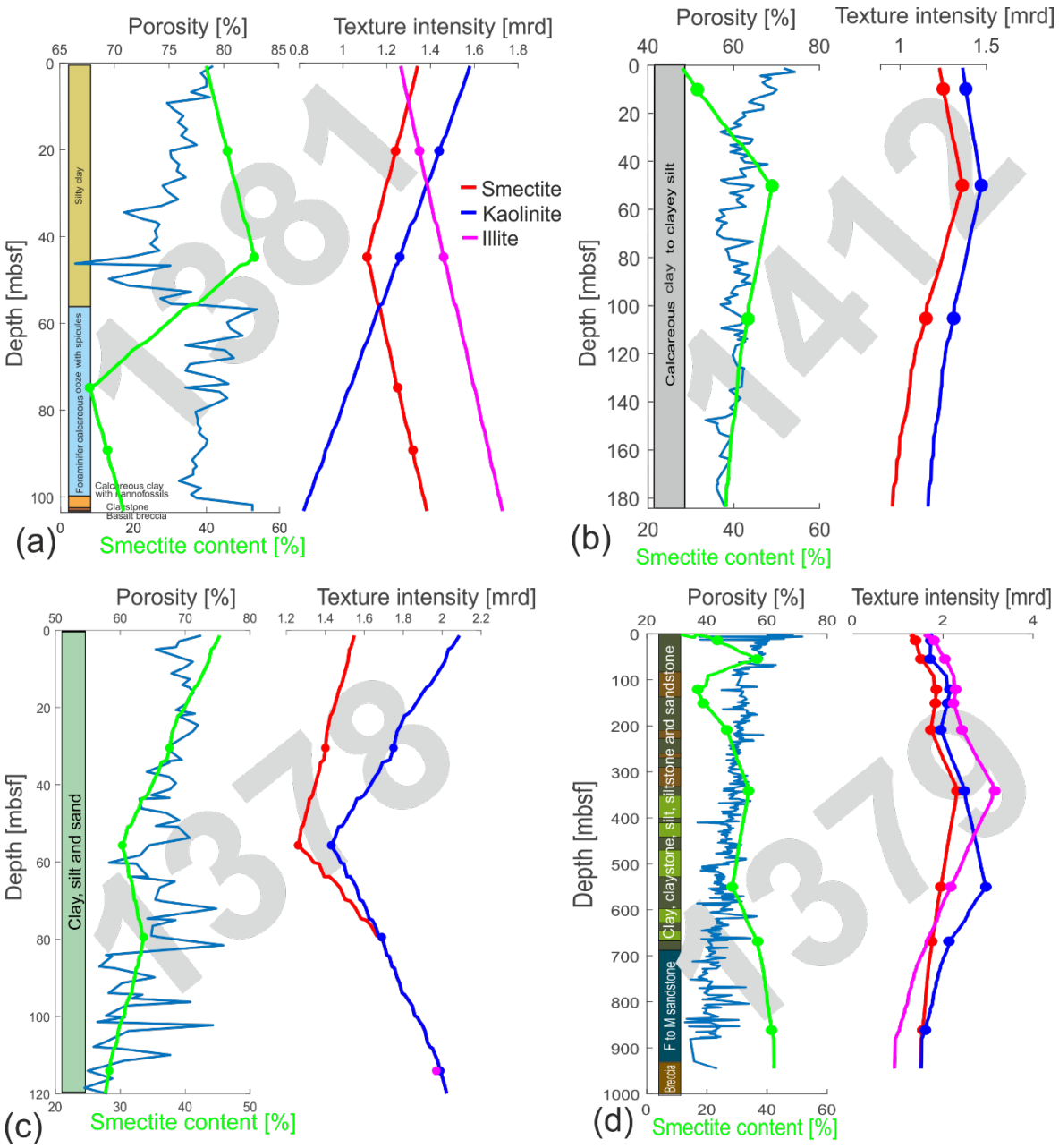


*Figure 4.6. Texture intensity versus porosity and smectite content with increasing depths for smectite, kaolinite and illite at all locations. Texture intensity of the three phases is largely corresponding within the cores, but generally lower in the incoming (1381) and accreted (1412) sediments. Figure includes data from Harris et al. (2013) and Vannucchi et al. (2012).*

In contrast to (hemi)pelagic sediments from the incoming plate and the accretionary frontal prism discussed before, sediments from the slope cover of the mid and upper slope are in general stronger textured (0.1-0.2 mrd stronger at corresponding depth) and mostly contain horizontal or slightly inclined bedding. These sediments show compositions mostly lower in

smectite and a generally 5-10% lower porosity compared to incoming plate and accretionary prism (Harris et al., 2013; Vannucchi et al., 2012; Figure 4.6). The lower porosity is probably caused by the different grain sizes as documented in the core description and mentioned before. The slope cover sediments contain clay, silt and sand-sized particles (Vannucchi et al., 2012) in contrast to the incoming and accreted sediments, which consist almost exclusively of clay and silt (Figure 4.2). In addition, deformation within the mid and upper slope cover sediments is much more intense as indicated by the structural core descriptions (Vannucchi et al., 2012). Correspondingly, we locally observed textures indicative of tectonically inclined, deformed and small-scale folded sediments apart from the overall compaction texture record. In contrast, the two samples from greater depth, which are assumed to represent an earlier and larger accretionary prism by Bangs et al. (2016), show only moderate tectonic reworking mainly expressed by tilted sediment blocks.

## 4.6. Conclusions

Our study provides the first quantitative compositional characterization of Caribbean plate slope cover sediments in the Pacific offshore Costa Rica, and also the sediments from the oceanic Cocos Plate are characterized.

Applying synchrotron texture analysis we could show that sediments from the incoming plate and accretionary prism are less textured than sediments from the slope due to higher smectite contents, higher porosity and resulting lower compaction rates. Compaction trends can be derived from the texture analysis. Apart from describing the compaction processes, the textures lead to the identification of faulting, folding and drag folding as well as rotated fault blocks located within the accretionary prism and slope cover sediments of the active continental margin, based on steeply inclined bedding plane orientations and girdle fabrics of phyllosilicate (001) pole figures.

## Acknowledgements

Technical support of Helmut Klein and Lars Raue in the preparation of and help during synchrotron diffraction experiments is greatly acknowledged. We also acknowledge the support of Klaus Wemmer and Volker Karius with X-ray powder measurements and analysis. Furthermore, we appreciate the beam time granted at ESRF Grenoble (ES-246) and DESY Hamburg (I-20140240) and the valuable support of the beam line scientists. The dedicated work of the JOIDES Resolution shipboard party is greatly acknowledged. The project was financially supported by the DFG projects STI 298/7-1,2 and LE 948/2-1. RK received funding by the GeoGenderChancen Fonds granted by the Faculty of Geoscience and Geography Göttingen. The experimental data used in this study is available at https://zenodo.org/record/1447081.

## References

Agar, S.M., Prior, D.J., & Behrmann, J.H., 1989. Back-scattered electron imagery of the tectonic fabrics of some fine-grained sediments: implications for fabric nomenclature and deformation processes. Geology 17, 901–904. doi:10.1346/CCMN.2006.0540411.

Antao, M., Hassan, I., Wang, J., Lee, P.L., Toby, B.H., 2008. State-of-the-art high-resolution powder X-ray diffraction (HRPXRD) illustrated with Rietveld structure refinement of quartz, sodalite, tremolite, and meionite. Can. Mineral. 46, 1501–1509. doi:10.3749/canmin.46.5.1501

Arroyo, I.G., Grevemeyer, I., Ranero, C.R., von Huene, R., 2014. Interplate seismicity at the CRISP drilling site: The 2002 Mw 6.4 Osa earthquake at the southwestern end of the Middle America Trench. Geochem. Geophys. Geosys. 15, 3035–3050. doi:10.1002/2015GC005918.

Bangs, N.L., McIntosh, K.D., Silver, E.A., Kluesner, J.W., Ranero, C.R., 2016. A recent phase of accretion along the southern Costa Rica subduction zone. Earth Planet. Sci. Lett. 443, 204–215.

Bangs, N.L., McIntosh, K.D., Silver, E.A., Kluesner, J.W., Ranero, C.R., 2015. Fluid accumulation along the Costa Rica subduction thrust and development of the seismogenic zone. J. Geophys. Res. - Solid Earth 120, 67–86. doi:10.1002/2014JB011265

Barckhausen, U., Ranero, C.R., von Huene, R., Cande, S.C., Roeser, H.A., 2001. Revised tectonic boundaries in the Cocos Plate off Costa Rica: Implications for the segmentation of the convergent margin and for plate tectonic models. J. Geophys. Res. 106, 207–220. doi:10.1029/2001JB000238

Bennett, R., Bryant, W., Keller, G., 1981. Clay fabric of selected submarine sediments: fundamental properties and models. J. Sediment. Petrol. 23, 217–232.

Bennett, R., Hulbert, M., 1986. Clay Microstructure. International Human Resources Development Corporation, Boston. pp. 161.

Bergmann, J., Friedel, P., Kleeberg, R., 1998. BGMN-A new fundamental parameters based Rietveld program for laboratory X-ray sources, its use in quantitative analysis and structure investigations. CPD Newsl. 20.

Bish, D.L., Von Dreele, R.B., 1989. Rietveld Refinement of Non-Hydrogen Atomic Positions in Kaolinite. Clays Clay Miner. 37, 289–296. doi:10.1346/CCMN.1989.0370401

Bowles, F.A., Bryant, W.R., & Wallin, C., (1969). Microstructure of unconsolidated and consolidated marine sediments. J. Sediment. Res. 39, 1546–1551.

Carson, B., von Huene, R., & Arthur, M. (1982). Small-scale deformation structures and physical properties related to convergence in Japan Trench slope sediments. Tectonics,

1(3), 277–302.

Curtis, C.D., Lipshie, S.R., Oertel, G., Pearson, M.J., 1980. Clay orientation in some Upper Carboniferous mudrocks, its relationship to quartz content and some inferences about fissility, porosity and compactional history. Sedimentology 27, 333–339.

DeMets, C., 2001. A new estimate for present-day Cocos-Caribbean plate motion: Implications for slip along the Central American volcanic arc. Geophys. Res. Lett. 28, 4043–4046. doi:10.1029/2001GL013518

Doebelin, N., Kleeberg, R., 2015. Profex: A graphical user interface for the Rietveld refinement program BGMN. J. Appl. Crystallogr. 48, 1573–1580. doi:10.1107/S1600576715014685

Downs, R.T., Hall-Wallace, M., 2003. The American Mineralogist crystal structure database. Am. Mineral. 88, 247–250.

Ghisoli, C., Caucia, F., & Marinoni, L. (2010). XRPD patterns of opals: A brief review and new results from recent studies. Powder Diffraction, 25(3), 274–282. doi:10.1154/1.3478554

Gournis, D., Lappas, A., Karakassides, M.A., Többens, D., Moukarika, A., 2008. A neutron diffraction study of alkali cation migration in montmorillonites. Phys. Chem. Miner. 35, 49–58. doi:10.1007/s00269-007-0197-z

Graf, D.L., 1961. Crystallographic tables for the rhombohedral carbonates. Am. Mineral. 46, 1283–1316.

Grazulis, S., Chateigner, D., Downs, R.T., Yokochi, A.F.T., Quirós, M., Lutterotti, L., Manakova, E., Butkus, J., Moeck, P., Le Bail, A., 2009. Crystallography Open Database - An open-access collection of crystal structures. J. Appl. Crystallogr. 42, 726–729. doi:10.1107/S0021889809016690

Gualtieri, A.F., Ferrari, S., Leoni, M., Grathoff, G., Hugo, R., Shatnawi, M., Paglia, G., Billinge, S., 2008. Structural characterization of the clay mineral illite-1M. J. Appl. Crystallogr. 41, 402–415. doi:10.1107/S0021889808004202

Harris, R.N., Sakaguchi, A., Petronotis, K., and the Expedition 344 Scientists, 2013. Proceedings IODP, 344. College Station, Texas. doi:10.2204/iodp.proc.344.2013

Hashimoto, Y., Tobin, H. and Knuth, M. (2010). Velocity-porosity relationship for slope apron and accreted sediments in the Nankai Trough Seismogenic Zone Experiment, Integrated Ocean Drilling Program Expedition 315 Site C0001. Geochem. Geophys. Geosyst., 11, Q0AD05, doi:10.1029/2010GC003217

Kameda, J., Harris, R.N., Shimizu, M., Ujiie, K., Tsutsumi, A., Ikehara, M., Uno, M., Yamaguchi, A., Hamada, Y., Namiki, Y., Kimura, G., 2015. Hydrogeological responses to incoming materials at the erosional subduction margin, offshore Osa Peninsula, Costa Rica. Geochem. Geophys. Geosys. 16, 2725–2742. doi:10.1002/2014GC005514.Received

Kanitpanyacharoen, W., Kets, F.B., Wenk, H.R., Wirth, R., 2012. Mineral preferred orientation

and microstructure in the Posidonia Shale in relation to different degrees of thermal maturity. Clays Clay Miner. 60, 315–329. doi:10.1346/CCMN.2012.0600308

Kanitpanyacharoen, W., Vasin, R., Wenk, H., Dewhurst, D.N., 2015. Linking preferred orientations to elastic anisotropy in Muderong Shale , Australia. Geophysics 80, C9–C19. doi:10.1190/GEO2014-0236.1

Kanitpanyacharoen, W., Wenk, H.R., Kets, F., Lehr, C., Wirth, R., 2011. Texture and anisotropy analysis of Qusaiba shales. Geophys. Prospect. 59, 536–556. doi:10.1111/j.1365-2478.2010.00942.x

Kawamura, K., 2011. Burial consolidation processes of deep-sea sediments: An example of core sediments collected from the Labrador Sea in the Northwest Atlantic. Soils and Foundations 50, 623–632.

Kawamura, K., Ogawa, Y., 2004. Progressive change of pelagic clay microstructure during burial process : examples from piston cores and ODP cores. Mar. Geol. 207, 131–144. doi:10.1016/j.margeo.2004.03.016

Kock, I., Huhn, K., 2007. Influence of particle shape on the frictional strength of sediments — A numerical case study. Sediment. Geol. 196, 217–233. doi:10.1016/j.sedgeo.2006.07.011

Kopf, A., 2013. Effective strength of incoming sediments and its implications for plate boundary propagation: Nankai and Costa Rica as type examples of accreting vs. erosive convergent margins. Tectonophysics 608, 958–969. doi:10.1016/j.tecto.2013.07.023

Kopf, A., Behrmann, J.H., 1997. Fabric evolution and mechanisms of diagenesis in fine-grained sediments from the Kita-Yamato Trough, Japan Sea. J. Sediment. Res. 67, 590–600.

Kurzawski, R.M., Niemeijer, A., Stipp, M., Charpentier, D., Behrmann, J.H., Spiers, C.J., 2018. Frictional properties of subduction input sediments at an erosive continental margin and related controls on décollement slip modes - the Costa Rica Seismogenesis Project (CRISP). J. Geophys. Res. - Solid Earth. doi:10.1029/2017jb015398

Kurzawski, R.M., Stipp, M., Niemeijer, A.R., Spiers, C.J., Behrmann, J.H., 2016. Earthquake nucleation in weak subducted carbonates. Nat. Geosci. 9, 717–722. doi:10.1038/ngeo2774

Lonardelli, I., Wenk, H.-R., Ren, Y., 2007. Preferred orientation and elastic anisotropy in shales. Geophysics 72, D33–D40. doi:10.1190/1.2435966

Lutterotti, L., Matthies, S., Wenk, H.-R., Schultz, A.S., Richardson, J.W., 1997. Combined texture and structure analysis of deformed limestone from time-of-flight neutron diffraction spectra. J. Appl. Phys. 81, 594–600. doi:10.1063/1.364220

Lutterotti, L., Voltolini, M., Wenk, H.R., Bandyopadhyay, K., Vanorio, T., 2010. Texture analysis

of a turbostratically disordered Ca-montmorillonite. Am. Mineral. 95, 98–103. doi:10.2138/am.2010.3238

Maffione, M., Morris, A., 2017. The onset of fabric development in deep marine sediments. Earth Planet. Sci. Lett. 474, 32–39. doi:10.1016/j.epsl.2017.06.018

Matthies, S., Vinel, G.W., 1982. On the Reproduction of the Orientation Distribution Function of Texturized Samples from Reduced Pole Figures Using the Conception of a Conditional Ghost Correction. Phys. status solidi 112, K111–K114. doi:10.1002/pssb.2221120254

Matthies, S., Wenk, H.-R., 2009. Transformations for monoclinic crystal symmetry in texture analysis. J. Appl. Crystallogr. 42, 564–571. doi:10.1107/S0021889809018172

Milliken, K. L., & Reed, R. M. (2010). Multiple causes of diagenetic fabric anisotropy in weakly consolidated mud, Nankai accretionary prism, IODP Expedition 316. J. Struct. Geol., 32, 1887- 1898.

Mondol, N.H., Bjørlykke, K., Jahren, J., Høeg, K., 2007. Experimental mechanical compaction of clay mineral aggregates — Changes in physical properties of mudstones during burial. Mar. Pet. Geol. 24, 289–311. doi:10.1016/j.marpetgeo.2007.03.006

Moon, C.F., Hurst, C.W., 1984. Fabrics of muds and shales: an overview. Geol. Soc. London Spec. Publ. 15, 579–593.

Moore, D.M., Reynolds, R.C.J., 1997. X-Ray diffraction and the identification and analysis of clay minerals. Oxford University Press, New York.

Oertel, G., (1983). The relationship of strain and preferred orientation of phyllosilicate grains in rocks — a review. In: Friedman, M., & Toksöz, M.N. (Eds.), Continental Tectonics: Structure, Kinematics and Dynamics. Tectonophysics. 100, 413–447.

Omotoso, O., Mikula, R., Urquhart, S., Sulimma, H., Stephens, P., 2006. Characterization of clays from poorly processing oil sands using synchrotron techniques. Clay Sci. 12, 88–93. doi:10.1017/CBO9781107415324.004

Protti, M., Schwartz, S.Y., 1994. Mechanics of back arc deformation in Costa Rica: Evidence from an aftershock study of the April 22, 1991, Valle de la Estrella, Costa Rica, earthquake (Mw=7.7). Tectonics 13, 1093–1107.

Ranero, C.R., von Huene, R., 2000. Subduction erosion along the Middle America convergent margin. Nature 404, 748–752. doi:10.1038/35008046

Rietveld, H.M., 1969. A profile refinement method for nuclear and magnetic structures. J. Appl. Crystallogr. 2, 65–71. doi:10.1107/S0021889869006558

Schumann, K., Stipp, M., Leiss, B., Behrmann, J.H., 2014. Texture development in naturally compacted and experimentally deformed silty clay sediments from the Nankai Trench and Forearc, Japan. Tectonophysics 636, 125–142. doi:10.1016/j.tecto.2014.08.005

Sintubin, M., 1994. Clay fabrics in relation to the burial history of shales. Sedimentology 41,

1161–1169.

Spinelli, G.A., Underwood, M.B., 2004. Character of sediments entering the Costa Rica subduction zone : Implications for partitioning of water along the plate interface. Isl. Arc 13, 432–451.

Środoń, J., Drits, V.A., McCarty, D.K., Hsieh, J.C.C., Eberl, D.D., 2001. Quantitative X-ray diffraction analysis of clay-bearing rocks from random preparations. Clays Clay Miner. 49, 514–528. doi:10.1346/CCMN.2001.0490604

Stipp, M., Rolfs, M., Kitamura, Y., Behrmann, J.H., Schumann, K., Schulte-Kortnack, D. and Feeser, V. (2013). Strong sediments at the deformation front, and weak sediments at the rear of the Nankai accretionary prism, revealed by triaxial deformation experiments. Geochem. Geophys. Geosys. 14/11, doi: 10.1002/ggge.20290.

Vannucchi, P., Morgan, J.P., Silver, E.A., Kluesner, J.W., 2016. Origin and dynamics of depositionary subduction margins. Geochem. Geophys. Geosys. 17, 1966–1974. doi:10.1002/ 2016GC006259

Vannucchi, P., Ranero, C.R., Galeotti, S., Straub, S.M., Scholl, D.W., McDougall-Reid, K., 2003. Fast rates of subduction erosion along the Costa Rica Pacific margin: Implications for nonsteady rates of crustal recycling at subduction zones. J. Geophys. Res. 108, 1–13. doi:10.1029/2002JB002207

Vannucchi, P., Scholl, D.W., Meschede, M., McDougall-Reid, K., 2001. Tectonic erosion and consequent collapse of the Pacific margin of Costa Rica: Combined implications from ODP Leg 170, seismic offshore data, and regional geology of the Nicoya Peninsula. Tectonics 20, 649–668.

Vannucchi, P., Ujiie, K., Stroncik, N., Malinverno, A., and the Expedition 334 Scientists, 2012. Expedition 334 summary. Proc. Integr. Ocean Drill. Progr. 334. College Station, Texas. doi:10.2204/iodp.proc.334.101.2012

Vasin, R.N., Wenk, H.R., Kanitpanyacharoen, W., Matthies, S., Wirth, R., 2013. Elastic anisotropy modeling of Kimmeridge shale. J. Geophys. Res. Solid Earth 118, 3931–3956. doi:10.1002/jgrb.50259

Voltolini, M., Wenk, H.-R., Mondol, N.H., Bjorlykke, K., Jahren, J., 2009. Anisotropy of experimentally compressed kaolinite-illite-quartz mixtures. Geophysics 74, D13–D23. doi:10.1190/1.3002557

von Huene, R., Ranero, C.R., Vannucchi, P., 2004. Generic model of subduction erosion. Geology 32, 913–916. doi:10.1130/G20563.1

von Huene, R., Ranero, C.R., Weinrebe, W., Hinz, K., 2000. Quaternary convergent margin tectonics of Costa Rica, segmentation of the Cocos Plate, and Central American volcanism. Tectonics 19, 314–334. doi:10.1029/1999TC001143

von Huene, R., Scholl, D.W., 1991. Observations at convergent margins concerning sediment subduction, subduction erosion, and the growth of continental crust. Rev. Geophys. 29, 279–316.

Wainwright, J.E., Starkey, J., 1971. A refinement of the structure of anorthite. Zeitschrift für Krist. 133, 75–84.

Wenk, H.-R., Kanitpanyacharoen, W., Voltolini, M., 2010. Preferred orientation of phyllosilicates: Comparison of fault gouge, shale and schist. J. Struct. Geol. 32, 478–489. doi:10.1016/j.jsg.2010.02.003

Wenk, H.-R., Lonardelli, I., Franz, H., Nihei, K., Nakagawa, S., 2007. Preferred orientation and elastic anisotropy of illite-rich shale. Geophysics 72, E69–E75. doi:10.1190/1.2432263

Wenk, H.-R., Voltolini, M., Kern, H., Popp, T., Mazurek, M., 2008a. Anisotropy in shale from Mont Terri. Lead. Edge 27, 742. doi:10.1190/1.2944161

Wenk, H.-R., Voltolini, M., Mazurek, M., Van Loon, L.R., Vinsot, A., 2008b. Preferred Orientations and Anisotropy in Shales: Callovo-Oxfordian Shale (France) and Opalinus Clay (Switzerland). Clays Clay Miner. 56, 285–306. doi:10.1346/CCMN.2008.0560301

Yue, H., Lay, T., Schwartz, S.Y., Rivera, L., Protti, M., Dixon, T.H., Owen, S., Newman, A. V, 2013. The 5 September 2012 Nicoya , Costa Rica Mw 7.6 earthquake rupture process from joint inversion of high-rate GPS, strong-motion, and teleseismic P wave data and its relationship to adjacent plate boundary interface properties. J. Geophys. Res. Solid Earth 118, 5453–5466. doi:10.1002/jgrb.50379

# 5. Textures in oceanic serpentinites from the Atlantis Massif, Mid-Atlantic Ridge

## Abstract

Oceanic serpentinites are mainly composed of the serpentine minerals lizardite and chrysotile. For the challenging analysis of the crystallographic preferred orientations (CPO, texture) of such mineral phases, we applied high-energy synchrotron diffraction.

A suite of serpentinite samples was cored during the International Ocean Discovery Program Expedition 357 at the Atlantis Massif oceanic core complex, located on the mid-Atlantic ridge at ~30°N. Samples are highly altered ultramafics, containing lizardite and chrysotile, as well as magnetite and further minor minerals. The microstructure varies from weakly foliated bastite-rich to bastite-free mesh structures. Serpentine CPOs in bastite-rich samples are dominated by bastites, while in bastite-poor samples the CPO seems to be controlled by the serpentinizing microfractures. The variations could depict differences in strain, in primary composition or fabrics inherited from the peridotite. Even though the CPO in the samples originates from different microfabrics, it leads to global texture with resulting anisotropic physical properties.

## 5.1. Introduction

Serpentinites are of great importance in plate tectonic processes. They occur at slow spreading ridges as well as in hydrated wedges in subduction zones. Serpentinization changes i.a. the rheology (Escartín et al., 2001) and the physical properties (Miller and Christensen, 1997) compared to the precursor rocks.

Serpentinite forms from peridotite and ultramafic rocks by hydration of olivine and pyroxene. Pseudomorphic alteration of olivine leads to the formation of a mesh microstructure. Serpentinization starts at fractures and grain boundaries forming mesh rims of serpentine (Wicks and Whittaker, 1977), typically traced by magnetite. Mesh rim growth can either progress up to the center of the grain (hourglass structure) or be followed by a mesh core which might still comprise olivine, or is completely serpentinized lacking an optically differentiable microstructure (Viti and Mellini, 1998; Wicks and Whittaker, 1977). Pseudomorphic alteration of pyroxene leads to the formation of bastites, fine-grained serpentinized regions. Different formation temperatures lead to the crystallization of different serpentine minerals. Lizardite, the flat stacked polymorph, and chrysotile, the fibrous polymorph, form at temperatures <300-400°C (Evans, 2004). Antigorite in contrast, which has a wavy crystal structure and is not a polymorph *sensu strictu* as it contains less water can be stable from 300 °C up to 720 °C at P=2 GPa (Ulmer and Trommsdorff, 1995). Whether

chrysotile or lizardite is formed is most likely determined by stress mode under which they form (Evans, 2004).

Serpentine crystallites in oceanic low-temperature serpentinites are often considered randomly oriented (e.g. Christensen, 2004). Therefore seismic velocities and anisotropies are often seen only as a function of the serpentinized volume fraction of the sample (Christensen, 2004; Ji et al., 2013), where increasing volume fraction of serpentine leads to a reduction of P-wave velocity from ~8 km/s to ~5 km/s (Miller and Christensen, 1997). Due to the irregular crystal structure it can be challenging to determine the crystallographic preferred orientation (=texture) of serpentinites, especially when including chrysotile. Most conventional texture analysis methods reach their limits. Electron backscatter diffraction (EBSD) requires highly polished crystal surfaces, which is impossible for the non-planar polymorphs, and neutron texture measurements can be hampered by the high amount of intracrystalline water incorporated in the serpentine minerals. A method suitable for these challenging samples is synchrotron diffraction as it is not demanding high preparation efforts and no absorption takes place by intracrystalline water. While textures of antigorite bearing serpentinites (often highly deformed) have been subject of a number of studies (e.g. Bezacier et al., 2010; Kern et al., 2015, 1997), the oceanic serpentinites have been more rarely explored (Lizardite: Boudier et al., 2010; Dewandel et al., 2003).

The texture of oceanic serpentinites is of major importance as it influences the geophysical properties. Large-scale anisotropies could change the interpretation of seismological models and thus enhance our ideas of the build-up of the oceanic crust. We therefore analyze serpentinite samples from the Atlantis Massif at the mid-Atlantic ridge regarding their texture using synchrotron diffraction. In combination with microstructural analyses we investigate the texture forming processes which contrast previous assumptions.

## 5.2. Geological setting and samples

We examined fresh oceanic serpentinites from the Atlantis Massif, located at 30°N at the Mid-Atlantic Ridge (MAR). The Atlantis Massif is a 1.5 – 2 m.y. old (Blackman et al., 2002, 1998), domal structure which is southerly bounded by the Atlantis Transform Fault and to the East by the MAR median valley (Figure 5.1).

The Atlantis Massif is an oceanic core complex (OCC), where upper mantle peridotites and gabbroic rocks are exhumed along a large scale detachment fault (e.g. Blackman et al., 1998; Cann et al., 1997; Tucholke and Lin, 1994; Tucholke et al., 1998). Faulting is thought to happen due to episodic and insufficient magma supply at slow spreading ridges, which cannot counterbalance the spreading velocity. The massif can be roughly subdivided in the central dome, where a large gabbroic body was discovered during IODP Expedition 305 drilling (Blackman et al., 2006; Ildefonse et al., 2007), an eastern hanging block formed by basalts

(Blackman et al., 2002), and the southern wall which is to large extent (45%) altered to serpentinite and which hosts the Lost City hydrothermal field (Früh-Green et al., 2018). Seismological modelling shows a higher p-wave velocity in the eastern part of the southern wall, indicating a change in lithology (Henig et al., 2012).

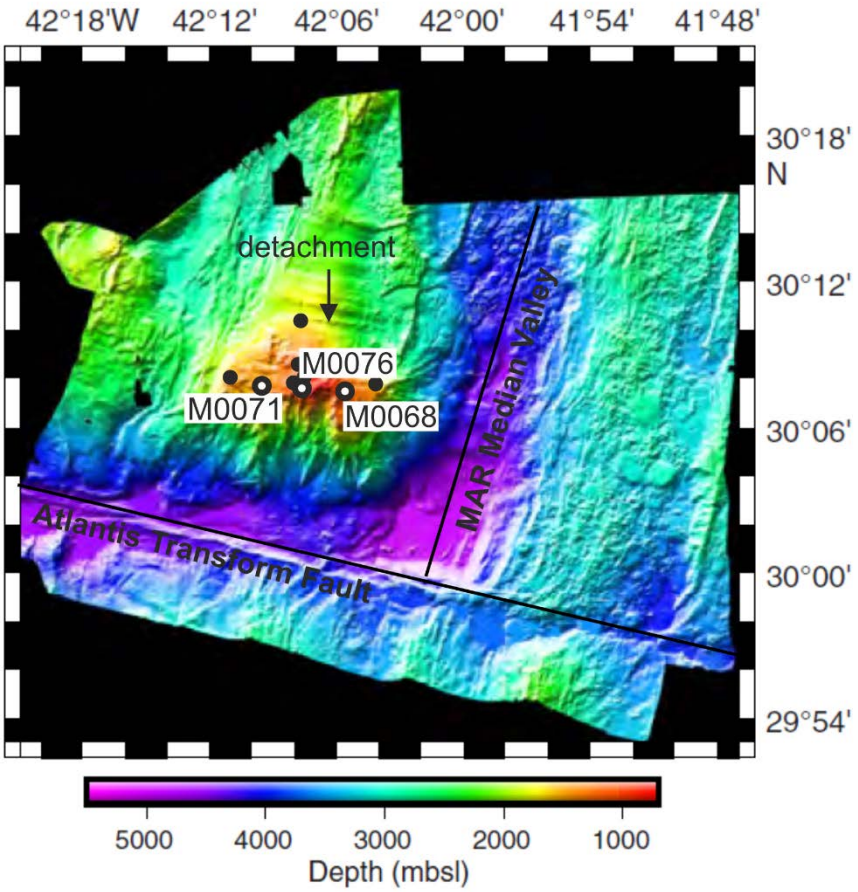


*Figure 5.1. Bathymetric map of the Atlantis Massif Oceanic Core Complex. Black circles mark drill locations from where samples were used in this study. Black dots mark other locations drilled during IODP Expedition 357. Modified from Früh-Green et al. 2017.*

During IODP Expedition 357, which explored the "Atlantis Massif Serpentinization and Life", shallow cores (maximum depth: 16.5 m) were drilled at nine sites along the top of the southern wall of the massif. The rock types discovered range from sediments over basalts to serpentinized peridotites, talc-amphibole-chlorite schists and gabbros (Früh-Green et al., 2018, 2017). Serpentinite was reported to be very heterogeneous in microstructure (Rouméjon et al., 2018).

We present texture data of four serpentinite samples from the drill cores M0068, M0071 & M0076, which were chosen due to their composition of serpentine and magnetite. Here and in the following we use an abbreviated sample name, the complete sample names including

depth and section can be found in Table 1. Two samples (71C3R1&71C9R1) originate from a drill core located in the western part of the southern wall of Atlantis Massif (Figure 5.1). Their macroscopic structure shows large (up to 1 cm) bastites. Another sample is from the central part of the southern wall (76B5R1), displaying multiple white veins in macroscopic section. The last sample originates from a drill hole further east on the southern wall (68B4R1). It is a dark rock with white and green veins.

*Table 5.1. Samples used in this study*

| Sample (Drill site +section) | Interval [cm] | Depth below seafloor [m] | Petrographic description from Früh-Green et al. (2017) |
|---|---|---|---|
| 71C3R1 | 24-28 | 5.2 | Serpentinized harzburgite |
| 71C9R1 | 34-38 | 10 | Serpentinized harzburgite |
| 76B5R1 | 63-67 | 7.4 | Serpentinized harzburgite |
| 68B4R1 | 87-90 | 4.9 | Serpentinized harzburgite |

## 5.3. Method

### 5.3.1. Microstructure

Thin sections were produced from the samples and analyzed using a polarizing microscope with an accessory plate inducing a wave difference of 550 nm.

### 5.3.2. Synchrotron texture measurements

Synchrotron texture measurements were conducted at the European Synchrotron Radiation Facility (ESRF) in Grenoble, France. Samples are cylinder shaped with a diameter of 1.5 to 2 cm. Measurements were carried out in transmission mode while rotating the sample about the cylinder axis from 0° to 175° in 5° steps with 1 s overall exposure time. As we used a Perkin Elmer image plate detector, this results in 36 images per measured sample position. Due to relatively large grain sizes of the samples, we measured several positions along the cylinder axis of the samples. Beam size was set to ~1 mm and wavelength to 70 keV. Sample-detector distance was 1401 mm.

### 5.3.3. Texture data analysis

The image data is transferred into *.tif images using the program Fit2D (Hammersley, 1998), which also allows the determination of the beam center.

Data treatment and analysis is conducted using the Rietveld program MAUD (Material Analysis Using Diffraction) (Lutterotti et al., 1997). As input lattice parameters the following cif-files from the AMCDS (Downs and Hall-Wallace, 2003) and COD (Grazulis et al., 2009) data bases are used: chrysotile from a powder containing nano-tubes by Falini et al. (2004), a lizardite 1T by

Laurora et al. (2011), magnesioferrite (Passerini, 1930) and magnetite (Gatta et al., 2007). First an average image is analyzed, and background and scale factors, instrumental parameters and crystal lattice parameters are refined. Then the images for every single measurement position are loaded and the texture is calculated using the EWIMV algorithm (derived from WIMV by (Matthies and Vinel, 1982)).

## 5.4. Results

### 5.4.1. Microstructure

Sample 71C9R1 (Figure 5.2a&b) shows large (>1 cm) altered bastitic clasts, which can still show the original cleavage or exhibit zonation. Some clasts are not completely altered but can still have some pyroxenic areas. The bastites are embedded in a mesh structure of mostly random oriented serpentinizing microfractures decorated with magnetite, with a width of up to 30 µm. Mesh rims can be feathery and can have isotropic mesh cores. Hourglass structures can also be observed. Other mesh cores are more isotropic. The density of serpentinizing microfractures can increase towards the embedded bastites. Foliation is hard to discover but there seems to be a predominant orientation in which more serpentinizing microfractures are oriented than in other directions. Additionally, late, rather parallel serpentine veins crosscut the mesh fabric.

Also in sample 71C3R1 (Figure 5.2c&d) large elongated bastite clasts (~ 1cm length) can be recognized, in some of them the original pyroxene cleavage can be visible. Serpentinizing microfractures are often oriented parallel, defining a foliation. They anastomose around the bastites, some of which are elongated and oriented parallel to the foliation. The mesh rims are diffuse and the amount of oriented feathery serpentine is less extensive, compared to sample 71C9R1. The mesh cells show some rare hourglass structures as well as some clearly visible cores, while the rest is more diffuse.

In sample 76B5R1 (Figure 5.2e&f) some rare, rather small (up to 300 µm) unaltered relic pyroxenes can be recognized. There is a strong parallel orientation of serpentinizing microfractures, which can be fairly broad (~50 µm), forming the foliation. The mesh rims look like perpendicular fibers. Veins of magnetite, serpentine, calcite, and talc crosscut the fabric perpendicular to the foliation. Mesh rims at microfractures with roughly the same serpentine orientation reveal the same orientation in some areas when the accessory plate is used.

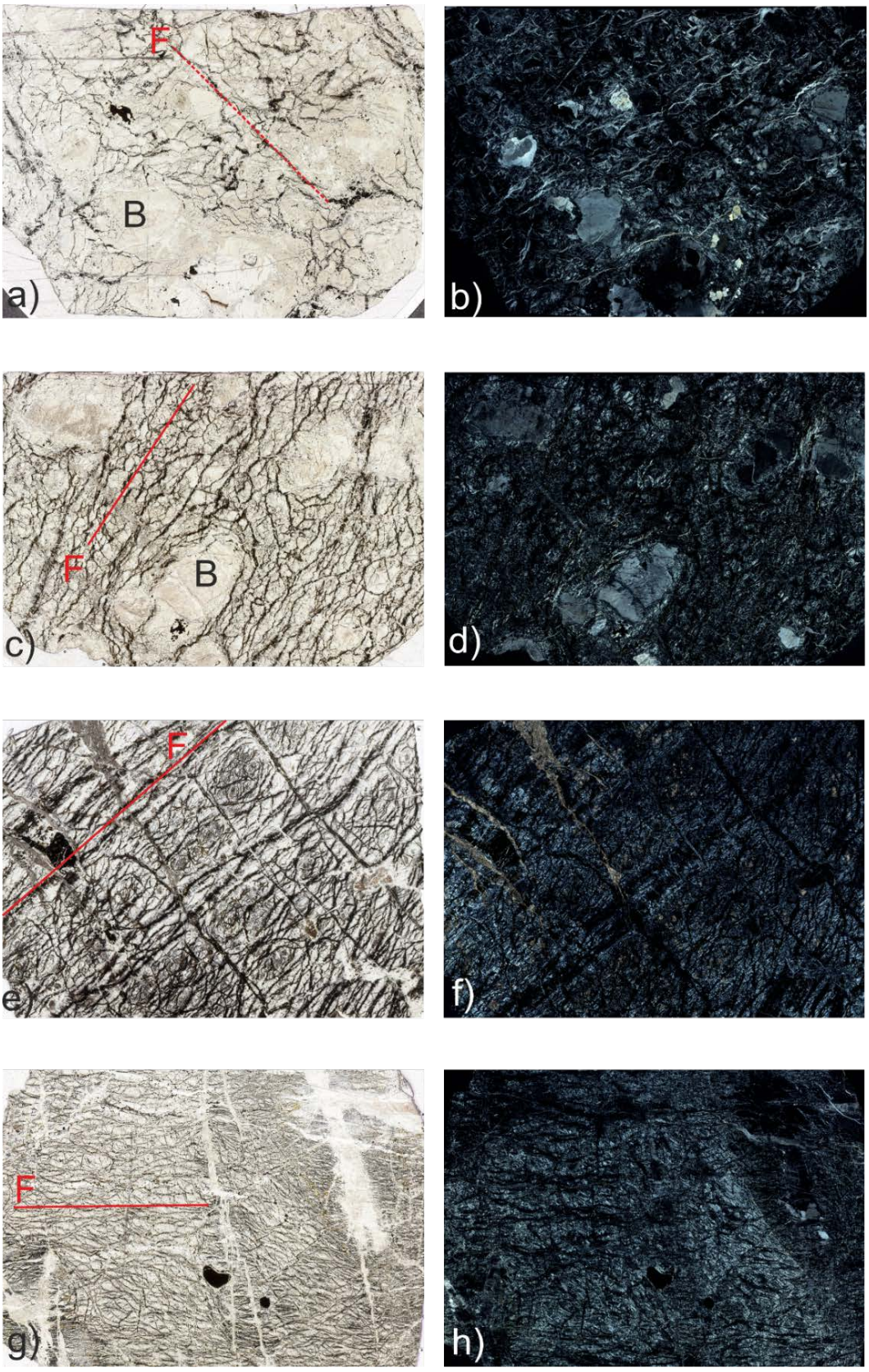


*Figure 5.2. Thin section scans of the samples a) 71C9R1 in parallel light b) same section as a) with crossed polars c) sample 71C3R1 in parallel light d) same as c) with crossed polars; e) sample 75B6R1 in parallel light f) same as e) with crossed polars g) sample 68B4R1 in parallel light h) same section as g) with crossed polars. Orientation of the foliation is indicated by red line (F). B: Bastite.*

In sample 68B4R1 (Figure 5.2g&h) no bastites or relicts can be recognized. There is a strong and closely spaced parallel alignment of serpentinizing microfractures in at least two directions, which define in combination a foliation and build a ribbon-shaped microstructure. Some microfractures are pure magnetite and some are magnetite at the rims and serpentine in the microfracture centre. The magnetite veins are thinner than in the samples described before (~10 µm). The mesh centers can reveal isotropic cores. The serpentine orientation is colorcoded by the orientation of the microfractures when using the accessory plate. One family of parallel microfractures turns out yellow, and the other one blue. Large serpentine veins crosscut the fabric, with a higher microfracture density around them.

### 5.4.2. Texture results

In sample 71C9R1 (Figure 5.3a) chrysotile (002) pole figure shows a single maximum with a maximum intensity of 1.7 mrd. The same maximum orientation is shown by the lizardite (001) pole figure, but smaller and sharper with a maximum intensity of 3.4 mrd (multiples of random distribution). The (00l) maxima of both serpentine minerals are inclined ~35° from the foliation plane. The magnetite shows no preferred orientation (maximum pole figure intensity: 1.1 mrd). The chrysotile (002) in sample 71C3R1 (Figure 5.3b) only shows a weak preferred orientation with a girdle inclined from the foliation plane with a pole figure maximum of 1.2 mrd. However, the lizardite (001) pole figure shows a small distinct maximum with a maximum intensity of 2.0 mrd. The magnetite pole figures do not show a texture (maximum intensity 1.2 mrd).

In sample 76B5R1 (Figure 5.3c) the chrysotile (002) pole figure shows a broad main maximum, which is inclined from the normal to the foliation but parallel to the core axis. The maximum intensity is 1.6 mrd. The lizardite (001) pole figure shows two maxima in about the same orientation as the chrysotile (002) submaxima. The maximum intensity is 1.7 mrd. All submaxima are inclined from the foliation plane. The magnetite pole figures show clear distinct symmetric maxima with a maximum intensity of 2.6 mrd.

The chrysotile (002) maximum in sample 68B4R1 (Figure 5.3d) shows a broader single maximum with a maximum intensity of 2.4 mrd. The same pattern is presented by the lizardite (001) pole figure, which is even broader than the chrysotile (002) maximum and with a stronger maximum intensity of 3.7 mrd. Both serpentine (00l) maxima lie perpendicular to the foliation. The magnetite pole figures show very clear distinct symmetric maxima with a maximum intensity of 5.1 mrd.

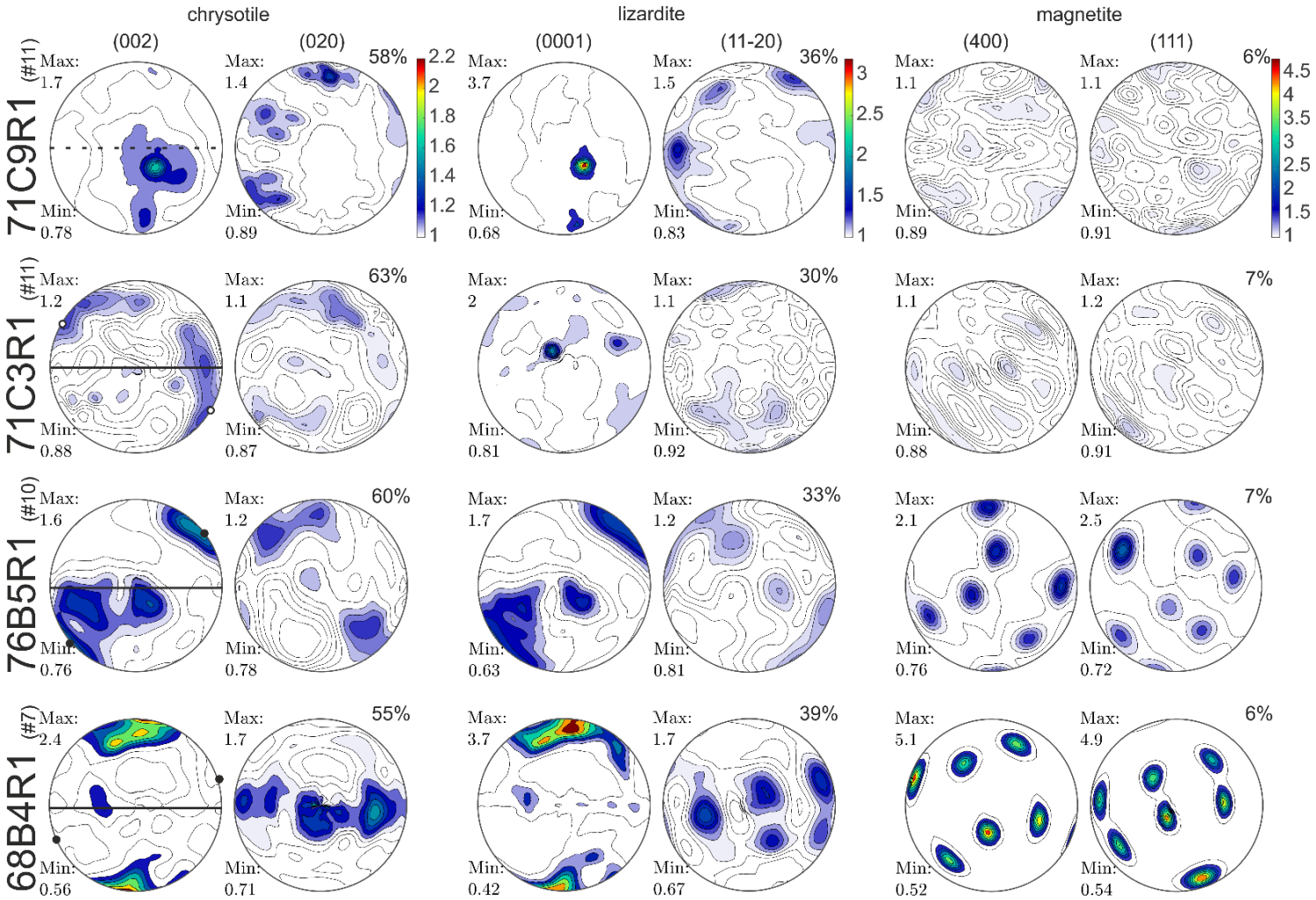


*Figure 5.3. Recalculated pole figures for chrysotile, lizardite and magnetite. Equal area, lower hemisphere projection. Maxima in mrd (multiples of random distribution). Orientation is given in the first pole figure for each sample: foliation is given as solid line, "hard to determine"-foliation is given as dashed line. Reference to the drill core axis is given by solid dots, circles are used for samples which are rubble, where core axis orientation is useless. In sample 71C9R1 the orientation of the piece of rubble to the core axis could not be reconstructed. The number of measured slices for each sample is given in brackets behind the sample name. Pole figures are projected in the same plane as the thin sections in Fig. 2.*

## 5.5. Discussion

### 5.5.1. Quality of the texture analysis

Using synchrotron diffraction for the texture analysis of oceanic serpentinite samples was very successful. We could extract lizardite and chrysotile textures by using Rietveld refinement. As both minerals have, beside their shared peaks, some peaks separated from each other it is possible to determine the texture by using the full spectra. However, we have to consider that our samples probably rank at the upper range of measurable samples regarding grain size. We compensated this by measuring several slices per samples which enhances the statistics. Our compositional results from Rietveld texture refinement show a higher amount of chrysotile than lizardite. This is in contrast to all observations, which state that lizardite is the most important serpentine mineral in oceanic serpentinites (e.g. Evans, 2004). It might be possible, that our samples are mineralogically different compared to all the other samples in the literature. As this case seems to be unlikely, we assume that the determination of the modal composition from textured rock samples with serpentine was not successful. As the composition does not affect the texture determination, we are still confident in our texture results.

### 5.5.2. Texture development

A direct link between serpentine texture and microstructure is unequivocally proven with our analytical approach, and the combination of the results of these analyses indicates how the observed texture is formed.

The sharp maxima in the serpentine texture in samples 71C9R1 and 71C3R1 are a result of bastite formation and oriented growth of serpentine in the host minerals. In sample 71C9R1 both serpentine minerals show the same sharp single maximum in the (00l) pole figure, while it is only lizardite in sample 71C3R1. This indicates that in the first sample both minerals are involved in the bastite formation, while it is only lizardite in the latter. While it is more commonly observed that lizardite forms bastites, it has also been described that chrysotile can be involved (Viti and Mellini, 1998; Wicks et al., 1977). The comparably low maxima might be a result of poor crystallization of bastites, as described by Viti and Mellini (1998). The “background texture” besides the bastites is very weak to non-existent. Even though the CPO generated by bastites is very local, we can interpolate that an inherited CPO of pyroxenes could lead to a pronounced more regional texture.

In samples 76B5R1 and 68B4R1 the broad, more intense maxima in the serpentine (00l) pole figures, are a result of strongly oriented serpentinizing microfractures and the accompanying perpendicular oriented feathery serpentine in the mesh rims. This has already been described by e.g. Rouméjon and Cannat (2014). Some studies (e.g. Boudier et al., 2010; Viti and Mellini,

1998) observed a parallel orientation of lizardite (001) plains parallel to the serpentine/olivine interface, i.e. parallel to the serpentinizing microfracture, which is stacked to columns appearing fibrous in optical microscopy. As we observed fibrous serpentine perpendicular to the serpentinizing microfractures this is most likely the source of texture in samples 68B4R1 and 76B5R1. In 76B5R1 it is inclined from the foliation normal, maybe due to local heterogeneities in foliation orientation. The serpentinizing microfractures show a clear parallel orientation, which leads to texture formation. A variety of studies considered the formation of serpentinizing microfractures (e.g. Malvoisin et al., 2017; Plümper et al., 2012; Rouméjon and Cannat, 2014; Wicks, 1984a, 1984b, 1984c), indicating that a strong preferred orientation of serpentinizing microfractures is a result of strain of the precursor olivine grains (Wicks, 1984c) or accommodate the volume increase (Rouméjon et al., 2018). This indicates that the texture in these samples is induced by deformation, either by external former or contemporaneous strain, or by internal strain generated by volume increase during serpentinization.

In all our samples the pole figures of chrysotile and lizardite appear very similar. Considering the different crystallographic structure of the two minerals, curly fibers and platy stacks, this is at least remarkable. It indicates that the chrysotile fibers are oriented in a plane which is parallel to the lizardite basal planes.

The strong magnetite texture observable in samples 76B5R1 and 68B4R1 is striking. Wicks and Whittaker (1977) mentioned, that the magnetite grains form primarily distributed within the mesh cells and then migrate towards clusters or fractures. If the migration happens within an external stress field, this could lead to a preferred orientation of the magnetite grains within the microfractures. This emphasizes the deformation-related texture formation in these samples.

### 5.5.3. Implications

As physical properties of single crystals can be highly dependent on crystallography, texture in a rock can lead to anisotropic p-wave velocities, which is of major importance for seismological models. We therefore calculated the texture-controlled Vp anisotropy from intrinsic elastic tensors for the minerals using the Matlab toolbox Mtex (Hielscher and Schaeben, 2008) following the method described by Mainprice et al., (2011). We used the elastic stiffness tensor for lizardite from Auzende et al. (2006), which was modified to be also used for chrysotile. The modeled Vp anisotropy varies over a large range from 1.1 to 8.2% (Figure 5.4). Bastite-controlled textures have lower anisotropies than microfracture controlled textures. The latter are therefore of higher importance for the interpretation of seismological models. Nevertheless, it has to be considered that the modeling does not take into account structural features as fractures, voids, etc., but may give an idea of anisotropy in serpentinites at depth, assuming closed fractures. In sample 68B4R1 with direction of fast Vp anisotropy parallel to the fractures, the foliation might further increase the anisotropy.

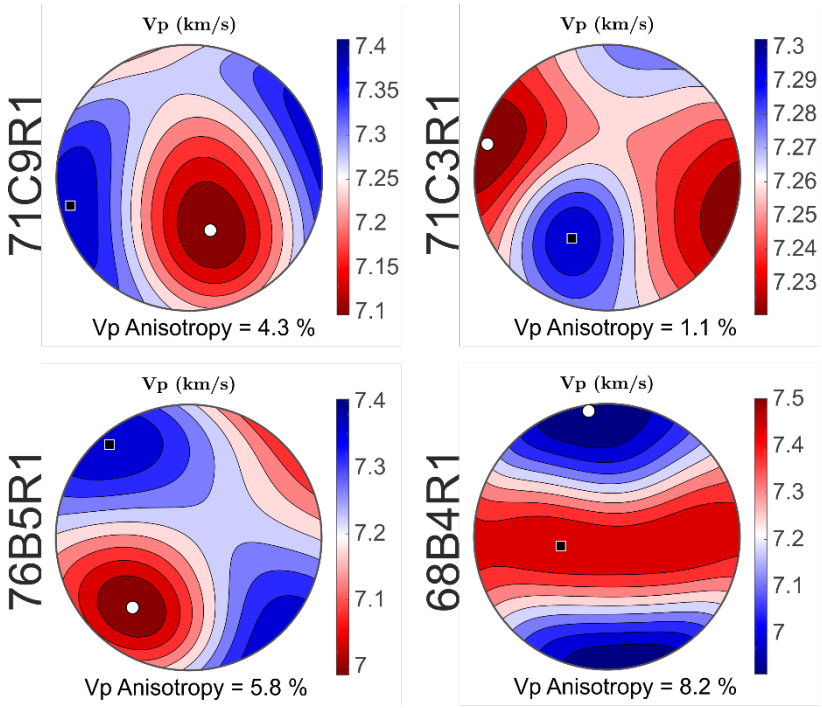


*Figure 5.4. Modeled Vp anisotropy for the samples in this study. Orientation corresponds to pole figures in Figure 3. Square: fast p-wave direction. Circle: slow p-wave direction.*

Texture intensity and thus anisotropy increase towards the detachment shear zone and the mid-Atlantic ridge. This might either reflect a change in precursor lithology from more pyroxene-rich to pyroxene-free or an increase in deformation towards the shear zone, or a combination of both. Regarding the seismological modeling of the southern wall of the Atlantis Massif (Henig et al., 2012) which showed higher velocities in the eastern part of the southern wall, the reason might be more likely the anisotropy formed by the deformation or slight changes in precursor mineralogy than a lithological change from serpentinite to gabbro.

## 5.6. Conclusion

Our study for the first time reports bulk rock quantitative textures of oceanic serpentinites. Synchrotron diffraction in combination with Rietveld refinement allowed to determine the textures. This overcomes the severe limitations posed by other texture analysis methods, and opens the possibility of quantitative modeling of physical properties of hydrated oceanic earth´s mantle.

Texture in our serpentinite samples is either generated by bastite formation or induced by pre- or syn-serpentinization deformation, as documented by preferred parallel orientation of microfractures. The latter one leads to strong seismic anisotropies, which vary in our samples between 5.8 – 8.2 % AVp. It is probably of more pervasive scale and therefore of higher importance for the interpretation of seismological models.

## Acknowledgements

We gratefully acknowledge the work of the IODP Expedition 357 scientific group. We are thankful for the great support of Andy Fitch and his group at ESRF ID22. This study was funded by DFG project BE 1041/34-1.

## References

Auzende, A.L., Pellenq, R.J.M., Devouard, B., Baronnet, A., Grauby, O., 2006. Atomistic calculations of structural and elastic properties of serpentine minerals: the case of lizardite. Phys. Chem. Miner. 33, 266–275.

Bezacier, L., Reynard, B., Bass, J.D., Sanchez-Valle, C., Van De Moortèle, B., 2010. Elasticity of antigorite, seismic detection of serpentinites, and anisotropy in subduction zones. Earth Planet. Sci. Lett. 289, 198–208. doi:10.1016/j.epsl.2009.11.009

Blackman, D.K., Cann, J.R., Janssen, B., Smith, D.K., 1998. Origin of extensional core complexes : Evidence from the Mid-Atlantic Ridge at Atlantis Fracture Zone. J. Geophys. Res. 103, 21315–21333. doi:10.1029/98JB01756

Blackman, D.K., Ildefonse, B., John, B.E., Ohara, Y., Miller, D.J., MacLeod, C.J., and the Expedition 304/305 Scientists, 2006. Proceedings of the Integrated Ocean Drilling Program Volume 304/305. College Station, Texas.

Blackman, D.K., Karson, J.A., Kelley, D.S., Cann, J.R., Früh-Green, G.L., Gee, J.S., Hurst, S.D., John, B.E., Morgan, J., Nooner, Scott, L., Ross, D.K., Schroeder, T.J., Williams, E.A., 2002. Geology of the Atlantis Massif (Mid-Atlantic Ridge, 30° N): Implications for the evolution of an ultramafic oceanic core complex. Mar. Geophys. Res. 23, 443–469. doi:10.1023/B:MARI.0000018232.14085.75

Boudier, F., Baronnet, A., Mainprice, D., 2010. Serpentine Mineral Replacements of Natural Olivine and their Seismic Implications: Oceanic Lizardite versus Subduction-Related Antigorite. J. Petrol. 51, 495–512. doi:10.1093/petrology/egp049

Cann, J.R., Blackman, D.K., Smith, D.K., McAllister, E., Janssen, B., Mello, S., Avgerinos, E., Pascoe, A.R., Escartin, J., 1997. Corrugated slip surfaces formed at ridge-transform intersections on the Mid-Atlantic ridge. Nature 385, 329–332. doi:10.1038/385329a0

Christensen, N.I., 2004. Serpentinites, Peridotites, and Seismology. Int. Geol. Rev. 46, 795–816. doi:10.2747/0020-6814.46.9.795

Dewandel, B., Boudier, F., Kern, H., Warsi, W., Mainprice, D., 2003. Seismic wave velocity and anisotropy of serpentinized peridotite in the Oman ophiolite. Tectonophysics 370, 77–94. doi:10.1016/S0040-1951(03)00178-1

Downs, R.T., Hall-Wallace, M., 2003. The American Mineralogist crystal structure database. Am. Mineral. 88, 247–250.

Escartín, J., Hirth, G., Evans, B., 2001. Strength of slightly serpentinized peridotites :

Implications for the tectonics of oceanic lithosphere. Geology 29, 1023–1026. doi:10.1130/0091-7613(2001)029<1023:SOSSPI>2.0.CO;2

Evans, B.W., 2004. The serpentinite multisystem revisited: chrysotile is metastable. Int. Geol. Rev. 46, 479–506. doi:10.2747/0020-6814.46.6.479

Falini, G., Foresti, E., Gazzano, M., Gualtieri, A.F., Leoni, M., Lesci, I.G., Roveri, N., 2004. Tubular-Shaped Stoichiometric Chrysotile Nanochrystals. Chem. A Eur. J. 10, 3043–3049. doi:10.1002/chem.200305685

Früh-Green, G.L., Orcutt, B.N., Green, S.L., Cotterill, C., Scientists, and the E. 357, 2017. Proceedings of the International Ocean Discovery Program Volume 357 Atlantis Massif Serpentinization and Life. College Station, Texas.

Früh-Green, G.L., Orcutt, B.N., Rouméjon, S., Lilley, M.D., Morono, Y., Cotterill, C., Green, S., Escartín, J., John, B.E., McCaig, A.M., et al., 2018. Magmatism, serpentinization and life: Insights through drilling the Atlantis Massif (IODP Expedition 357). Lithos 323, 137–155. doi:10.1016/j.lithos.2018.09.012

Gatta, G.D., Kantor, I., Ballaran, T.B., Dubrovinsky, L., McCammon, C., 2007. Effect of non-hydrostatic conditions on the elastic behaviour of magnetite: an in situ single crystal X-ray diffraction study. Phys. Chem. Miner. 34, 627–635. doi:10.1007/s00269-007-0177-3

Grazulis, S., Chateigner, D., Downs, R.T., Yokochi, A.F.T., Quirós, M., Lutterotti, L., Manakova, E., Butkus, J., Moeck, P., Le Bail, A., 2009. Crystallography Open Database - An open-access collection of crystal structures. J. Appl. Crystallogr. 42, 726–729. doi:10.1107/S0021889809016690

Hammersley, A.P., 1998. FIT2D V9.129 Reference Manual V3.1. Inter Rep ESRF98HA01. Grenoble.

Henig, A.S., Blackman, D.K., Harding, A.J., Kent, G.M., 2012. Downward continued multichannel seismic refraction analysis of Atlantis Massif oceanic core complex, 30°N, Mid-Atlantic Ridge 13, 1–25. doi:10.1029/2012GC004059

Hielscher, R., Schaeben, H., 2008. A novel pole figure inversion method: specification of the MTEX algorithm. J. Appl. Crystallogr. 41, 1024–1037. doi:10.1107/S0021889808030112

Ildefonse, B., Blackman, D.K., John, B.E., Ohara, Y., Miller, D.J., MacLeod, C.J., 2007. Oceanic core complexes and crustal accretion at slow-spreading ridges. Geology 35, 623–626. doi:10.1130/G23531A.1

Ji, S., Li, A., Wang, Q., Long, C., Wang, H., Marcotte, D., Salisbury, M., 2013. Seismic velocities, anisotropy, and shear-wave splitting of antigorite serpentinites and tectonic implications for subduction zones 118, 1015–1037. doi:10.1002/jgrb.50110

Kern, H., Liu, B., Popp, T., 1997. Relationship between anisotropy of P and S wave velocities and anisotropy of attenuation in serpentinite and amphibolite. J. Geophys. Res. 102,

3051–3065.

Kern, H., Lokajicek, T., Svitek, T., Wenk, H., 2015. Seismic anisotropy of serpentinite from Val Malenco, Italy. J. Geophys. Res. Earth 120, 4113–4129. doi:10.1002/2015JB012030

Laurora, A., Brigatti, M.F., Malferrari, D., Galli, E., Rossi, A., Ferrari, M., 2011. The crystal chemistry of Lizardite-1T from northern Apennines ophiolites near Modena, Italy. Can. Mineral. 49, 1045–1054. doi:10.3749/canmin.49.4.1045

Lutterotti, L., Matthies, S., Wenk, H.-R., Schultz, A.S., Richardson, J.W., 1997. Combined texture and structure analysis of deformed limestone from time-of-flight neutron diffraction spectra. J. Appl. Phys. 81, 594–600. doi:10.1063/1.364220

Mainprice, D., Hielscher, R., Schaeben, H., 2011. Calculating anisotropic physical properties from texture data using the MTEX open source package 1–33. doi:10.1144/SP360.10

Malvoisin, B., Brantut, N., Kaczmarek, M.-A., 2017. Control of serpentinisation rate by reaction-induced cracking. Earth Planet. Sci. Lett. 476, 143–152. doi:10.1016/j.epsl.2017.07.042

Matthies, S., Vinel, G.W., 1982. On the Reproduction of the Orientation Distribution Function of Texturized Samples from Reduced Pole Figures Using the Conception of a Conditional Ghost Correction. Phys. status solidi 112, K111–K114. doi:10.1002/pssb.2221120254

Miller, D.J., Christensen, N.I., 1997. Seismic velocities of lower crustal and upper mantle rocks from the slow-spreading mid-Atlantic ridge, south of the Kane transform Zone (MARK), in: Proceedings of the Ocean Drilling Program, Scientific Results Leg 135. College Station, Texas.

Passerini, L., 1930. Ricerche sugli Spinelli. II. I. Composti. Cu Al2 O4, Mg Al2 O4 , Mg Fe2 O4, Zn Al2 O4, Zn Cr2 O4, Zn Fe2 O4, Mn Fe2 O4. Gazz. Chim. Ital. 60, 389–399.

Plümper, O., Royne, A., Magrasó, A., Jamtveit, B., 2012. The interface-scale mechanism of reaction-induced fracturing during serpentinization. Geology 40, 1103–1106. doi:10.1130/G33390.1

Rouméjon, S., Cannat, M., 2014. Serpentinization of mantle-derived peridotites at mid-ocean ridges: Mesh texture development in the context of tectonic exhumation. Geochemistry Geophys. Geosystems 15, 2354–2379. doi:10.1002/2013GC005148

Rouméjon, S., Früh-Green, G.L., Orcutt, B.N., & the Expedition 357 Science Party, 2018. Alteration heterogeneities in peridotites exhumed on the southern wall of the Atlantis Massif ( IODP Expedition 357 ). doi:10.1093/petrology/egy065/5042903

Tucholke, B.E., Lin, J., 1994. A geological model for the structure of ridge segments in slow spreading ocean crust. J. Geophys. Res. Solid Earth 99, 11937–11958. doi:10.1029/94JB00338

Tucholke, E., Lin, J., Kleinrock, C., 1998. Megamullions and mullion structure defining oceanic metamorphic core complexes on the Mid-Atlantic Ridge. J. Geophys. Res. 103, 9857–

9866. doi:10.1029/98JB00167

Ulmer, P., Trommsdorff, V., 1995. Serpentine Stability to Mantle Depths and Subduction-Related Magmatism 268, 858–862. doi:10.1126/science.268.5212.858

Viti, C., Mellini, M., 1998. Mesh textures and bastites in the Elba retrograde serpentinites. Eur. J. Mineral. 10, 1341–1359.

Wicks, F.J., 1984a. Deformation histories as recorded by serpentinites. I. Deformation prior to serpentinization. Can. Mineral. 22, 185–195.

Wicks, F.J., 1984b. Deformation histories as recorded by serpentinites. II. Deformation during and after serpentinization. Can. Mineral. 22, 197–203.

Wicks, F.J., 1984c. Deformation histories as recorded by serpentinites. III. Fracture patterns developed prior to serpentinization. Can. Mineral. 22, 205–209.

Wicks, F.J., Whittaker, E.J.W., 1977. Serpentine textures and serpentinization. Can. Mineral. 15, 459–488.

Wicks, F.J., Whittaker, E.J.W., Zussman, J., 1977. A idealized model for serpentine textures after olivine. Can. Mineral. 15, 446–458.

# 6. Summary, Discussion & Conclusion

The aim of this thesis was the development and application of an advanced methodology for the analysis of quantitative bulk rock textures using synchrotron diffraction. So far applied measurement strategies like those used by e.g. Lutterotti et al. (2010); Schumann et al. (2014); Wenk et al. (2010) were improved and extended. In three case studies with phyllosilicate-rich samples, it was demonstrated that synchrotron texture analysis is a powerful tool to study the texture development in delicate polycrystalline multiphase samples.

In the first case study (Chapter 3) on the texture and AMS of Devonian black shales it could be demonstrated by modeling the AMS from texture that the phyllosilicates carry the anisotropy in absence of ferromagnetic minerals. Modeling the principal direction was very successful and fitted very well with the experimental AMS measurements, while the models were less successful when comparing the total susceptibility. These differences might be a result of different chemical composition of intrinsic susceptibility of literature phases ad those actually present in the samples. The study gives new insights on how magnetic fabric is formed in detail. Furthermore, it was possible to link kinked phyllosilicates in the microstructure, the appearance of the pole figure maxima, and therefore the magnetic lineation, to far field deformation by the Alleghenian orogeny.

In the second case study (Chapter 4), the texture of clay-rich sedimentary samples from the subduction zone offshore Costa Rica was determined. These samples are highly delicate in handling as they contain clay minerals. According to their tectonic setting the sediments from IODP cores drilled during expeditions 334 and 344 on the incoming plate and accretionary prism are less textured than the samples from the slope. This is due to the total smectite content, lower compaction rates and higher porosity. Due to the inclination of the foliation plane and the pole figure geometry it was possible to relate some samples to faulting and folding in the slope and its sedimentary cover.

In the third case study (Chapter 5) oceanic serpentinite samples from the Atlantis Massif at the Mid-Atlantic Ridge were analyzed regarding their texture. The samples were drilled during IODP expedition 357. Texture analysis of serpentinites has been challenging in the past as more conventional methods hit their limits due to the curly and fibrous habit of the low-temperature serpentine minerals lizardite and chrysotile. Two mechanisms of texture formation in oceanic serpentinites were identified; firstly, the appearance of bastites leads to local (001) pole figure maxima which could get more regional when the precursor pyroxene already involved a CPO. And secondly, a pre- or syn-serpentinization strain which led to the development of parallel serpentinizing microfractures invokes a texture to the rocks.

## 6.1. Application of synchrotron texture analysis

The method overcomes the severe limitations posed by more conventional texture analysis methods used in geosciences, but it is limited to fine grained samples due to the small beam size. By employing a certain sample diameter and measuring several slices of the samples, limitations arising from grain size can be extended. Still coarse grained samples cannot be measured, but as they are more likely to be suitable for the conventional methods, it was not the intention of this thesis to implement the method for all kinds of rocks and samples.

The advantages of synchrotron texture analysis with regard to the more conventional texture analysis methods generally applied in geosciences are in detail discussed in Chapter 4.5.1.

The three case studies posed three different problems to quantitative texture analysis: the first case study in Chapter 3 demanded a destruction free method to use the same sample material for AMS and texture analysis and showed a wide range of grain sizes. Due to the enlarged sample size it was possible to use the same samples for AMS and texture measurements. The second case study concerned mud samples whose water-bearing fabric is very sensitive to drying and external manipulation. Due to the measurement of sample cylinders, preparation could be restricted to a minimum and does therefore not or only slightly affect the delicate microstructure of such samples. Considering the measured sample diameter and volume external minor manipulations become negligible. The samples in the third case study in Chapter 5 had crystallographic issues and incorporated water in their crystal lattice. Synchrotron radiation is unaffected by the water in the crystal lattice and by applying Rietveld texture analysis it was possible to analyze the unconventional crystallographic patterns.

Beside the great improvements the method introduces to quantitative texture analysis of delicate samples, some constraints have to be considered. It turned out to be very difficult to determine the modal composition and the texture from rock samples, when it comes to delicate samples, especially the clay-rich sediments. For the composition of the samples it is still more reasonable to analyze the bulk composition from random powder samples, especially when considering delicate samples including e.g. swelling or irregularly stacked minerals. Nevertheless, this has no impact on texture analysis and calculation.

## 6.2. Significance of phyllosilicate textures

The three case studies focused on three totally different rocks incorporating a broad range of different phyllosilicate minerals. The black shales presented in Chapter 3 included illite/muscovite and chlorite. The samples are highly textured which was mostly induced by burial compaction. A slight elliptification of the (001) maximum in the pole figures of both minerals recorded layer parallel shortening as far field deformation, which is documented in the signal of the physical properties. The muds and mudrocks in Chapter 4 consist to a large extent from the clay minerals smectite, kaolinite and illite. These minerals report tectonic

movements, probably at small scale, in the partially soft material of the accretionary wedge, which were not documented so far. The serpentine minerals lizardite and chrysotile are also phyllosilicates and underline the importance of the combination of texture and microstructure analysis, as the texture in some samples is defined by re-mineralization only while in other samples it is a combination of deformation and re-mineralization.

The results show that also samples and lithologies which seem to be of minor interest regarding deformation and anisotropy of physical properties can yield important information about tectonic processes. Phyllosilicates, due to their strong shape anisotropy, can be really sensitive to tectonic processes and therefore record movements which are otherwise unrecognized.

In all three case studies, the texture formation due to intra-crystalline plastic deformation was less important than usually considered when talking about textures. It is sedimentary and remineralization processes in combination with brittle or far field deformation that control texture formation in these rocks. So, the interpretation of phyllosilicate textures should always be done carefully and the microstructure and composition should always be explored with regard to texture origin. Large scale tectonics always leave their foot print in the microscale universe.

## 6.3. Conclusion

The application of synchrotron texture analysis in combination with Rietveld refinement enlarges the field of quantitative texture analysis to delicate rocks which can have an irregular crystallography. The analyzed rocks pose problems to more conventional texture analysis due to the different special mineralogical or crystallographic features. By implying a new workflow and measuring a certain sample volume and several slices of cylindrical samples, it was possible to overcome restrictions of very fine grain sizes. The results were successfully used to monitor far field compression, brittle faulting in a wedge associated with a subduction zone and metamorphic re-mineralization which can be a result of spreading-related detachment faulting. As phyllosilicates are rheologically weak, they get affected by slight tectonic deformations first and record it. This was demonstrated for three case studies concerning different rocks from different tectonic settings. The texture and microstructure in Appalachian black shales was successfully used to model the AMS and showed layer parallel shortening from far field deformation. Muds and mudrocks from the sedimentary cover of the Costa Rica subduction zone showed faulting and folding recorded by the texture. In oceanic serpentinites from the Atlantis Massif oceanic core complex texture was identified, caused by serpentinization mechanisms and pre-serpentinization strain. The determined texture can then be used to model physical properties like anisotropy of the magnetic susceptibility and seismic P-wave anisotropy.

## References

Lutterotti, L., Voltolini, M., Wenk, H.R., Bandyopadhyay, K., Vanorio, T., 2010. Texture analysis of a turbostratically disordered Ca-montmorillonite. Am. Mineral. 95, 98–103. doi:10.2138/am.2010.3238

Schumann, K., Stipp, M., Leiss, B., Behrmann, J.H., 2014. Texture development in naturally compacted and experimentally deformed silty clay sediments from the Nankai Trench and Forearc, Japan. Tectonophysics 636, 125–142. doi:10.1016/j.tecto.2014.08.005

Wenk, H.-R., Kanitpanyacharoen, W., Voltolini, M., 2010. Preferred orientation of phyllosilicates: Comparison of fault gouge, shale and schist. J. Struct. Geol. 32, 478–489. doi:10.1016/j.jsg.2010.02.003

# Appendix

A1 Synchrotron texture refinement with MAUD

A2 Supplementary material to the manuscript in Chapter 3: “Quantitative comparison of microfabric and magnetic fabric in black shales from the Appalachian plateau (western Pennsylvania, U.S.A.) by AMS modeling”

# A1 Synchrotron Texture Refinement with MAUD

This manual describes the work flow which was used to analyze the texture data presented in this thesis. This procedure was successful for the data analyzed and presented in this thesis and is not necessarily recommended for different samples and data. The manual was developed based on the work routines given by Lutterotti et al. (2014); Schumann (2013); Wenk et al. (2014). The reader is referred to these studies for further information.
The programs used (Maud (Lutterotti et al., 1997), Fit2D (Hammersley, 1998), Mtex (Hielscher and Schaeben, 2008) are freeware and can be downloaded at the source given in the Literature. Only Mtex is Matlab-based and therefore needs to be run in Matlab.

## Refinement of a standard

Standard measurements are executed to define the instrumental parameters used for the refinements. From the experimental measurements the following parameters should be known by the user:

- Wavelength
- Sample-detector distance
- Detector parameters: pixel size and number or size in each direction
- Rotational measurement step

In Fit2D the beam center can be determined from the Standard as described by (Schumann, 2013). Then in Maud the Standard can be refined using this information, following the instructions given by (Lutterotti et al., 2014) and the online available appendix (http://eps.berkeley.edu/~wenk/TexturePage/MAUD.htm). The Fit2D beam center is probably more precise than a determination “by hand” in Maud itself.

## Data transformation & input

Depending on the detector used for the synchrotron measurements the results will be in *.esg or *.mar format or else. Using the Fit2D program, the images can be converted in tiff16bit data, which are suitable to be used in Maud.
Additionally, an average file of all 36 measured images can be created using the File Series -> Average option. Using the average file will speed up the refinement.
When loading the average file in Maud as described by (Lutterotti et al., 2014; Schumann, 2013) pay attention to the orientation of the image (already when you refine the Standard). The orientation necessary for Maud is given by (Lutterotti et al., 2014). This is essential for texture calculation.

## Sample Refinement using the average file

Refining a file in Maud is described by (Lutterotti et al., 2014; Schumann, 2013; Wenk et al., 2014). This is the refinement routine used here:

a. Background and scale factors
b. Instrumental parameters: intensity, beam center, wavelength, sample detector distance
c. Crystallographic parameters, each phase separately, be careful to only refine components which are clearly defined by their peaks
d. Parameters defining peak broadening: crystallite size & microstrain
e. Temperature factor B-iso
f. Give every phase the texture model EWIMV (derived from WIMV (Matthies and Vinel, 1982)
g. Duplicate the datafileset 36 times (or the number of single step measurements you have done)
h. Load the single step measurements separately in the 36 datafilesets
i. Calculate texture

## Pole figure extraction & treatment

Pole figures and ODF can be extracted from the EWIMV panel. The pole figures in *.xpc format can then be imported in Mtex. Here pole figures can be visualized in different ways, used for physical property calculations.

## References

Hammersley, A.P., 1998. FIT2D V9.129 Reference Manual V3.1. Inter Rep ESRF98HA01. Grenoble.

Hielscher, R., Schaeben, H., 2008. A novel pole figure inversion method: specification of the MTEX algorithm. J. Appl. Crystallogr. 41, 1024–1037. doi:10.1107/S0021889808030112

Lutterotti, L., Matthies, S., Wenk, H.-R., Schultz, A.S., Richardson, J.W., 1997. Combined texture and structure analysis of deformed limestone from time-of-flight neutron diffraction spectra. J. Appl. Phys. 81, 594–600. doi:10.1063/1.364220

Lutterotti, L., Vasin, R., Wenk, H.-R., 2014. Rietveld texture analysis from synchrotron diffraction images I. Calibration and basic analysis. Powder Diffr. 29, 76–84. doi:10.1017/S0885715613001346

Matthies, S., Vinel, G.W., 1982. On the Reproduction of the Orientation Distribution Function of Texturized Samples from Reduced Pole Figures Using the Conception of a Conditional Ghost Correction. Phys. status solidi 112, K111–K114. doi:10.1002/pssb.2221120254

Schumann, K., 2013. Strength, textures, microfabrics and acoustic properties of active plate margin sediments on- and offshore SW Japan. PhD thesis, Christian-Albrechts-University Kiel.
Wenk, H., Lutterotti, L., Kaercher, P., Kanitpanyacharoen, W., Miyagi, L., Vasin, R., 2014. Rietveld texture analysis from synchrotron diffraction images . II . Complex multiphase materials and diamond envil cell experiments. Powder Diffr. 29, 220–232. doi:10.1017/S0885715614000360

## A2 Supplementary material to manuscript “Quantitative comparison of microfabric and magnetic fabric in black shales from the Appalachian plateau (western Pennsylvania, U.S.A.)” by Kuehn, R., Hirt, A.M., Biedermann, A.R., Leiss,B. in revision at *Tectonophysics*

| | |
|---|---|
| Supplementary Table 1 | Low-field AMS data |
| Supplementary Table 2 | High-field AMS data |
| Supplementary Table 3 | Modeled AMS data |
| Supplementary Figure 1 | Model contributions of the different minerals |

Supplementary Table 1 Eigenvalues and eigendirections for principal axes of the deviatoric tensor for the bulk magnetic component with their corresponding anisotropy parameters as determined from low-field AMS measurements

| Sample | k_mean | k1 | Dec k1 | Inc k1 | k2 | Dec k2 | Inc k2 | k3 | Dec k3 | Inc k3 | k' | U | k'% |
|---|---|---|---|---|---|---|---|---|---|---|---|---|---|
| 3522,21 | 2,70E-04 | 1,050 | 34,9 | 0,9 | 1,0440 | 124,9 | 0,0 | 0,906 | 214,9 | 89,1 | 2,703E-04 | 0,93 | 6,6 |
| 3522,22 | 2,65E-04 | 1,048 | 49,4 | 0,6 | 1,0420 | 139,4 | 1,1 | 0,910 | 290,4 | 88,7 | 2,647E-04 | 0,92 | 6,4 |
| 3522,23 | 2,69E-04 | 1,051 | 28,0 | 1,2 | 1,0440 | 118,1 | 1,9 | 0,905 | 266,1 | 87,7 | 2,685E-04 | 0,91 | 6,7 |
| 3522,24 | 2,70E-04 | 1,052 | 21,6 | 0,9 | 1,0450 | 111,6 | 0,4 | 0,903 | 226,0 | 89,0 | 2,696E-04 | 0,91 | 6,9 |
| 3531,91 | 3,18E-04 | 1,052 | 49,7 | 1,0 | 1,0470 | 319,6 | 1,6 | 0,902 | 172,6 | 88,1 | 3,182E-04 | 0,93 | 6,9 |
| 3531,92 | 3,11E-04 | 1,051 | 221,1 | 2,8 | 1,0460 | 131,1 | 0,2 | 0,903 | 37,0 | 87,2 | 3,114E-04 | 0,93 | 6,8 |
| 3531,93 | 3,09E-04 | 1,052 | 234,9 | 1,8 | 1,0460 | 324,9 | 0,0 | 0,902 | 56,4 | 88,2 | 3,086E-04 | 0,93 | 6,9 |
| 3531,94 | 3,12E-04 | 1,053 | 243,4 | 1,5 | 1,0470 | 333,4 | 0,8 | 0,901 | 90,0 | 88,3 | 3,122E-04 | 0,93 | 7,0 |
| 3542,71 | 3,12E-04 | 1,048 | 38,0 | 1,1 | 1,0440 | 128,0 | 0,9 | 0,908 | 256,9 | 88,6 | 3,120E-04 | 0,94 | 6,5 |
| 3542,72 | 3,10E-04 | 1,048 | 232,0 | 0,3 | 1,0440 | 322,0 | 0,1 | 0,908 | 63,8 | 89,7 | 3,103E-04 | 0,94 | 6,5 |
| 3542,73 | 3,16E-04 | 1,049 | 222,6 | 1,7 | 1,0450 | 132,5 | 0,6 | 0,906 | 23,6 | 88,2 | 3,158E-04 | 0,94 | 6,7 |
| 3552,21 | 8,87E-04 | 1,042 | 284,1 | 87,8 | 0,9820 | 127,2 | 2,0 | 0,977 | 37,2 | 0,8 | 8,865E-04 | -0,86 | 2,9 |
| 3552,22 | 8,54E-04 | 1,037 | 278,6 | 87,5 | 0,9840 | 124,1 | 2,2 | 0,979 | 34,1 | 1,1 | 8,538E-04 | -0,81 | 2,6 |
| 3552,23 | 8,37E-04 | 1,036 | 286,5 | 86,5 | 0,9840 | 137,5 | 3,0 | 0,979 | 47,4 | 1,8 | 8,367E-04 | -0,82 | 2,6 |
| 3572,81 | 3,06E-04 | 1,040 | 217,7 | 1,3 | 1,0380 | 307,8 | 1,3 | 0,921 | 84,0 | 88,2 | 3,063E-04 | 0,96 | 5,6 |
| 3572,82 | 3,06E-04 | 1,041 | 59,0 | 1,7 | 1,0390 | 329,0 | 0,5 | 0,919 | 221,4 | 88,2 | 3,064E-04 | 0,96 | 5,7 |
| 3572,83 | 3,06E-04 | 1,040 | 219,3 | 1,9 | 1,0350 | 309,4 | 3,3 | 0,925 | 98,9 | 86,2 | 3,061E-04 | 0,92 | 5,3 |
| 3583,21 | 4,11E-04 | 1,014 | 247,5 | 0,5 | 1,0120 | 157,5 | 0,2 | 0,974 | 44,2 | 89,5 | 4,111E-04 | 0,93 | 1,9 |
| 3583,22 | 4,20E-04 | 1,011 | 58,3 | 0,9 | 1,0100 | 148,3 | 1,2 | 0,979 | 289,5 | 88,5 | 4,203E-04 | 0,93 | 1,5 |
| 3583,23 | 3,84E-04 | 1,019 | 308,0 | 0,6 | 1,0180 | 38,0 | 0,3 | 0,964 | 153,9 | 89,3 | 3,836E-04 | 0,95 | 2,6 |
| 3583,24 | 4,22E-04 | 1,010 | 90,0 | 1,9 | 1,0100 | 0,0 | 0,0 | 0,979 | 270,0 | 88,1 | 4,217E-04 | 1,00 | 1,5 |
| 3593,71 | 1,91E-04 | 1,040 | 51,3 | 0,4 | 1,0310 | 321,3 | 0,5 | 0,929 | 177,6 | 89,4 | 1,909E-04 | 0,83 | 5,0 |
| 3593,72 | 1,93E-04 | 1,040 | 221,8 | 0,2 | 1,0320 | 131,8 | 1,2 | 0,928 | 322,3 | 88,7 | 1,928E-04 | 0,85 | 5,1 |
| 3593,73 | 1,90E-04 | 1,039 | 233,8 | 1,5 | 1,0320 | 143,8 | 1,8 | 0,929 | 3,9 | 87,6 | 1,904E-04 | 0,86 | 5,0 |
| 3603,71 | 2,90E-04 | 1,048 | 28,5 | 1,0 | 1,0440 | 298,5 | 0,6 | 0,909 | 176,1 | 88,9 | 2,903E-04 | 0,95 | 6,5 |

| Sample | k_mean | k1 | Dec k1 | Inc k1 | k2 | Dec k2 | Inc k2 | k3 | Dec k3 | Inc k3 | k' | U | k'% |
|---|---|---|---|---|---|---|---|---|---|---|---|---|---|
| 3603,72 | 2,96E-04 | 1,047 | 51,3 | 0,4 | 1,0420 | 141,3 | 0,1 | 0,911 | 252,3 | 89,6 | 2,963E-04 | 0,92 | 6,3 |
| 3603,73 | 2,94E-04 | 1,048 | 64,7 | 1,6 | 1,0440 | 334,7 | 0,8 | 0,908 | 217,0 | 88,2 | 2,941E-04 | 0,94 | 6,5 |
| 3603,74 | 2,92E-04 | 1,048 | 51,2 | 0,8 | 1,0430 | 141,2 | 1,2 | 0,909 | 286,9 | 88,6 | 2,924E-04 | 0,93 | 6,4 |
| 3623,31 | 2,61E-04 | 1,048 | 42,9 | 0,5 | 1,0430 | 133,0 | 1,1 | 0,910 | 291,3 | 88,8 | 2,607E-04 | 0,93 | 6,4 |
| 3623,32 | 2,61E-04 | 1,047 | 40,9 | 1,3 | 1,0430 | 131,0 | 1,1 | 0,910 | 261,5 | 88,3 | 2,605E-04 | 0,93 | 6,4 |
| 3623,33 | 2,57E-04 | 1,048 | 198,6 | 0,7 | 1,0400 | 108,6 | 0,3 | 0,912 | 358,9 | 89,2 | 2,565E-04 | 0,88 | 6,2 |
| 3623,34 | 2,59E-04 | 1,046 | 38,5 | 0,5 | 1,0410 | 128,5 | 1,5 | 0,914 | 290,8 | 88,5 | 2,593E-04 | 0,93 | 6,1 |
| 3634,11 | 3,02E-04 | 1,053 | 40,6 | 0,0 | 1,0480 | 310,6 | 0,9 | 0,899 | 132,5 | 89,1 | 3,019E-04 | 0,94 | 7,2 |
| 3634,12 | 2,67E-04 | 1,053 | 34,3 | 0,5 | 1,0480 | 124,3 | 1,1 | 0,899 | 282,5 | 88,8 | 2,671E-04 | 0,94 | 7,2 |
| 3644,82 | 2,58E-04 | 1,045 | 219,2 | 2,2 | 1,0390 | 309,3 | 1,8 | 0,916 | 78,7 | 87,2 | 2,581E-04 | 0,92 | 5,9 |
| 3653,41 | 2,51E-04 | 1,050 | 26,7 | 1,8 | 1,0450 | 116,7 | 2,4 | 0,905 | 259,9 | 87,1 | 2,513E-04 | 0,93 | 6,7 |
| 3653,42 | 2,54E-04 | 1,051 | 27,2 | 1,1 | 1,0470 | 117,3 | 3,1 | 0,902 | 278,7 | 86,7 | 2,538E-04 | 0,95 | 6,9 |
| 3653,43 | 2,54E-04 | 1,052 | 14,8 | 1,1 | 1,0450 | 104,9 | 2,6 | 0,904 | 262,5 | 87,2 | 2,536E-04 | 0,91 | 6,8 |
| 3665,71 | 1,85E-04 | 1,038 | 212,3 | 4,5 | 1,0350 | 122,2 | 1,3 | 0,928 | 16,5 | 85,3 | 1,851E-04 | 0,95 | 5,1 |
| 3665,72 | 1,93E-04 | 1,039 | 213,9 | 3,2 | 1,0340 | 123,7 | 3,1 | 0,927 | 349,6 | 85,5 | 1,926E-04 | 0,91 | 5,2 |
| 3665,73 | 1,89E-04 | 1,038 | 208,8 | 1,6 | 1,0310 | 118,7 | 4,1 | 0,931 | 319,6 | 85,6 | 1,888E-04 | 0,87 | 4,9 |
| 3665,74 | 1,82E-04 | 1,036 | 210,2 | 0,2 | 1,0330 | 300,2 | 1,7 | 0,931 | 112,8 | 88,2 | 1,821E-04 | 0,94 | 4,9 |
| 3674,51 | 1,59E-04 | 1,030 | 209,3 | 2,7 | 1,0260 | 119,2 | 0,5 | 0,944 | 19,2 | 87,2 | 1,589E-04 | 0,91 | 3,9 |
| 3674,52 | 1,59E-04 | 1,030 | 216,3 | 2,7 | 1,0260 | 306,3 | 0,6 | 0,944 | 48,4 | 87,3 | 1,590E-04 | 0,91 | 4,0 |
| 3674,53 | 1,58E-04 | 1,030 | 211,7 | 1,6 | 1,0250 | 121,7 | 1,0 | 0,945 | 358,4 | 88,1 | 1,579E-04 | 0,88 | 3,9 |
| 3685,41 | 1,53E-04 | 1,028 | 205,1 | 0,1 | 1,0240 | 115,1 | 0,4 | 0,948 | 303,3 | 89,6 | 1,526E-04 | 0,91 | 3,7 |
| 3685,42 | 1,53E-04 | 1,029 | 188,7 | 0,2 | 1,0240 | 98,7 | 0,6 | 0,947 | 299,8 | 89,4 | 1,529E-04 | 0,88 | 3,8 |
| 3685,43 | 1,54E-04 | 1,028 | 194,2 | 1,0 | 1,0250 | 104,2 | 0,6 | 0,947 | 343,8 | 88,8 | 1,543E-04 | 0,93 | 3,7 |
| 3695,41 | 2,40E-04 | 1,049 | 42,3 | 1,0 | 1,0460 | 312,2 | 2,5 | 0,906 | 155,2 | 87,3 | 2,404E-04 | 0,96 | 6,7 |
| 3695,42 | 2,43E-04 | 1,051 | 256,9 | 2,0 | 1,0460 | 346,9 | 0,6 | 0,902 | 94,2 | 87,9 | 2,434E-04 | 0,93 | 6,9 |
| 3695,43 | 2,24E-04 | 1,050 | 20,3 | 1,0 | 1,0460 | 290,2 | 5,1 | 0,904 | 121,0 | 84,8 | 2,242E-04 | 0,95 | 6,8 |
| 3695,44 | 2,44E-04 | 1,050 | 28,2 | 1,8 | 1,0460 | 298,1 | 2,2 | 0,904 | 157,3 | 87,1 | 2,438E-04 | 0,95 | 6,8 |

| Sample | k_mean | k1 | Dec k1 | Inc k1 | k2 | Dec k2 | Inc k2 | k3 | Dec k3 | Inc k3 | k' | U | k'% |
|---|---|---|---|---|---|---|---|---|---|---|---|---|---|
| 3705,21 | 2,28E-04 | 1,054 | 211,0 | 0,6 | 1,0470 | 121,0 | 1,7 | 0,899 | 319,4 | 88,3 | 2,279E-04 | 0,91 | 7,1 |
| 3705,22 | 2,36E-04 | 1,051 | 46,0 | 0,1 | 1,0460 | 136,0 | 0,1 | 0,903 | 271,0 | 89,9 | 2,360E-04 | 0,93 | 6,8 |
| 3714,61 | 2,68E-04 | 1,049 | 36,0 | 0,1 | 1,0440 | 306,0 | 0,0 | 0,907 | 206,2 | 89,9 | 2,684E-04 | 0,93 | 6,6 |
| 3714,62 | 2,71E-04 | 1,047 | 225,8 | 0,1 | 1,0410 | 135,8 | 0,9 | 0,912 | 324,6 | 89,1 | 2,713E-04 | 0,91 | 6,2 |
| 3714,63 | 2,65E-04 | 1,050 | 29,3 | 0,1 | 1,0430 | 299,3 | 2,0 | 0,907 | 123,5 | 88,0 | 2,645E-04 | 0,90 | 6,6 |
| 3727,51 | 2,34E-04 | 1,046 | 221,8 | 1,8 | 1,0410 | 311,8 | 1,4 | 0,913 | 80,6 | 87,7 | 2,337E-04 | 0,92 | 6,1 |
| 3727,52 | 2,28E-04 | 1,046 | 222,8 | 2,0 | 1,0390 | 312,9 | 2,0 | 0,915 | 87,8 | 87,2 | 2,277E-04 | 0,90 | 6,0 |
| 3727,53 | 2,25E-04 | 1,041 | 236,1 | 2,7 | 1,0370 | 326,2 | 1,9 | 0,922 | 91,1 | 86,7 | 2,245E-04 | 0,92 | 5,5 |
| 3739,01 | 1,70E-04 | 1,037 | 41,4 | 1,2 | 1,0330 | 311,4 | 0,3 | 0,931 | 206,0 | 88,8 | 1,700E-04 | 0,92 | 4,9 |
| 3739,02 | 1,69E-04 | 1,037 | 227,6 | 0,8 | 1,0310 | 137,6 | 0,0 | 0,933 | 44,8 | 89,2 | 1,691E-04 | 0,89 | 4,8 |
| 3739,03 | 1,70E-04 | 1,037 | 233,7 | 0,4 | 1,0330 | 143,7 | 0,8 | 0,930 | 349,6 | 89,1 | 1,699E-04 | 0,92 | 5,0 |
| 3751,21 | 2,38E-04 | 1,044 | 239,9 | 0,3 | 1,0380 | 149,9 | 0,3 | 0,918 | 9,9 | 89,6 | 2,383E-04 | 0,90 | 5,8 |
| 3751,22 | 2,24E-04 | 1,043 | 218,0 | 0,3 | 1,0370 | 128,0 | 0,8 | 0,920 | 327,1 | 89,1 | 2,244E-04 | 0,91 | 5,7 |
| 3751,23 | 2,29E-04 | 1,044 | 41,9 | 0,2 | 1,0390 | 311,9 | 0,4 | 0,917 | 157,2 | 89,5 | 2,294E-04 | 0,91 | 5,8 |
| 3751,24 | 2,32E-04 | 1,043 | 228,0 | 0,6 | 1,0370 | 318,1 | 1,2 | 0,920 | 110,7 | 88,6 | 2,320E-04 | 0,91 | 5,7 |
| 3763,41 | 2,00E-04 | 1,047 | 20,8 | 1,6 | 1,0420 | 110,8 | 1,1 | 0,911 | 235,4 | 88,0 | 1,997E-04 | 0,92 | 6,3 |
| 3763,42 | 1,98E-04 | 1,047 | 29,7 | 1,1 | 1,0420 | 119,7 | 1,1 | 0,911 | 253,8 | 88,4 | 1,983E-04 | 0,92 | 6,3 |
| 3763,43 | 1,99E-04 | 1,047 | 42,1 | 2,1 | 1,0420 | 312,1 | 0,0 | 0,911 | 221,0 | 87,9 | 1,993E-04 | 0,93 | 6,3 |
| 3763,44 | 2,00E-04 | 1,047 | 19,9 | 1,2 | 1,0400 | 289,9 | 0,3 | 0,914 | 183,6 | 88,8 | 2,003E-04 | 0,90 | 6,1 |
| 3774,51 | 1,46E-04 | 1,032 | 45,3 | 3,4 | 1,0290 | 135,8 | 8,9 | 0,939 | 294,4 | 80,4 | 1,461E-04 | 0,95 | 4,3 |
| 3774,52 | 1,47E-04 | 1,032 | 208,4 | 1,0 | 1,0300 | 118,2 | 9,5 | 0,937 | 304,5 | 80,5 | 1,466E-04 | 0,96 | 4,4 |
| 3774,53 | 1,45E-04 | 1,033 | 201,3 | 1,1 | 1,0290 | 111,1 | 9,0 | 0,938 | 298,5 | 81,0 | 1,448E-04 | 0,93 | 4,4 |
| 3774,54 | 1,47E-04 | 1,032 | 36,7 | 0,7 | 1,0290 | 126,8 | 7,8 | 0,940 | 301,5 | 82,2 | 1,473E-04 | 0,93 | 4,3 |
| 3786,71 | 1,44E-04 | 1,032 | 20,1 | 1,1 | 1,0280 | 110,1 | 0,3 | 0,941 | 215,6 | 88,8 | 1,444E-04 | 0,92 | 4,2 |
| 3786,72 | 1,46E-04 | 1,032 | 210,3 | 0,5 | 1,0290 | 300,3 | 0,9 | 0,940 | 90,8 | 88,9 | 1,455E-04 | 0,94 | 4,3 |
| 3786,73 | 1,46E-04 | 1,032 | 20,3 | 1,4 | 1,0280 | 110,3 | 0,7 | 0,941 | 228,6 | 88,4 | 1,458E-04 | 0,91 | 4,2 |
| 3798,91 | 1,51E-04 | 1,038 | 43,6 | 0,4 | 1,0350 | 133,6 | 0,7 | 0,927 | 287,3 | 89,2 | 1,508E-04 | 0,95 | 5,2 |

| Sample | k_mean | k1 | Dec k1 | Inc k1 | k2 | Dec k2 | Inc k2 | k3 | Dec k3 | Inc k3 | k' | U | k'% |
|---|---|---|---|---|---|---|---|---|---|---|---|---|---|
| 3798,92 | 1,51E-04 | 1,039 | 42,2 | 0,0 | 1,0360 | 132,2 | 1,6 | 0,925 | 310,8 | 88,4 | 1,512E-04 | 0,95 | 5,3 |
| 3798,93 | 1,48E-04 | 1,039 | 41,4 | 0,6 | 1,0360 | 311,4 | 0,1 | 0,925 | 215,4 | 89,4 | 1,478E-04 | 0,96 | 5,3 |
| 3798,94 | 1,52E-04 | 1,040 | 205,1 | 0,2 | 1,0370 | 115,1 | 0,3 | 0,924 | 322,4 | 89,6 | 1,517E-04 | 0,94 | 5,4 |
| 3813,91 | 2,08E-04 | 1,037 | 42,1 | 0,8 | 1,0330 | 312,1 | 0,3 | 0,930 | 202,5 | 89,1 | 2,079E-04 | 0,92 | 5,0 |
| 3813,92 | 2,07E-04 | 1,036 | 38,0 | 0,0 | 1,0320 | 308,0 | 0,6 | 0,933 | 128,0 | 89,4 | 2,070E-04 | 0,92 | 4,8 |
| 3813,93 | 2,09E-04 | 1,036 | 232,7 | 0,9 | 1,0320 | 322,8 | 1,1 | 0,931 | 105,1 | 88,6 | 2,092E-04 | 0,93 | 4,9 |
| 3813,94 | 2,07E-04 | 1,037 | 43,2 | 1,4 | 1,0320 | 133,2 | 1,7 | 0,931 | 274,2 | 87,8 | 2,069E-04 | 0,92 | 4,9 |
| 3826,61 | 2,09E-04 | 1,039 | 221,1 | 1,2 | 1,0350 | 131,1 | 1,8 | 0,926 | 344,3 | 87,8 | 2,087E-04 | 0,93 | 5,2 |
| 3826,62 | 2,08E-04 | 1,038 | 222,1 | 0,9 | 1,0340 | 132,1 | 0,3 | 0,928 | 26,0 | 89,0 | 2,083E-04 | 0,92 | 5,1 |
| 3826,63 | 2,08E-04 | 1,039 | 231,3 | 0,9 | 1,0350 | 141,3 | 0,6 | 0,927 | 17,5 | 89,0 | 2,082E-04 | 0,93 | 5,2 |
| 3826,64 | 2,09E-04 | 1,039 | 36,7 | 0,3 | 1,0340 | 306,6 | 1,2 | 0,927 | 141,5 | 88,7 | 2,088E-04 | 0,92 | 5,1 |
| 3840,41 | 2,27E-04 | 1,038 | 221,4 | 0,3 | 1,0330 | 311,4 | 1,6 | 0,929 | 122,0 | 88,4 | 2,268E-04 | 0,92 | 5,1 |
| 3840,42 | 2,28E-04 | 1,038 | 218,0 | 0,1 | 1,0340 | 308,0 | 1,9 | 0,928 | 126,3 | 88,0 | 2,276E-04 | 0,92 | 5,1 |
| 3852,91 | 1,83E-04 | 1,043 | 52,6 | 0,5 | 1,0370 | 142,6 | 1,1 | 0,920 | 300,0 | 88,8 | 1,826E-04 | 0,91 | 5,6 |
| 3852,92 | 1,78E-04 | 1,042 | 49,3 | 0,2 | 1,0370 | 319,3 | 0,6 | 0,921 | 157,5 | 89,3 | 1,779E-04 | 0,92 | 5,6 |
| 3852,93 | 1,79E-04 | 1,042 | 53,8 | 1,0 | 1,0360 | 143,8 | 1,9 | 0,923 | 294,8 | 87,9 | 1,786E-04 | 0,91 | 5,5 |
| 3865,21 | 1,81E-04 | 1,042 | 38,6 | 0,8 | 1,0360 | 308,6 | 2,1 | 0,922 | 149,7 | 87,8 | 1,805E-04 | 0,91 | 5,5 |
| 3865,22 | 1,78E-04 | 1,041 | 46,4 | 0,6 | 1,0370 | 316,4 | 0,3 | 0,922 | 200,9 | 89,4 | 1,775E-04 | 0,92 | 5,5 |
| 3865,23 | 1,78E-04 | 1,042 | 45,0 | 1,3 | 1,0370 | 135,0 | 0,7 | 0,921 | 252,6 | 88,5 | 1,778E-04 | 0,91 | 5,6 |
| 3865,24 | 1,72E-04 | 1,043 | 40,7 | 1,0 | 1,0380 | 130,8 | 1,4 | 0,919 | 275,2 | 88,3 | 1,724E-04 | 0,92 | 5,7 |
| 3890,91 | 2,03E-04 | 1,041 | 40,7 | 2,0 | 1,0360 | 130,7 | 0,8 | 0,923 | 241,8 | 87,8 | 2,032E-04 | 0,92 | 5,5 |
| 3890,92 | 2,16E-04 | 1,042 | 218,0 | 1,0 | 1,0370 | 128,0 | 0,5 | 0,921 | 9,5 | 88,9 | 2,157E-04 | 0,93 | 5,6 |
| 3890,93 | 2,03E-04 | 1,041 | 43,8 | 1,5 | 1,0370 | 133,8 | 0,4 | 0,922 | 238,8 | 88,4 | 2,030E-04 | 0,94 | 5,5 |
| 3905,81 | 2,12E-04 | 1,037 | 45,0 | 0,2 | 1,0330 | 135,0 | 0,2 | 0,931 | 271,1 | 89,8 | 2,117E-04 | 0,92 | 4,9 |
| 3905,82 | 1,96E-04 | 1,037 | 234,7 | 1,0 | 1,0320 | 144,6 | 2,1 | 0,931 | 349,5 | 87,7 | 1,955E-04 | 0,91 | 4,9 |
| 3905,83 | 2,13E-04 | 1,037 | 213,9 | 0,7 | 1,0330 | 123,9 | 0,6 | 0,930 | 351,5 | 89,1 | 2,126E-04 | 0,91 | 4,9 |
| 3905,84 | 2,06E-04 | 1,041 | 42,6 | 1,0 | 1,0360 | 132,6 | 0,5 | 0,924 | 249,2 | 88,9 | 2,064E-04 | 0,91 | 5,4 |

| Sample | k_mean | k1 | Dec k1 | Inc k1 | k2 | Dec k2 | Inc k2 | k3 | Dec k3 | Inc k3 | k' | U | k'% |
|---|---|---|---|---|---|---|---|---|---|---|---|---|---|
| 3920,01 | 1,57E-04 | 1,037 | 36,8 | 0,0 | 1,0320 | 126,8 | 1,2 | 0,931 | 304,8 | 88,8 | 1,573E-04 | 0,91 | 4,9 |
| 3920,02 | 1,58E-04 | 1,037 | 209,4 | 0,1 | 1,0320 | 119,4 | 1,0 | 0,931 | 304,7 | 89,0 | 1,576E-04 | 0,91 | 4,9 |
| 3920,03 | 1,58E-04 | 1,036 | 31,0 | 0,2 | 1,0310 | 121,0 | 0,9 | 0,933 | 285,9 | 89,1 | 1,579E-04 | 0,91 | 4,7 |
| 3935,61 | 1,89E-04 | 1,041 | 233,3 | 1,5 | 1,0370 | 323,3 | 0,3 | 0,922 | 63,7 | 88,5 | 1,894E-04 | 0,94 | 5,5 |
| 3935,62 | 1,86E-04 | 1,040 | 219,0 | 0,7 | 1,0360 | 309,0 | 0,3 | 0,924 | 64,1 | 89,2 | 1,861E-04 | 0,94 | 5,4 |
| 3935,63 | 1,85E-04 | 1,040 | 220,9 | 1,0 | 1,0370 | 130,9 | 0,3 | 0,923 | 26,2 | 89,0 | 1,849E-04 | 0,94 | 5,4 |
| 3948,71 | 1,73E-04 | 1,033 | 216,8 | 1,1 | 1,0260 | 306,9 | 1,3 | 0,941 | 86,3 | 88,4 | 1,730E-04 | 0,85 | 4,2 |
| 3948,72 | 1,59E-04 | 1,031 | 216,5 | 0,2 | 1,0270 | 306,5 | 2,8 | 0,942 | 122,2 | 87,2 | 1,592E-04 | 0,91 | 4,1 |
| 3948,73 | 1,53E-04 | 1,031 | 234,2 | 0,7 | 1,0250 | 324,2 | 1,0 | 0,944 | 110,2 | 88,7 | 1,525E-04 | 0,86 | 4,0 |
| 3962,61 | 5,21E-05 | 1,017 | 71,2 | 2,0 | 1,0100 | 161,2 | 0,8 | 0,973 | 273,1 | 87,8 | 5,214E-05 | 0,69 | 2,0 |
| 3962,62 | 4,12E-05 | 1,012 | 243,4 | 1,5 | 1,0080 | 333,4 | 1,5 | 0,980 | 107,9 | 87,9 | 4,121E-05 | 0,75 | 1,4 |
| 3967,71 | 1,02E-04 | 1,035 | 96,0 | 10,4 | 1,0300 | 187,8 | 9,8 | 0,936 | 320,2 | 75,6 | 1,015E-04 | 0,90 | 4,6 |
| 3967,72 | 1,04E-04 | 1,031 | 239,2 | 3,2 | 1,0260 | 329,5 | 6,0 | 0,943 | 121,4 | 83,2 | 1,037E-04 | 0,88 | 4,0 |
| 3967,73 | 9,74E-05 | 1,034 | 107,9 | 16,1 | 1,0300 | 199,7 | 6,5 | 0,936 | 310,8 | 72,6 | 9,739E-05 | 0,92 | 4,5 |
| 3967,74 | 1,00E-04 | 1,029 | 54,2 | 0,5 | 1,0250 | 324,2 | 2,5 | 0,945 | 154,5 | 87,4 | 1,002E-04 | 0,91 | 3,9 |
| 3977,81 | 6,69E-05 | 1,004 | 3,2 | 1,4 | 1,0010 | 93,4 | 8,2 | 0,995 | 263,9 | 81,7 | 6,687E-05 | 0,29 | 0,4 |
| 3977,82 | 6,98E-05 | 1,003 | 180,0 | 1,1 | 1,0010 | 90,0 | 0,0 | 0,995 | 0,0 | 88,9 | 6,983E-05 | 0,59 | 0,3 |
| 3977,83 | 6,71E-05 | 1,003 | 184,0 | 2,8 | 1,0010 | 274,1 | 2,0 | 0,997 | 38,6 | 86,5 | 6,705E-05 | 0,23 | 0,3 |
| 3977,84 | 6,62E-05 | 1,004 | 7,5 | 2,3 | 1,0010 | 97,5 | 1,1 | 0,995 | 213,5 | 87,5 | 6,623E-05 | 0,41 | 0,4 |
| 3977,85 | 6,59E-05 | 1,004 | 18,9 | 2,6 | 1,0010 | 109,0 | 2,2 | 0,995 | 238,6 | 86,6 | 6,592E-05 | 0,18 | 0,4 |
| 3991,21 | 1,21E-04 | 1,034 | 220,3 | 3,0 | 1,0290 | 310,3 | 1,4 | 0,936 | 64,6 | 86,7 | 1,213E-04 | 0,90 | 4,5 |
| 3991,22 | 1,26E-04 | 1,035 | 215,2 | 1,5 | 1,0300 | 125,2 | 0,3 | 0,935 | 22,6 | 88,5 | 1,255E-04 | 0,90 | 4,6 |
| 3991,23 | 1,25E-04 | 1,035 | 217,9 | 2,5 | 1,0290 | 308,0 | 1,5 | 0,936 | 68,5 | 87,1 | 1,254E-04 | 0,89 | 4,5 |
| 3991,24 | 1,26E-04 | 1,036 | 221,9 | 1,9 | 1,0310 | 131,9 | 0,7 | 0,934 | 21,9 | 88,0 | 1,260E-04 | 0,90 | 4,7 |
| 4004,71 | 1,18E-04 | 1,040 | 212,8 | 1,5 | 1,0350 | 302,9 | 3,4 | 0,925 | 98,4 | 86,3 | 1,178E-04 | 0,92 | 5,3 |
| 4004,72 | 1,17E-04 | 1,041 | 206,7 | 1,4 | 1,0350 | 296,8 | 1,9 | 0,925 | 79,6 | 87,6 | 1,165E-04 | 0,90 | 5,3 |
| 4004,73 | 1,16E-04 | 1,040 | 216,8 | 1,5 | 1,0340 | 306,9 | 2,2 | 0,926 | 93,5 | 87,3 | 1,163E-04 | 0,90 | 5,3 |

| Sample | k_mean | k1 | Dec k1 | Inc k1 | k2 | Dec k2 | Inc k2 | k3 | Dec k3 | Inc k3 | k' | U | k'% |
|---|---|---|---|---|---|---|---|---|---|---|---|---|---|
| 4020,01 | 1,91E-04 | 1,044 | 46,3 | 1,4 | 1,0390 | 316,3 | 0,4 | 0,918 | 209,6 | 88,5 | 1,909E-04 | 0,92 | 5,8 |
| 4020,02 | 1,93E-04 | 1,044 | 46,2 | 0,9 | 1,0380 | 316,2 | 1,2 | 0,919 | 174,7 | 88,5 | 1,929E-04 | 0,91 | 5,8 |
| 4020,03 | 1,92E-04 | 1,044 | 41,5 | 0,9 | 1,0390 | 311,4 | 2,0 | 0,918 | 156,2 | 87,8 | 1,916E-04 | 0,91 | 5,8 |
| 4065,31 | 2,29E-04 | 1,051 | 37,1 | 0,8 | 1,0440 | 127,1 | 1,6 | 0,905 | 280,9 | 88,2 | 2,285E-04 | 0,91 | 6,7 |
| 4065,32 | 2,30E-04 | 1,051 | 39,5 | 0,4 | 1,0440 | 129,5 | 2,1 | 0,905 | 298,9 | 87,9 | 2,296E-04 | 0,91 | 6,7 |
| 4065,33 | 2,24E-04 | 1,051 | 39,7 | 0,0 | 1,0450 | 129,7 | 1,0 | 0,905 | 0,0 | 90,0 | 2,240E-04 | 0,91 | 6,8 |
| 4065,34 | 2,28E-04 | 1,050 | 221,8 | 0,0 | 1,0440 | 131,8 | 0,9 | 0,906 | 314,8 | 89,1 | 2,279E-04 | 0,90 | 6,7 |
| 4080,11 | 2,31E-04 | 1,047 | 222,0 | 1,0 | 1,0420 | 312,1 | 2,5 | 0,911 | 110,3 | 87,3 | 2,305E-04 | 0,93 | 6,3 |
| 4080,12 | 2,32E-04 | 1,047 | 217,5 | 0,7 | 1,0400 | 127,5 | 1,1 | 0,912 | 340,4 | 88,7 | 2,317E-04 | 0,90 | 6,2 |
| 4080,13 | 2,33E-04 | 1,047 | 212,6 | 0,8 | 1,0410 | 302,6 | 0,9 | 0,912 | 79,8 | 88,8 | 2,334E-04 | 0,92 | 6,2 |
| 4080,14 | 2,30E-04 | 1,047 | 225,0 | 0,5 | 1,0400 | 135,0 | 0,5 | 0,912 | 358,8 | 89,3 | 2,302E-04 | 0,90 | 6,2 |
| 4092,71 | 2,13E-04 | 1,046 | 221,9 | 0,7 | 1,0410 | 131,9 | 0,3 | 0,913 | 19,7 | 89,2 | 2,128E-04 | 0,92 | 6,2 |
| 4092,72 | 2,10E-04 | 1,046 | 221,4 | 0,3 | 1,0390 | 131,4 | 1,2 | 0,915 | 326,7 | 88,8 | 2,096E-04 | 0,89 | 6,0 |
| 4092,73 | 2,01E-04 | 1,045 | 216,5 | 0,4 | 1,0390 | 126,4 | 1,8 | 0,915 | 318,8 | 88,2 | 2,009E-04 | 0,91 | 6,0 |
| 4092,74 | 1,91E-04 | 1,046 | 222,1 | 1,4 | 1,0390 | 132,1 | 0,2 | 0,915 | 35,7 | 88,6 | 1,910E-04 | 0,89 | 6,0 |
| 4102,11 | 7,35E-05 | 1,023 | 16,3 | 0,3 | 1,0210 | 286,3 | 12,7 | 0,956 | 112,7 | 87,3 | 7,347E-05 | 0,95 | 3,1 |
| 4102,12 | 7,29E-05 | 1,024 | 4,3 | 0,5 | 1,0200 | 274,3 | 1,7 | 0,957 | 111,7 | 88,2 | 7,285E-05 | 0,89 | 3,1 |
| 4102,13 | 7,41E-05 | 1,022 | 24,6 | 0,2 | 1,0210 | 294,6 | 2,0 | 0,957 | 121,2 | 88,0 | 7,412E-05 | 0,97 | 3,0 |
| 4102,14 | 7,35E-05 | 1,022 | 201,1 | 0,0 | 1,0210 | 291,1 | 3,1 | 0,957 | 110,9 | 86,9 | 7,351E-05 | 0,95 | 3,0 |
| 4103,01 | 2,05E-04 | 1,046 | 217,0 | 0,9 | 1,0400 | 127,0 | 1,0 | 0,915 | 350,5 | 88,6 | 2,052E-04 | 0,91 | 6,0 |
| 4103,02 | 2,05E-04 | 1,046 | 223,9 | 0,2 | 1,0410 | 133,9 | 0,9 | 0,913 | 327,4 | 89,1 | 2,052E-04 | 0,92 | 6,2 |
| 4103,03 | 2,00E-04 | 1,046 | 221,4 | 0,8 | 1,0410 | 311,4 | 0,7 | 0,913 | 80,8 | 88,9 | 1,998E-04 | 0,92 | 6,2 |
| 4103,04 | 2,05E-04 | 1,047 | 231,0 | 1,2 | 1,0400 | 321,1 | 0,7 | 0,913 | 79,8 | 88,6 | 2,053E-04 | 0,91 | 6,2 |
| 4125,31 | 1,75E-05 | 1,019 | 14,8 | 0,8 | 1,0110 | 104,9 | 3,8 | 0,970 | 272,2 | 86,1 | 1,745E-05 | 0,69 | 2,1 |
| 4125,31 | 1,17E-05 | 1,018 | 36,3 | 3,4 | 1,0110 | 126,7 | 5,5 | 0,971 | 274,9 | 83,5 | 1,170E-05 | 0,67 | 2,1 |
| 4125,31 | 1,17E-05 | 1,019 | 18,0 | 4,2 | 1,0120 | 108,1 | 2,4 | 0,970 | 228,1 | 85,2 | 1,168E-05 | 0,71 | 2,2 |
| 4125,32 | 1,28E-05 | 1,013 | 27,1 | 7,0 | 1,0060 | 117,6 | 4,3 | 0,981 | 239,0 | 81,8 | 1,275E-05 | 0,57 | 1,4 |

| Sample | k_mean | k1 | Dec k1 | Inc k1 | k2 | Dec k2 | Inc k2 | k3 | Dec k3 | Inc k3 | k' | U | k'% |
|---|---|---|---|---|---|---|---|---|---|---|---|---|---|
| 4125,32 | 1,27E-05 | 1,012 | 14,4 | 5,1 | 1,0050 | 284,2 | 1,7 | 0,983 | 175,5 | 84,6 | 1,268E-05 | 0,50 | 1,2 |
| 4125,32 | 1,27E-05 | 1,011 | 34,1 | 9,8 | 1,0070 | 124,5 | 2,2 | 0,982 | 227,0 | 80,0 | 1,265E-05 | 0,68 | 1,3 |

Supplementary Table 2 Eigenvalues and eigendirections for principal axes of the deviatoric tensor for the paramagnetic component with their corresponding anisotropy parameters as determined from high-field torque AMS measurements

| Sample | k1 | Dec k1 | Inc k1 | k2 | Dec k2 | Inc k2 | k3 | Dec k3 | Inc k3 | k' | U | k'% |
|---|---|---|---|---|---|---|---|---|---|---|---|---|
| 3531 | 1,72E-05 | 212,5 | 2,1 | 1,51E-05 | 122,5 | 1,0 | -3,23E-05 | 8,0 | 87,7 | 2,29E-05 | 0,92 | 7,2 |
| 3593 | 8,44E-06 | 41,4 | 0,1 | 6,52E-06 | 131,4 | 2,0 | -1,50E-05 | 307,9 | 88,0 | 1,06E-05 | 0,84 | 5,6 |
| 3634 | 8,40E-06 | 42,1 | 0,2 | 6,48E-06 | 132,1 | 2,2 | -1,49E-05 | 308,1 | 87,8 | 2,48E-05 | 0,93 | 8,2 |
| 3665 | 7,68E-06 | 200,4 | 1,6 | 6,22E-06 | 110,3 | 4,8 | -1,39E-05 | 309,2 | 85,0 | 9,85E-06 | 0,87 | 5,3 |
| 3674 | 5,48E-06 | 213,9 | 2,7 | 4,56E-06 | 123,8 | 1,2 | -1,00E-05 | 9,5 | 87,0 | 7,10E-06 | 0,88 | 4,5 |
| 3751 | 1,13E-05 | 51,3 | 0,3 | 9,68E-06 | 141,3 | 0,0 | -2,10E-05 | 237,4 | 89,7 | 1,49E-05 | 0,90 | 6,3 |
| 3890 | 9,80E-06 | 217,5 | 0,7 | 8,54E-06 | 127,5 | 1,2 | -1,83E-05 | 338,1 | 88,6 | 1,30E-05 | 0,91 | 6,4 |
| 3967 | 9,37E-07 | 218,4 | 4,3 | 3,28E-07 | 126,7 | 21,9 | -1,27E-06 | 318,9 | 67,6 | 9,28E-07 | 0,45 | 0,9 |
| 3977 | 5,10E-08 | 182,0 | 4,7 | 8,61E-09 | 285,5 | 70,6 | -5,96E-08 | 90,4 | 18,7 | 4,56E-08 | 0,23 | 0,1 |
| 4020 | 9,55E-06 | 42,1 | 1,0 | 8,18E-06 | 132,1 | 0,9 | -1,77E-05 | 263,7 | 88,6 | 1,26E-05 | 0,90 | 6,6 |
| 4092 | 1,15E-05 | 220,0 | 1,2 | 9,84E-06 | 130,0 | 1,1 | -2,13E-05 | 355,8 | 88,4 | 1,50E-05 | 0,90 | 7,0 |
| 4103 | 1,01E-05 | 217,9 | 0,8 | 8,70E-06 | 127,9 | 0,5 | -1,88E-05 | 7,7 | 89,0 | 1,33E-05 | 0,90 | 6,5 |

Supplementary Table 3 Eigenvalues and eigendirections for principal axes of the deviatoric tensor for the modeled bulk rock composition with their corresponding anisotropy parameters

| Sample | k_mean | k1 | Dec k1 | Inc k1 | k2 | Dec k2 | Inc k2 | k3 | Dec k3 | Inc k3 | k' | U | k'% |
|---|---|---|---|---|---|---|---|---|---|---|---|---|---|
| 3531 | 5,31E-08 | 5,53E-08 | 201,6 | 1,9 | 5,51E-08 | 291,6 | 0,2 | 4,90E-08 | 27,8 | 88,1 | 2,92E-09 | 0,94 | 5,5 |
| 3593 | 4,85E-08 | 5,01E-08 | 50,3 | 1,9 | 4,97E-08 | 140,2 | 1,8 | 4,56E-08 | 6,6 | 87,4 | 2,03E-09 | 0,83 | 4,2 |
| 3634 | 5,14E-08 | 5,40E-08 | 212,9 | 1,9 | 5,38E-08 | 302,9 | 0,6 | 4,63E-08 | 50,4 | 88,0 | 3,58E-09 | 0,96 | 7,0 |
| 3665 | 4,53E-08 | 4,72E-08 | 198,0 | 2,0 | 4,65E-08 | 107,5 | 4,4 | 4,21E-08 | 312,5 | 85,1 | 2,25E-09 | 0,75 | 5,0 |
| 3674 | 3,98E-08 | 4,10E-08 | 203,7 | 2,8 | 4,07E-08 | 293,6 | 0,4 | 3,77E-08 | 16,5 | 87,1 | 1,51E-09 | 0,79 | 3,8 |
| 3751 | 4,99E-08 | 5,16E-08 | 43,3 | 0,4 | 5,14E-08 | 313,3 | 0,1 | 4,67E-08 | 27,8 | 89,6 | 2,29E-09 | 0,92 | 4,6 |
| 3890 | 2,17E-08 | 2,26E-08 | 36,0 | 0,4 | 2,25E-08 | 306,0 | 0,0 | 1,99E-08 | 218,9 | 89,6 | 1,24E-09 | 0,89 | 5,7 |
| 3967 | 3,65E-08 | 3,71E-08 | 219,5 | 0,3 | 3,69E-08 | 309,4 | 16,6 | 3,54E-08 | 310,3 | 73,4 | 7,48E-10 | 0,72 | 2,1 |
| 3977 | 1,97E-09 | 2,05E-09 | 355,4 | 13,9 | 1,97E-09 | 266,0 | 2,5 | 1,88E-09 | 186,2 | 75,9 | 6,61E-11 | 0,02 | 3,4 |
| 4020 | 4,48E-08 | 4,68E-08 | 40,0 | 1,8 | 4,66E-08 | 310,1 | 0,7 | 4,10E-08 | 61,5 | 88,1 | 2,67E-09 | 0,91 | 6,0 |
| 4103 | 5,30E-08 | 5,49E-08 | 43,4 | 0,2 | 5,48E-08 | 313,4 | 0,1 | 4,94E-08 | 250,0 | 89,8 | 2,57E-09 | 0,97 | 4,8 |

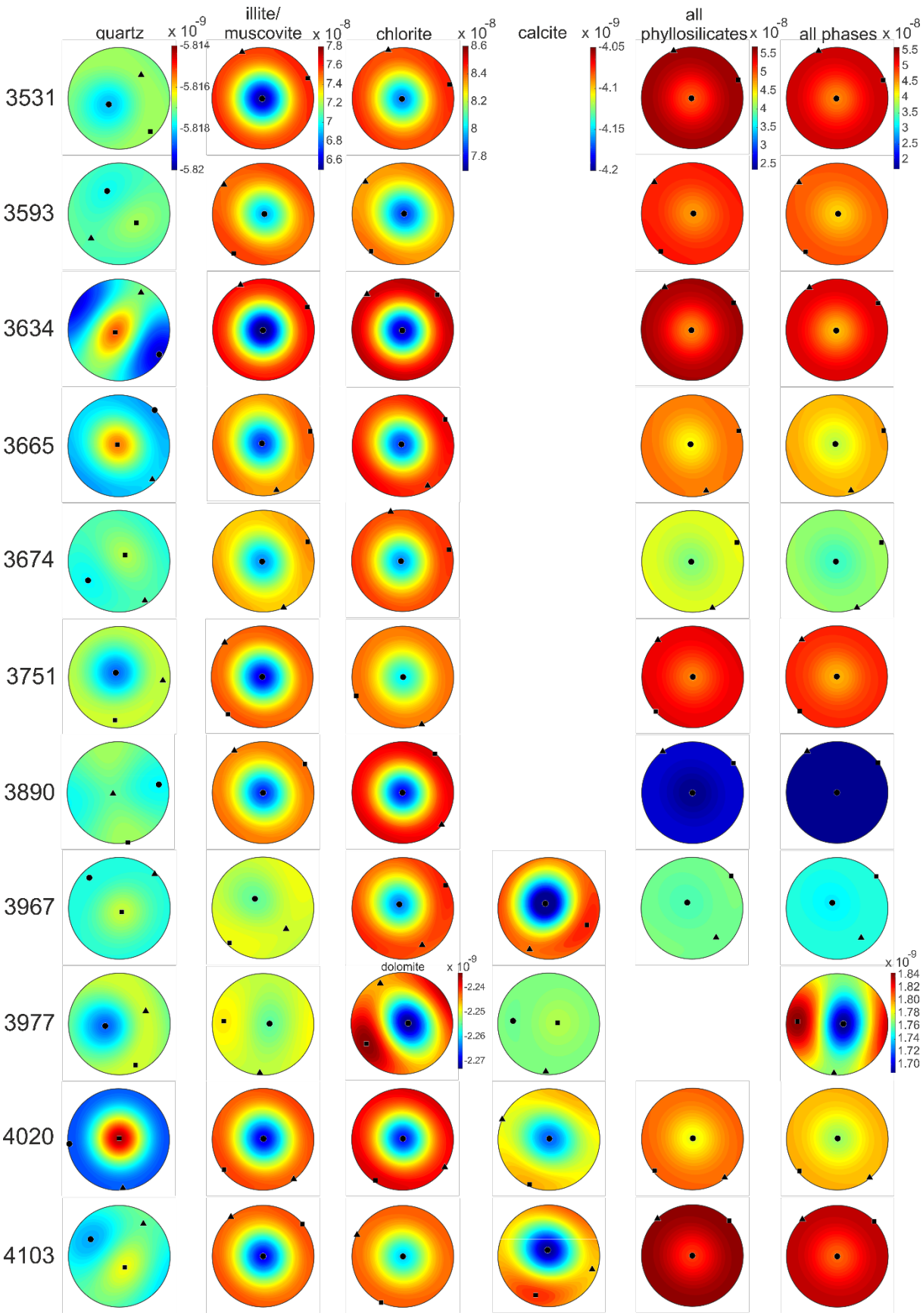


Supplementary Figure 1 Overview of all model contributions of the different minerals and the combined paramagnetic and bulk magnetic mode